

8. Appendices

Published and Submitted Works

APPENDIX I

Accurate Mineralogical Characterization to Assess the Radiocarbon Dating of Historical Lime Mortars

APPENDIX I.1

Hydrotalcite and Hydrocalumite in Mortar Binders from the Medieval Castle of Portilla (Álava, North Spain): Accurate Mineralogical Control to Achieve More Reliable Chronological Ages

Graciela Ponce-Antón, Luis Angel Ortega, Maria Cruz Zuluaga,
Ainhoa Alonso-Olazabal, Jose Luis Solaun

Minerals 2018; 8(8):326

Article Metrics

✓ Journal Citation Reports

Citations: 1

Impact Factor

2018	5 Years
2.25	2.453

JCR® Rank	Classification	Quartile	Percentile
Mineralogy	12 of 29	Q2	60.345
Mining & Mineral Processing	6 of 19	Q2	70.053

✓ Scopus

Citations: 3

CiteScore 2018	2.46
SJR 2018	0.427
SNIP 2018	0.966

CiteScore Rank	Classification	Percentile
Earth and Planetary Sciences (Geotechnical Engineering and Engineering Geology)	39 of 176	78
Earth and Planetary Sciences (Geology)	47 of 217	78

✓ Google Academic

Citations: 7

Article

Hydrotalcite and Hydrocalumite in Mortar Binders from the Medieval Castle of Portilla (Álava, North Spain): Accurate Mineralogical Control to Achieve More Reliable Chronological Ages

Graciela Ponce-Antón ^{1,*} , Luis Angel Ortega ¹ , Maria Cruz Zuluaga ¹,
Ainhoa Alonso-Olazabal ¹ and Jose Luis Solaun ² 

¹ Department of Mineralogy and Petrology, Science and Technology Faculty, University of the Basque Country-UPV/EHU, Sarriena s/n, 48940 Leioa, Bizkaia, Spain; luis.ortega@ehu.eus (L.A.O.); mcruz.zuluaga@ehu.eus (M.C.Z.); ainhoa.alonso@ehu.eus (A.A.-O.)

² Department of Geography, Prehistory and Archaeology, Faculty of Arts, University of the Basque Country-UPV/EHU, Paseo de la Universidad, 5, 01006 Vitoria-Gasteiz, Spain; joseluis.solaun@ehu.eus

* Correspondence: graciela.ponce@ehu.eus; Tel.: +34-946-015-456

Received: 8 June 2018; Accepted: 26 July 2018; Published: 29 July 2018



Abstract: Mortars from different stratigraphic units at Portilla Castle (Alava, North Spain) have been analyzed for mineralogical characterization before radiocarbon dating. The mortar binder at Portilla Castle is composed not only of neof ormation calcite but also of double-layered hydroxide (LDH) minerals such as hydrotalcite and hydrocalumite. The mineralogy of several fractions of the binder has been analyzed to determine the granulometric distribution of minerals in the binder. The continuous monitoring of mineralogy during the extraction of different grain size fractions has been performed by using a scanning electron microscopy (SEM), X-ray diffraction (XRD), and thermogravimetric analyses (TGA). Hydrotalcite and hydrocalumite-bearing mortar binders give older ages than expected since they introduce dead carbon into the system.

Keywords: mortar; binder; hydrotalcite; hydrocalumite; radiocarbon dating

1. Introduction

One of the main goals in building archaeology is to determine the age of the structures discovered. In the absence of written records or other archaeological evidence to establish the chronology of the building, traditionally wooden timbers are used in radiocarbon dating [1]. Through this way, the date obtained may point to older ages due to material reuse or long storage. Therefore, it is vital to determine that the historical remains are not affected by the use of older construction materials since the reuse of wood materials leads to an in-built age defined as the difference between the time when the wood formed and the date of the event of interest [2–5].

In this framework, mortars can provide a potential dating solution. Archaeological mortars are artificial materials composed of a mixture of lime or plaster as binder and sand or other kinds of organic or inorganic additive as aggregates. The ease of preparation as well as the availability of raw materials and their durability have contributed to make mortars ubiquitous materials at sites from the Neolithic period onwards, which becomes an important source of information in archaeological sites [6,7].

Archaeological mortars have been dated by using radiocarbon methods since the 1960s as a way to determine the age of historical/archaeological structures. As such, the application of radiocarbon dating of mortars has been described by several authors [8–21]. Many studies have used charcoal

fragments or other organic inclusions embedded in the mixture to date archaeological mortars. However, the dating of charred materials could provide aged dates by incorporating “dead” C into the system since the calcination process can already be decades or centuries old [22–24].

Lime mortar dating is useful since the mortar binder should reflect the time period when the building was constructed. The basic mortar production technology, known as the lime cycle, can be explained as follows: the calcium carbonate (CaCO_3) of the limestone is heated at a high temperature (800–1000 °C) to liberate carbon dioxide (CO_2) and produce quicklime (CaO) in the calcination process (Equation (1)). Then the calcium oxide is slaked by adding water. It then forms portlandite (Ca(OH)_2) (Equation (2)). Throughout this phase, portlandite crystals are rearranged and become smaller and foil-like, which enhances their future CO_2 absorption capability [25]. The slaked lime is mixed with aggregates to increase its workability. In the setting phase, the calcium hydroxide in the mortar reacts with atmospheric carbon dioxide and again becomes calcium carbonate in a carbonation process (Equation (3)) [26].

The lime cycle is summarized in the following equations.



The ^{14}C of atmospheric carbon dioxide is fixed in the neoformation carbonate as a result of the hardening process and the radiocarbon dating of the binder gives the age of the building. In practice, discrepancies between radiocarbon ages and expected ages are frequently observed. These fluctuations correspond to primary carbonate relicts resulting from the inefficient calcination of the limestone or to carbonate aggregates (limestone fragments) added to the mortar. Those carbonates of different origin are the main problem in radiocarbon dating since they affect the accuracy of results by adding “dead” C to the system and cause an aging of dates [15,18,21,27].

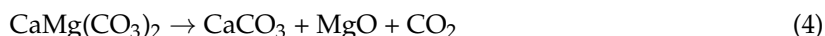
Several methodologies and preparation procedures have been developed to isolate a pure neo-formation calcite fraction without any other carbon contaminant [17–21,28–31]. The first procedures to date the binder consisted of the hydrolysis of lime binder particles of different grain size fractions by using diluted hydrochloric acid (HCl) or 85% orthophosphoric acid (H_3PO_4) [12,13,16,17,19–21,32–35]. When carbonate aggregates appear, mechanical/physical methods of binder extraction are an alternative to chemical methods to avoid contamination by carbonate aggregates in the fraction used for hydrolysis [29,30,36]. The use of lime lumps in mortar for radiocarbon dating has been reported by Van Strydonck et al. [16] and Lindroos et al. [17] since these lumps represent a pure binder when the lime is scarcely mixed with the aggregates [37,38].

However, previously developed protocols do not always solve the problem because often the obtained ages are older or younger than expected. Since the proposed methods do not seem to provide consistent and reproducible results, it is imperative to develop new procedures to assess the contaminant nature and the granulometric distribution within the binder. Since particle size is the main issue to obtain a suitable fraction for dating, the extraction and monitoring of the adequate grain size particle of the binder becomes vital [28].

When dolostones and/or limestones enriched in magnesium are used as a raw material in lime production, magnesium minerals should be considered in the mortar binder because they may add new problems to mortar dating.

During the calcination of calcium magnesium rich limestone, the dolomitic lime cycle differs from the typical lime cycle. When the natural dolomite ($\text{CaMg}(\text{CO}_3)_2$) is burned, a half thermal decomposition occurs by generating a mixture of periclase (MgO), quicklime (CaO) and calcite (CaCO_3) [39]. At the beginning, during the calcination process between 640 °C to 740 °C, the dolomite decomposes to produce calcite (CaCO_3) and periclase (MgO) (Equation (4)). Afterward, the generated

calcium carbonate decomposes in quicklime (CaO) (Equation (5)). These reactions are described by the equations below.



As a result of the slaking process, besides portlandite ($\text{Ca}(\text{OH})_2$), the brucite ($\text{Mg}(\text{OH})_2$) mineral phase is also formed, which leads to a wider variety of phases during the carbonation process of the mortar binder.

In comparison with the carbonation of portlandite to calcite, the carbonation of brucite is not simple. Brucite is a relatively stable compound that causes a slow carbonation process and even yields partial carbonation. The resulting mortars contain a mixture of compounds in varying amounts. Therefore, the dolomitic lime cycle does not constitute a full cycle like the calcium lime cycle [40].

Likewise, during the slaking process in the dolomitic cycle, layered double hydroxide (LDH) compounds can be formed [41]. In general, LDH minerals are often referred to as hydrotalcite-like clay (HT-like) since hydrotalcite is one of the most representative minerals in this group [42,43]. The presence of Al^{3+} ions combining with Mg^{2+} ions from MgO leads to the formation of hydrotalcite crystals [$\text{Mg}_6\text{Al}_2(\text{CO}_3)(\text{OH})_{16}\cdot 4(\text{H}_2\text{O})$] [44]. The MgO- Al_2O_3 rehydrates and combines with other available anions present in the putty to form hydrotalcite in the presence of water [45,46].

A hydrotalcite mineral is based on positive brucite-like layers alternating with layers containing anions and water molecules. In the crystallographic structure of hydrotalcite, some Mg^{2+} cations are replaced isomorphously by Al^{3+} cations in octahedral sites. The resultant positive charge is balanced by CO_3^{2-} anions in the interlayer sites where the crystallization water can also be found [47–50].

Under hyper-alkaline conditions during the slaking process, Ca^{2+} ions are sparingly soluble [51,52]. Over time, early-formed portlandite is consumed, which forms more stable Ca minerals [53]. In the presence of aluminate ions ($\text{Al}(\text{OH})_4^-$) from the decomposition of clay minerals present as impurities in the raw material, the portlandite ($\text{Ca}(\text{OH})_2$) is transformed into some forms of LDH minerals such as hydrocalumite [$\text{Ca}_4\text{Al}_2(\text{Cl},\text{CO}_3,\text{OH})_2(\text{OH})_{12}\cdot 4\text{H}_2\text{O}$] [54,55]. Therefore, hydrocalumite is the calcium analogue of hydrotalcite [50,56]. Consequently, these LDH minerals have a high capacity to capture large anions such as CO_3^{2-} due to their ion-exchange properties [47].

LDH phases have been observed in ancient hydraulic mortars, in modern pozzolanic cements, and in dolomitic lime mortars [57–60]. Nevertheless, until the current study, neither the shape nor the size distribution of hydrotalcite and hydrocalumite in the lime mortars has ever been described in detail. To this end, it is essential to establish particle size distribution of mineral phases in the binder. For this purpose, several size grain fractions of the binder have been extracted by a settling procedure and by checking the mineralogy of all fractions using multi-analytical techniques.

The aim of this work is to study mineral composition of the mortar binder obtained by the calcination of dolostones and/or impure limestones in order to select the adequate fraction to date. Several mortar samples from the main structures of Portilla Castle (Álava, Spain) have been analyzed by adapting previous extraction procedures to the real mineralogy.

2. Archaeological Background

The archaeological site of Portilla is located in the village of Zambrana (Álava, Spain) (Figure 1). Portilla Castle and the Portilla de Ibda medieval village form the archaeological site. The site was classified as Cultural Heritage with the category of Monumental Complex in 2012 because it constitutes one of the best-conserved examples of a fortified medieval settlement. The archaeological work showed discontinuous periods of occupation during the Late Bronze and Early Iron Ages, the Late Roman Period (3rd to 5th centuries AD), and the Late Middle Ages (11th to 15th centuries).

Portilla Castle is located on Txulato Mountain and the strategic location was valuable for the Kingdom of Navarre during the 11th and 12th centuries until, in the 13th century, it became part of the

Kingdom of Castile. In the early 14th century, the fortified village gradually lost its population as a more accessible settlement was established in the valley. Although the first written references to Portilla date back to the year 1040, the origin and later evolution of the building remains unknown [61,62].



Figure 1. Geographic location of Portilla Castle (Álava, Spain).

3. Materials and Methods

Seven samples of archaeological mortars from different stratigraphic units (SU) at Portilla Castle were considered for lime mortar sampling. Of the fourteen structures defined [62], the three most significant structures were selected in the sampling known as the West Tower (A14, SU-2), Tower Keep (A12, SU-4), and the East Tower (A11, SU-19) (Figure 2 and Table 1).



Figure 2. Studied structures at Portilla Castle. West Tower (A14), Tower Keep (A12), and East Tower (A11).

Table 1. Studied samples from different structures at Portilla Castle.

Stratigraphic Unit	Archaeological Structure	Sample
SU-2	West Town (A14)	CP-2
SU-4	Tower Keep (A12)	CP-4 CP-13-6 CP-13-8 CP-13-10
SU-19	East Town (A11)	CP-19 CP-13-3

SU: Stratigraphic Unit.

To determine the binder and aggregate types, mortar thin-sections were analyzed by an optical polarizing microscope using a Nikon Eclipse LV100POL microscope equipped with a DS F-I1 digital camera and a DS L-2 control unit.

The binder was analyzed by several techniques. The X-ray diffraction (XRD) analysis in a powder sample was performed using a Philips X'Pert diffractometer (Malvern PANalytical, Almelo, The Netherlands) equipped with a monochromatic Cu- $k_{\alpha 1}$ X-radiation operating at 40 kV and 20 mA. The data collection on the powder sample was performed by a continuous scan in the range 5° to 70° [2 θ] at an acquisition rate of 0.02° per second [20]. The interpretation of diffraction patterns and semi-quantitative calculation were performed with X'Pert HighScore Plus 3.0 software (Malvern PANalytical, Almelo, The Netherlands) by using a PANalytical on the basis of the characteristic space of each mineral by reconstructing mineral profiles of the compounds and comparing the experimental peaks with experimental patterns of ICDD and ICSD diffraction databases. The extracted fractions of the binder were analyzed by using the scanning electron microscopy (SEM) with a JEOL JSM-7000F Schottky-type field emission scanning electron microscope (JEOL, Tokyo, Japan) and by operating with an Oxford Pentafet photon energy instruments Link Isis X-ray (EDX) microanalysis system. Samples were carbon-coated to eliminate charging effects. Thermo-gravimetric analysis (TGA) was performed in a TA SDT 2960 TG-DSC simultaneous instrument (TA Instruments, New Castle, DE, USA). Pt crucibles containing 5 mg to 7 mg of the sample were heated at $2^{\circ}\text{C min}^{-1}$ from room temperature to 1000°C under a dry oxidizing atmosphere. The samples have been dated by the ^{14}C accelerator technique (AMS) in Beta Analytic Inc. (Miami, FL, USA). The conventional ^{14}C ages were calibrated by using OxCal v4.2.3 software [63] and an IntCal13 atmospheric calibration curve [64].

Extraction Procedure

A settling extraction procedure has been performed to obtain different grain size fractions of the binder based on the procedure described by Ortega et al. [28]. In order to assess the potential of the binder as a time record, the extracted fractions have been characterized mineralogically. Unlike in Ortega et al. [28], the mortars from Portilla Castle show a more complex mineralogy in the finest fraction ($<2\ \mu\text{m}$). The occurrence of potential contaminant phases such as LDHs has led to an adjustment of the extraction procedure to refine the fraction suitable for dating. The modification of the procedure consists of both modifying centrifugation times and including an additional extraction step. The modified extraction procedure of the fractions consists of the following steps (Figure 3).

1. The few upper millimeters of mortar surface were removed using a scraper to eliminate the altered surfaces that may interfere in the analytical results. Then mortars were crumbled manually, which is described by Casadio et al. [65]. The fragments of charcoal produced during lime production were picked out and removed.
2. The sample was placed in an ultrasonic bath with 150 mL of ultrapure water for 10 min. To promote further crumbling, the test tube was shaken vigorously and then left to rest for 5 min.

- Then, the topmost 50 mL of suspended volume corresponding to particle fraction size 2 μm to 20 μm was extracted. This fraction was referred to as coarse fraction (CF).
- Coarse fraction enriched in the binder was re-suspended in 65 mL of ultrapure water and placed in the ultrasonic bath to promote particle disaggregation. The suspension was centrifuged for 100 s at 1000 rpm. The uppermost 15 mL were collected corresponding to a grain size fraction of $<2 \mu\text{m}$ and were referred to as a fine fraction (FF).
 - From the fine fraction, the particles of grain size $<0.5 \mu\text{m}$ were removed. To this end, the sample was re-suspended again in 65 mL of ultrapure water and placed in an ultrasonic bath. The suspension was centrifuged for 9 min at 2000 rpm and the uppermost 15 mL were collected and referred to as ultrafine fraction (UF).
 - The suitable fraction enriched in neoformation calcite was obtained as a result of removing the ultrafine fraction (UF) from the fine fraction (FF). This fraction was named a target fraction (TF) corresponding to a grain size between 0.5 μm to 2 μm .
 - The collected fractions were concentrated via centrifugation at 3000 rpm for 10 min using a Kubota 3000 centrifuge (Kubota Corp., Tokyo, Japan).

To avoid the precipitation of calcite during the extraction process by absorption of modern atmospheric CO_2 , ultrapure water was used throughout the process. Moreover, the water is buffered at $\text{pH} = 8$ to preclude the calcite dissolution and favor the optimal scattering of small crystals [66] and, at the same time, avoid chemical reactions that dissolve the calcite [67]. Furthermore, 30 mL of each collected fraction (CF, FF, UF, and TF) were placed in a Petri dish to monitor fraction grain size by several analytical techniques in order to determine the mineralogical composition throughout the procedure. The fractions were dried in an oven at 80 $^\circ\text{C}$. According to the binder/aggregate relation of mortars, the procedure was repeated as necessary until a sufficient amount of the binder for accelerator mass spectrometry (AMS) analysis ($>0.8 \text{ mg}$) was obtained.

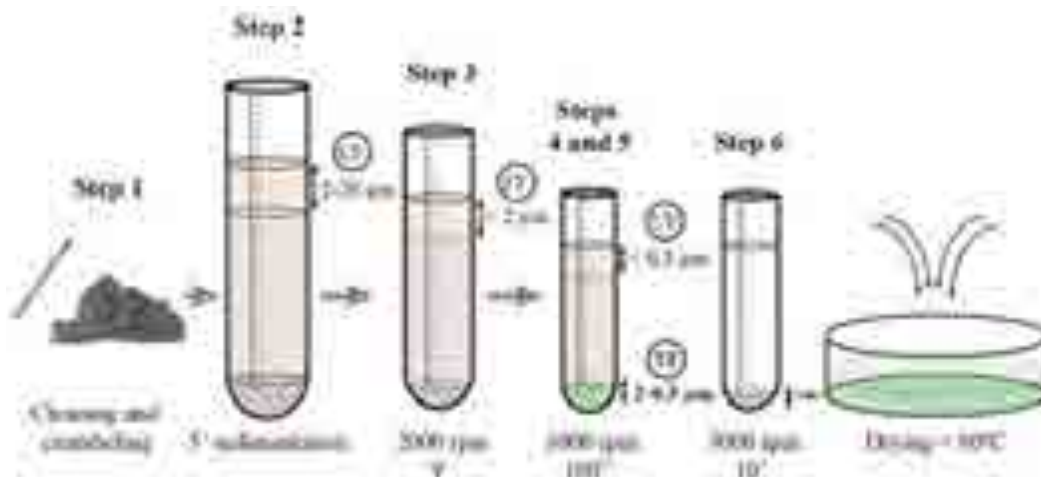


Figure 3. Extraction procedure to obtain the target fraction. Steps 2 to 5 show the mechanical separation of different particle-fractionations of the binder mortar and Step 6 shows the concentration of the extracted fraction. CF: coarse fraction, FF: fine fraction, UF: ultrafine fraction, TF: target fraction.

4. Results and Discussion

Petrographic studies of mortar have been used to identify the nature of aggregates and the binder. The relation and ratios between the aggregates and cementing matrix, texture, form, and size of mortar components have also been observed. The petrographic study of the Portilla samples revealed the similar nature of all the mortars but revealed heterogeneous textures. Aggregates were composed by heterometric and angular/sub-angular detrital quartz, limestone fragments, some

partially dolomitized, and unburnt limestone remains (Figure 4a,b). Within the binder matrix, heterometric lime lumps were observed (Figure 4c,d). Additionally, minute charcoal fragments were present in most samples (Figure 4d). Textural and mineralogical heterogeneities constituted additional difficulties for the extraction of the binder.

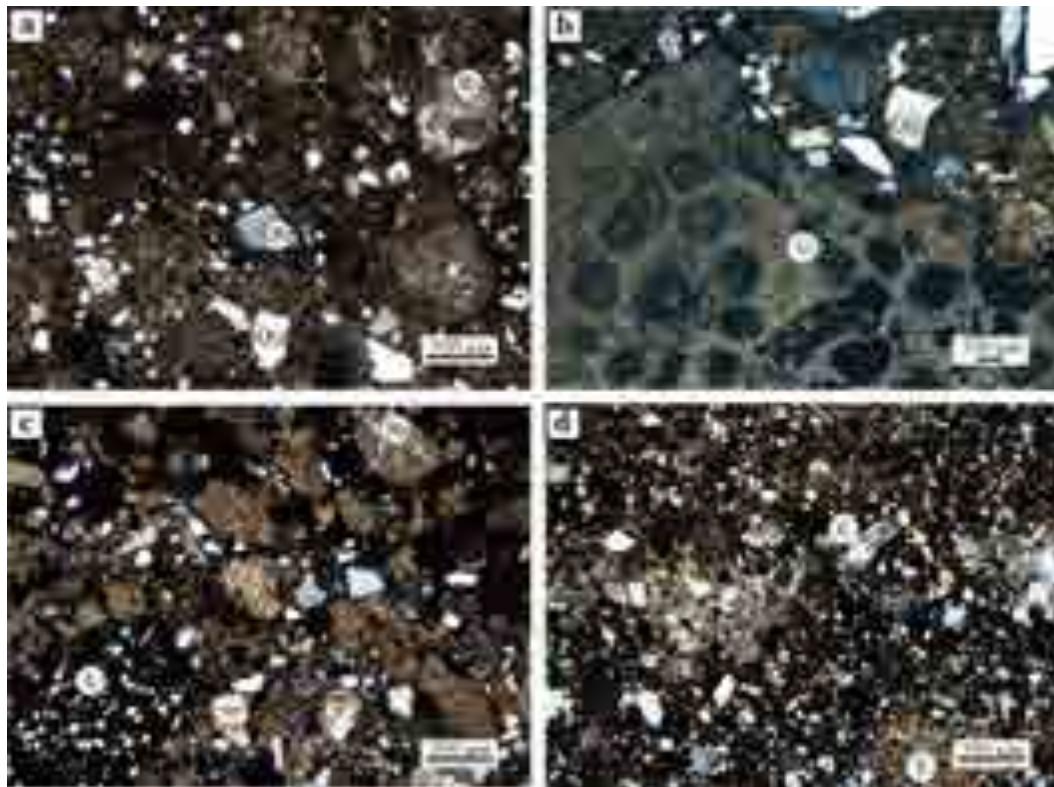


Figure 4. Photomicrographs showing the textural heterogeneity of historic lime mortars from Portilla Castle. (a) Mortar with rock fragments, lumps, and quartz grains. (b) Fragments of unburnt limestone and angular quartz grains. (c) Mortar with limestone fragments and quartz bearing lumps. (d) Mortar with a pure lump and charcoal fragment. Rx: rock fragment, Qtz: quartz, L: lump, U: unburnt, C: charcoal.

During the binder extraction process, several analytical techniques were applied to evaluate the mineralogy of the different fractions and monitoring the extraction method. By XRD analysis of the fine fraction ($<2\ \mu\text{m}$), magnesium calcite was identified as the main component of all samples while quartz, hydrotalcite [$\text{Mg}_6\text{Al}_2(\text{CO}_3)(\text{OH})_{16}\cdot 4(\text{H}_2\text{O})$], and hydrocalumite [$\text{Ca}_4\text{Al}_2(\text{Cl},\text{CO}_3,\text{OH})_2(\text{OH})_{12}\cdot 4\text{H}_2\text{O}$] are also present in minor amounts (Figure 5). The low intensity of hydrotalcite and hydrocalumite reflections indicates not only low abundance but also the low degree of crystallization of these mineral phases [49].

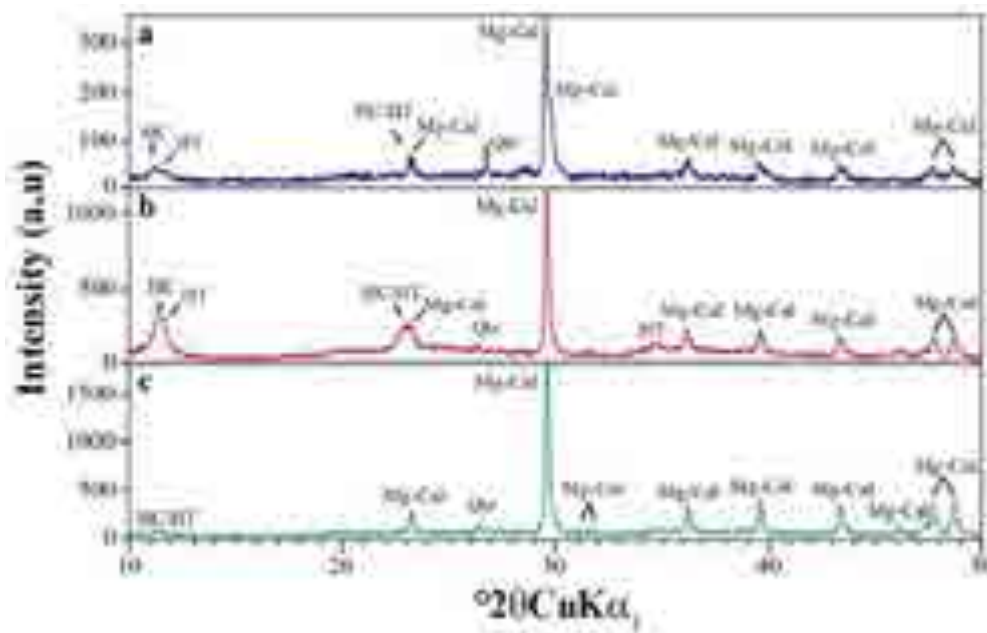


Figure 5. X-ray diffraction patterns of extracted binder fractions. (a) Fine fraction, (b) ultrafine fraction, and (c) target fraction. HC: hydrocalumite, HT: hydrotalcite, Qtz: quartz, Mg-Cal: magnesium calcite.

These LDH mineral phases are formed as a result of the slaking process and identification and characterization is crucial due to their very high ability to fix carbonate anions [68]. During the rehydration process, CO_3^{2-} from the partial washing of unburnt fragments of limestone is fixed in the crystalline structure of HT-like minerals. The captured CO_3^{2-} introduces dead carbon in the system and ages the radiometric dates. A new step was introduced in the extraction procedure in order to remove the potential contaminant HT-like mineral phases in the ultrafine fraction ($<0.5 \mu\text{m}$).

SEM observations of fine fraction ($<2 \mu\text{m}$) of the binder confirm the presence of very small HT-like particles embedded in a calcitic matrix (Figure 6). Irregular and hexagonal crystals of $<0.5 \mu\text{m}$ grain size, corresponding to Ca-enriched or Mg-enriched anion clays, can be observed in Figure 6b. The Energy Dispersive X-ray (EDX) analyses indicate that well-formed or euhedral crystals correspond to Ca-enriched HT-like particles (point 1 in Figure 7) while the irregular or anhedral crystals correspond to Mg-enriched HT-like particles (point 2 in Figure 7). Therefore, Ca-enriched particles correspond to hydrocalumite and Mg-enriched particles to hydrotalcite. In fact, hydrotalcite is more likely to be present as a non-well-formed phase compared with hydrocalumite [44]. The EDX analysis also shows the presence of silica that has been attributed to the presence of microcrystalline quartz. The SEM images of ultrafine fraction ($<0.5 \mu\text{m}$) show a homogeneous matrix composed only of hydrotalcite and hydrocalumite phases of a $<0.5 \mu\text{m}$ grain size. The SEM-EDX analysis supports that the extraction of HT-like minerals from the fine fraction was successful (Figure 6c).



Figure 6. Scanning Electron Microscopy images of binder mortar: (a,b) fine fraction and (c) ultrafine fraction. Point 1 and point 2 indicate the particles analysed by EDX.

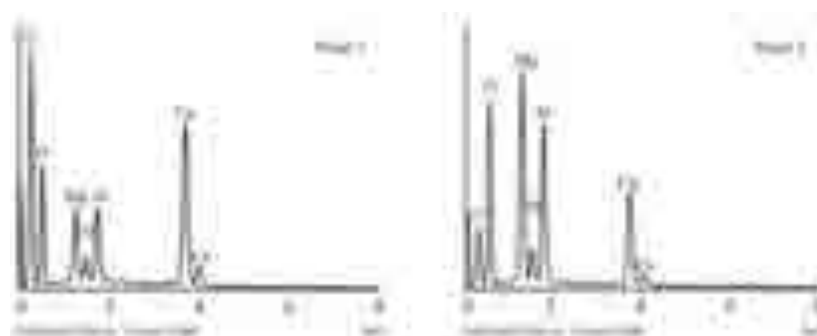


Figure 7. Energy dispersive X-ray analyses results of layered double hydroxides (LDH) of the fine fraction shown in Figure 6b. Point 1 is Ca-enriched anion clay (i.e., hydrocalumite) and point 2 is Ca-enriched anion clay (i.e., hydrotalcite).

Petrographic, XRD, and SEM-EDX analyses show that the raw material used to obtain lime was impure limestone and/or partially dolomitized limestone. When limestones enriched in calcium magnesium are calcined, magnesium minerals should be considered in the mortar binder. Magnesium oxide (MgO) is formed as well as calcium oxide (CaO) during the calcination of dolomitic rocks due to the dolomitic cycle, which differs from the typical lime cycle (Figure 8).

Considering that the LDH mineral phases constitute a potential contaminant in radiocarbon dating, the grain size fraction $<0.5 \mu\text{m}$ (i.e., ultrafine fraction) is extracted in order to eliminate these phases. XRD patterns of UF show significant increases of reflexions at $d = 7.86 \text{ \AA}$ ($11.2^\circ 2\theta$), $d = 7.69 \text{ \AA}$ ($11.4^\circ 2\theta$), $d = 3.83 \text{ \AA}$ ($23.2^\circ 2\theta$), and $d = 2.58 \text{ \AA}$ ($34.4^\circ 2\theta$) corresponding to hydrotalcite and indicate a large enrichment of LDH mineral phases in the ultrafine fraction (Figure 5b).

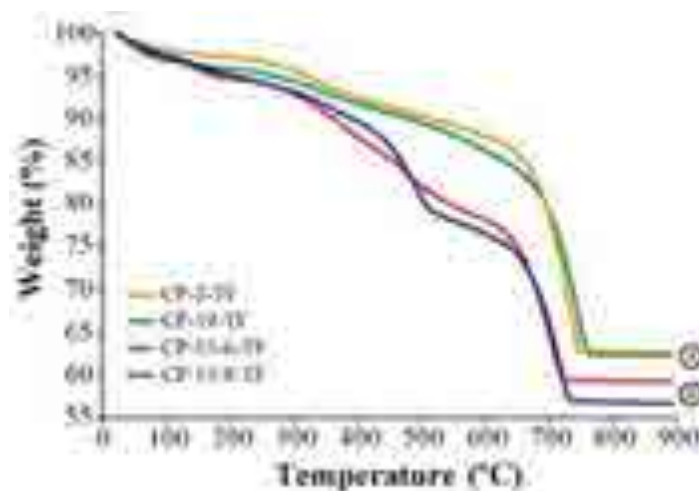
As a result of the LDH minerals phase being removed, the target fraction (TF) corresponds to the grain size fraction between $0.5 \mu\text{m}$ to $2 \mu\text{m}$. An XRD pattern of the TF fraction shows an increase in magnesium calcite reflections while hydrotalcite reflections disappear (Figure 5c). Nevertheless, an extraction procedure of the target fraction has to be checked in each mortar sample. Figure 9 shows XRD patterns of the target fraction of several samples. The presence and the intensity of characteristic reflections of LDH minerals in some XRD patterns suggest different levels of refinement in the extraction procedure, which indicates different amounts of LDH minerals in each sample. As can be observed, CP-2-TF, CP-4-TF, and CP-19-TF samples exhibit low intensity hydrotalcite reflections while CP-13-3-TF, CP-13-6-TF, CP-13-8-TF, and CP-13-10-TF samples still present significant LDH mineral reflections.

Table 2. Semi-quantitative data results (%) of X-ray diffraction analyses of target and ultrafine fractions of mortar binders.

Sample	Target Fraction (%)					Ultrafine Fraction (%)				
	Mg-Cal	HT	HC	Qtz	Total LDHs	Mg-Cal	HT	HC	Qtz	Total LDHs
CP-2	88	3	6	3	9	64	12	24	-	36
CP-4	84	8	8	-	16	58	16	26	-	42
CP-13-6	62	10	28	-	38	38	28	34	-	62
CP-13-8	79	9	10	2	19	48	28	24	-	52
CP-13-10	85	4	10	1	14	55	22	23	-	45
CP-19	89	5	5	1	10	55	24	20	-	44
CP-13-3	68	13	18	1	31	61	11	28	-	39

Mg-Cal: magnesium calcite, HT: hydrotalcite, HC: hydrocalumite, Qtz: quartz, LDHs: layered double hydroxides.

The temperature ranges and relative weight loss observed in TGA analysis are reliable for the characterization of these materials. The first weight loss below 120 °C is attributed to the presence of adsorption water in the inter-particle pore. The second weight loss occurs between 120 and 200 °C and is attributed to the crystallization water or the interlayer water. The weight loss between 200 °C to 600 °C is attributed to structural OH⁻, which corresponds to the dehydration of the Ca(OH)₂ of pure carbonates. Lastly, at temperatures above 600 °C, the loss of CO₂ takes place due to the decomposition of the carbonate [69–71]. However, in the third decomposition step (200 °C to 600 °C) of target fraction (0.5 µm to 2 µm) from Portilla Castle samples, the TGA curve shows two weight loss steps (Figure 10). These weight losses correspond to the decomposition of LDH phases and are attributed to the loss of the OH⁻ groups bonded to Al³⁺ and to Mg²⁺ in Mg-Al-CO₃ compounds [72,73].

**Figure 10.** Thermo-gravimetric analyses of target fractions of representative mortar binders. (A) Binder samples with little weight loss and (B) binder samples with clear stepped weight loss in the 200 °C to 600 °C range.

The thermos-gravimetric analyses of the target fraction show two different patterns, which are representative of TGA curves. These patterns are shown in Figure 10. The pattern type-A corresponds to samples with little weight loss in the 200 °C to 600 °C range (CP-2-TF, CP-4-TF, and CP-19-TF) while pattern type-B displays a pronounced stepped weight loss (CP-13-3-TF, CP-13-6-TF, CP-13-8-TF, and CP-13-10-TF). Table 3 summarizes the weight loss percentages of the target fraction in each temperature range. Samples show weight loss between 1.5% and 2.9% due to adsorbed water. The lower weight loss of water molecules from the interlayer space corresponds to type-A patterns and higher to type-B patterns. The weight loss between 200 °C and 600 °C temperature range corresponding to the

dehydroxylation processes shows larger variations in the TG curves. Type-A pattern curves show weight loss varying from 10.3% to 12.8% while the weight loss in the type-B patterns varies from 13.6% to 19.6%. Weight loss in dehydroxylation processes shows larger contents of LDH minerals in the type-B samples than in samples with a type-A pattern. When over 600 °C, carbonates decompose and CO₂ content ranges between 16.3% and 23.5%. The weight loss of pure calcium carbonate decomposition is 44% and lower percentages of weight loss indicate variable amounts of other compounds as LDH minerals. Therefore, mortars with no or little structurally-bound water (OH⁻) and high carbon dioxide content are potentially adequate for radiocarbon dating since they reflect the absence of other carbonate phases apart from calcite. Therefore, CP-2 and CP-19 are the most suitable mortars for radiocarbon dating since they display lower structurally-bound water and higher carbon dioxide content (Table 3).

Table 3. Thermo-gravimetric analysis results (wt %) of target fractions of mortar binders.

Sample	Pattern Type	H ₂ O _(ltp)	H ₂ O _(lil)	OH ⁻	CO ₃ ²⁻
CP-2-TF	A	1.46	1.35	10.40	23.47
CP-4-TF	A	2.86	1.82	12.8	16.28
CP-13-6-TF	B	2.30	2.78	19.64	18.46
CP-13-8-TF	B	1.89	2.28	15.41	23.04
CP-13-10-TF	B	1.89	2.12	17.01	21.83
CP-19-TF	A	2.54	1.41	10.31	23.29
CP-13-3-TF	B	2.77	2.45	13.56	18.06

ltp: interparticle, lil: interlayer, TF: target fraction. Pattern type as referred in Figure 10.

Since sample CP-19 shows the lowest weight loss of structurally-bound water corresponding to the decomposition of LDH phases, it has been selected instead of sample CP-2. In order to verify the contaminant potential of LDHs, both fine fraction (particle size <2 μm) and target fraction (particle size between 0.5 and 2 μm) have been dated (Table 4).

Table 4. Results of AMS ¹⁴C dates for different grain-size fractions of mortar binder.

Lab Code	Sample	Binder Grain-Size	Conventional Age	δ ¹³ C	Calibrate Age (95.4%)
BETA375404	CP-19-TF	0.5–2 μm	1370 ± 30 BP	−16.5	Cal AD 640–675
BETA343295	CP-19-FF	<2 μm	2180 ± 40 BP	−21.3	Cal BC 380–160

TF: target fraction, FF: fine fraction.

The result of ¹⁴C dating of CP-19-FF is 2180 ± 40 BP corresponding to the calendar age of Cal BC 380–160 (Figure 11a) and the radiocarbon age of CP-19-TF is 1370 ± 30 BP, which corresponds to the calendar age of Cal AD 640–675 (Figure 11b). The obtained dates are older than expected since the first written chronicle of Portilla Castle is dated in 1040 AD. The age interval between the archaeological age and radiocarbon ages of the target fraction reflects the persistent presence of dead carbon contamination related with the CO₃²⁻ anion of hydrotalcite and hydrocalumite.

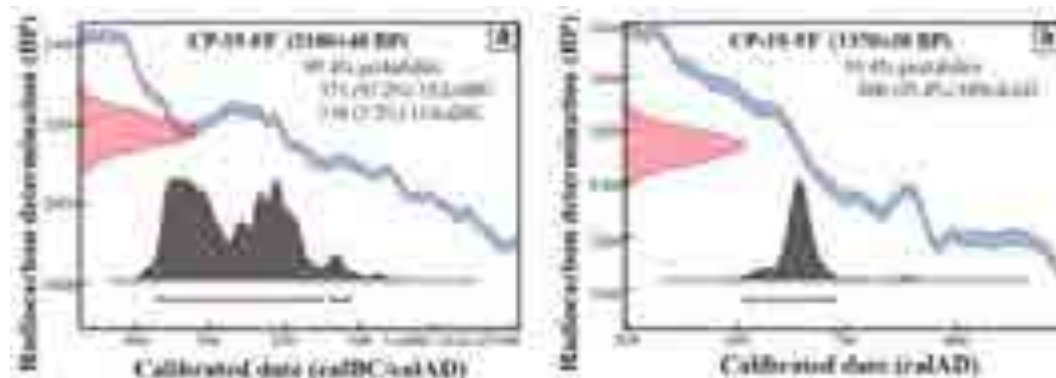


Figure 11. Calibrated ^{14}C dates of two fraction-sizes of the same lime mortar from Portilla Castle, (a) fine fraction (FF), and (b) target fraction (TF) obtained with OxCal v 4.1.7 [63] and IntCal09 atmospheric data [64].

The mineralogical composition of carbonate phases of the mortar binder and the granulometric distribution has determined the particle size to be extracted for radiocarbon dating. The selection of fine-grain size fraction ($<2\ \mu\text{m}$) is only useful when the mortar binder is formed solely by calcite, e.g., Ortega et al. [28]. In contrast, when the binder includes hydrotalcite and hydrocalumite besides neo-formation calcite, as in Portilla Castle, which determines the granulometric distribution of carbonate minerals is essential in selecting effective thresholds. Once the granulometric distribution is determined, the most suitable preconditioning method should be established for each sample in order to isolate the adequate fraction for radiocarbon dating. Therefore, dating of mortars without a comprehensive mineralogical study can lead to meaningless results.

5. Conclusions

Portilla Castle mortars are formed by calcitic binder and quartz, limestone fragments, some partially dolomitized, and unburnt limestone remains as aggregates. The presence of hydrotalcite and hydrocalumite in the fine grain fraction of binder indicates the use of impure limestone and/or partially dolomitized limestones in the lime production. These raw materials provide magnesium and aluminium ions and under hyper-alkaline conditions lead to the formation of LDHs phases during the slaking process.

The continuous mineralogical control of the extraction procedure allows a better mineralogical characterization of the finest grain fractions ($<2\ \mu\text{m}$) of the binder. Only the study of these fractions allows the identification of hydrotalcite and hydrocalumite in lime mortars. In this contribution, additional steps in the extraction process to remove small grain size particles enriched in LDHs has been performed making the obtained radiocarbon dates closer to the archaeological ages.

The occurrence of hydrotalcite and hydrocalumite mainly in the grain size is smaller than $0.5\ \mu\text{m}$ in the Portilla Castle mortars, which adds dead carbon to the system and explains older ages than expected. Therefore, hydrotalcite and hydrocalumite constitute crucial contaminant mineral phases in mortar dating issues.

Mineralogical studies are essential to select the samples for dating and reject unsuitable samples since they allow the mineralogical nature of the contaminants and the grain size distribution within the binder to be determined. Mineralogical studies of the binder have to develop tailored purification procedures for each sample.

Author Contributions: L.A.O. and M.C.Z. conceived and designed the experiments; J.L.S., G.P.-A. and L.A.O. selected archaeological materials, G.P.-A. performed the experiments; G.P.-A., L.A.O. and M.C.Z. analyzed the data; A.A.-O. contributed to the discussion; G.P.-A., L.A.O. and M.C.Z. wrote the paper.

Funding: This research was possible thanks to the financial support of SAI13/106 research project of Basque Country Government.

Acknowledgments: The authors would like to thank the anonymous referees for their comments and suggestions on the manuscript. GPA also acknowledges the PhD research grant of the Basque Country Government (2015-1-02-35). They also would like to thank Peter Smith for reviewing the use of English in the manuscript.

Conflicts of Interest: The authors declare no conflict of interest.

References

1. Schiffer, M. *Radiocarbon Dating and the “Old Wood” Problem: The Case of the Hohokam Chronology*; Elsevier: New York, NY, USA, 1986; Volume 13, pp. 13–30.
2. Mc Faden, B.G. Dating New Zealand archaeology by radiocarbon. *N. Z. J. Sci.* **1982**, *25*, 379–392.
3. Gavin, D.G. Estimation of inbuilt age in radiocarbon ages of soil charcoal for fire history studies. *Radiocarbon* **2001**, *43*, 27–44. [[CrossRef](#)]
4. Bowman, S. *Radiocarbon Dating*; British Museum Press: London, UK, 1990.
5. Taylor, R.; Bar-Yosef, O. *Radiocarbon Dating: An Archaeological Perspective*; Left Coast Press: Walnut Creek, CA, USA, 2014.
6. Boaretto, E.; Poduska, K.M. Materials science challenges in radiocarbon dating: The case of archaeological plasters. *J. Mater.* **2013**, *65*, 481–488. [[CrossRef](#)]
7. Kingery, D.W.; Pamela, B.V.; Martha, P. *The Beginnings of Pyrotechnology, Part II: Production and Use of Lime and Gypsum Plaster in the Pre-Pottery Neolithic Near East*; Taylor and Francis: New York, NY, USA, 1988; Volume 15, pp. 219–243.
8. Labeyrie, J.; Delibrias, G. Dating of old mortar by Carbon-14 method. *Nature* **1964**, *201*, 742–743. [[CrossRef](#)]
9. Stuiver, M.; Smith, C.S. *Radiocarbon Dating of Ancient Mortar and Plaster, Proceedings of the 6th International ¹⁴C Conference, Montreal, Canada, 8–15 September 1965*; Chatters, R.M., Olson, C.A., Eds.; Clearinghouse for Federal Scientific and Technical Information: Springfield, IL, USA; pp. 338–343.
10. Pachiaudi, C.; Marechal, J.; Van Strydonck, M.; Dupas, M.; Dauchotdehon, M. Isotopic fractionation of carbon during CO₂ absorption by mortar. *Radiocarbon* **1986**, *28*, 691–697. [[CrossRef](#)]
11. Ambers, J. Stable carbon isotope ratios and their relevance to the determination of accurate radiocarbon dates for lime mortars. *J. Archaeol. Sci.* **1987**, *14*, 569–576. [[CrossRef](#)]
12. Baxter, M.S.; Walton, A. Radiocarbon dating of mortars. *Nature* **1970**, *225*, 937–938. [[CrossRef](#)] [[PubMed](#)]
13. Folk, R.L.; Valastro, S.J. Successful technique for dating of lime mortar by carbon-14. *J. Field Archaeol.* **1976**, *3*, 203–208. [[CrossRef](#)]
14. Van Strydonck, M.; Dupas, M.; Dauchot-Dehon, M. *Radiocarbon dating of old mortars, ¹⁴C and Archaeology, Proceedings*; Mook, W.G., Waterbolk, H.T., Eds.; PACT: Phnom Penh, Cambodia, 1983; pp. 337–343.
15. Van Strydonck, M.; Dupas, M.; Dauchotdehon, M.; Pachiaudi, C.; Marechal, J. The influence of contaminating (fossil) carbonate and the variations of delta-C-13 in mortar dating. *Radiocarbon* **1986**, *28*, 702–710. [[CrossRef](#)]
16. Van Strydonck, M.J.Y.; Van der Borg, K.; De Jong, A.F.M.; Keppens, E. Radiocarbon dating of lime fractions and organic material from buildings. *Radiocarbon* **1992**, *34*, 873–879. [[CrossRef](#)]
17. Lindroos, A.; Heinemeier, J.; Ringbom, Å.; Braskén, M.; Sveinbjörnsdóttir, Á. Mortar dating using AMS ¹⁴C and sequential dissolution: Examples from medieval, non-hydraulic lime mortars from the Åland Islands, SW Finland. *Radiocarbon* **2007**, *49*, 47–67. [[CrossRef](#)]
18. Sonninen, E.; Jungner, H. An improvement in preparation of mortar for radiocarbon dating. *Radiocarbon* **2001**, *43*, 271–273. [[CrossRef](#)]
19. Hale, J.; Heinemeier, J.; Lancaster, L.; Lindroos, A.; Ringbom, Å. Dating ancient mortar. *Am. Sci.* **2003**, *91*, 130–137. [[CrossRef](#)]
20. Nawrocka, D.; Michniewicz, J.; Pawlyta, J.; Pazdur, A. Application of radiocarbon method for dating of lime mortars. *Geochronometria* **2005**, *24*, 109–115.
21. Heinemeier, J.; Jungner, H.G.; Lindroos, A.; Ringbom, S.; von Konow, T.; Rud, N. AMS ¹⁴C dating of lime mortar. *Nucl. Instrum. Methods Phys. Res. Sect. B Beam Interact. Mater. Atoms* **1997**, *123*, 487–495. [[CrossRef](#)]
22. Tubbs, L.E.; Kinder, T.N. The use of AMS for the dating of lime mortars. *Nucl. Instrum. Methods Phys. Res. Sect. B Beam Interact. Mater. Atoms.* **1990**, *52*, 438. [[CrossRef](#)]
23. Toffolo, M.; Maeir, A.M.; Chadwick, J.R.; Boaretto, E. Characterization of contexts for radiocarbon dating: Results from the early Iron Age at Tell es-Safi/Gath, Israel. *Radiocarbon* **2012**, *54*, 371–390. [[CrossRef](#)]

24. Asscher, Y.; Lehmann, G.; Rosen, S.A.; Weiner, S.; Boaretto, E. Absolute dating of the late bronze to iron age transition and the appearance of philistine culture in qubur el-walaydah, southern Levant. *Radiocarbon* **2015**, *57*, 77–97. [[CrossRef](#)]
25. Rodriguez-Navarro, C.; Hansen, E.; Ginell, W.S. Calcium hydroxide crystal evolution upon aging of lime putty. *J. Am. Ceram. Soc.* **1998**, *81*, 3032–3034. [[CrossRef](#)]
26. Boynton, R.S. *Chemistry and Technology of Lime and Limestone*; John Wiley & Sons, Inc.: New York, NY, USA, 1980.
27. Zouridakis, N.M.; Saliege, J.F.; Person, A.; Filippakis, S.E. Radiocarbon dating of mortars from ancient greek palaces. *Archaeometry* **1987**, *29*, 60–68. [[CrossRef](#)]
28. Ortega, L.A.; Zuluaga, M.C.; Alonso-Olazabal, A.; Murelaga, X.; Insausti, M.; Ibañez-Etxeberria, A. Historic lime-mortar ¹⁴C dating of Santa María la Real (Zarautz, northern Spain): Extraction of suitable grain size for reliable ¹⁴C dating. *Radiocarbon* **2012**, *54*, 23–36. [[CrossRef](#)]
29. Marzaioli, F.; Lubritto, C.; Nonni, S.; Passariello, I.; Capano, M.; Terrasi, F. Mortar radiocarbon dating: Preliminary accuracy evaluation of a novel methodology. *Anal. Chem.* **2011**, *83*, 2038–2045. [[CrossRef](#)] [[PubMed](#)]
30. Marzaioli, F.; Nonni, S.; Passariello, I.; Capano, M.; Ricci, P.; Lubritto, C.; De Cesare, N.; Eramo, G.; Quirós Castillo, J.A.; Terrasi, F. Accelerator mass spectrometry ¹⁴C dating of lime mortars: Methodological aspects and field study applications at CIRCE (Italy). *Nucl. Instrum. Methods Phys. Res. Sect. B Beam Interact. Mater. Atoms* **2013**, *294*, 246–251. [[CrossRef](#)]
31. Folk, R.L.; Valastro, S. Successful Technique for Dating of Lime Mortar by Carbon-14. *J. Field Archaeol.* **1976**, *3*, 203–208. [[CrossRef](#)]
32. Goslar, T.; Nawrocka, D.; Czernik, J. Foraminiferous limestone in C-14 dating of mortar. *Radiocarbon* **2009**, *51*, 987–993. [[CrossRef](#)]
33. Heinemeier, J.; Ringbom, A.; Lindroos, A.; Sveinbjornsdottir, A.E. Successful AMS ¹⁴C dating of non-hydraulic lime mortars from the medieval churches of the Aland Islands, Finland. *Radiocarbon* **2010**, *52*, 171–204. [[CrossRef](#)]
34. Al-Bashaireh, K. Plaster and mortar radiocarbon dating of Nabatean and Islamic structures, South Jordan. *Archaeometry* **2013**, *55*, 329–354. [[CrossRef](#)]
35. Ringbom, A.; Lindroos, A.; Heinemeier, J.; Sonck-Koota, P. 19 years of mortar dating: Learning from experience. *Radiocarbon* **2014**, *56*, 619–635. [[CrossRef](#)]
36. Nonni, S.; Marzaioli, F.; Secco, M.; Passariello, I.; Capano, M.; Lubritto, C.; Mignardi, S.; Tonghini, C.; Terrasi, F. ¹⁴C mortar dating: The case of the medieval shayzar citadel, Syria. *Radiocarbon* **2013**, *55*, 514–525. [[CrossRef](#)]
37. Pesce, G.; Quarta, G.; Calcagnile, L.; D’Elia, M.; Cavaciocchi, P.; Lastrico, C.; Guastella, R. Radiocarbon dating of lumps from aerial lime mortars and plasters: Methodological issues and results from San Nicolò of Capodimonte church (Camogli, Genoa, Italy). *Radiocarbon* **2009**, *51*, 867–872. [[CrossRef](#)]
38. Pesce, G.L.A.; Ball, R.J.; Quarta, G.; Calcagnile, L. Identification, extraction, and preparation of reliable lime samples for ¹⁴C dating of plasters and mortars with the “pure lime lumps” technique. *Radiocarbon* **2012**, *54*, 933–942. [[CrossRef](#)]
39. Beruto, D.T.; Vecchiattini, R.; Giordani, M. Solid products and rate-limiting step in the thermal half decomposition of natural dolomite in a CO₂ (g) atmosphere. *Thermochim. Acta* **2003**, *405*, 183–194. [[CrossRef](#)]
40. Schork, J. Dolomitic Lime in the US. *J. Archit. Conserv.* **2012**, *18*, 7–25. [[CrossRef](#)]
41. Kuzel, H.-J.; Baier, H. Hydration of calcium aluminate cements in the presence of calcium carbonate. *Eur. J. Mineral.* **1996**, 129–142. [[CrossRef](#)]
42. Evans, D.G.; Slade, R.C.T. Structural aspects of layered double hydroxides. In *Layered Double Hydroxides*; Duan, X., Evans, D.G., Eds.; Springer: Berlin/Heidelberg, Germany, 2006; pp. 1–87.
43. Forano, C.; Hibino, T.; Leroux, F.; Taviot-Guého, C. Chapter 13.1 layered double hydroxides. *Dev. Clay Sci.* **2006**, *1*, 1021–1095.
44. Guo, Q.; Reardon, E.J. Calcined dolomite: Alternative to lime for minimizing undesirable element leachability from fly ash. *Ind. Eng. Chem. Res.* **2012**, *51*, 9106–9116. [[CrossRef](#)]
45. Miyata, S.; Okada, A. Synthesis of hydrotalcite-like compounds and their physico-chemical properties—The systems Mg²⁺-Al³⁺-SO₄²⁻ - and Mg²⁺-Al³⁺-CrO₄²⁻. *Clays Clay Min.* **1977**, *25*, 14–18. [[CrossRef](#)]

46. Miyata, S. Physico-chemical properties of synthetic hydrotalcites in relation to composition. *Clays Clay Min.* **1980**, *28*, 50–56. [[CrossRef](#)]
47. Miyata, S. Anion-exchange properties of hydrotalcite-like compounds. *Clays Clay Min.* **1983**, *31*, 305–311. [[CrossRef](#)]
48. Reichle, W.T. Synthesis of anionic clay minerals (mixed metal hydroxides, hydrotalcite). *Solid State Ionics* **1986**, *22*, 135–141. [[CrossRef](#)]
49. Cavani, F.; Trifirò, F.; Vaccari, A. Hydrotalcite type anionic clays, preparation, properties and applications. *Catal. Today* **1991**, *11*, 173–301. [[CrossRef](#)]
50. Mills, S.J.; Christy, A.G.; Génin, J.-M.R.; Kameda, T.; Colombo, F. Nomenclature of the hydrotalcite supergroup: Natural layered double hydroxides. *Mineral. Mag.* **2012**, *76*, 1289–1336. [[CrossRef](#)]
51. Kutus, B.; Gacsi, A.; Pallagi, A.; Palinko, I.; Peintler, G.; Sipos, P. A comprehensive study on the dominant formation of the dissolved Ca(OH)₂ (aq) in strongly alkaline solutions saturated by Ca(II). *RSC Adv.* **2016**, *6*, 45231–45240. [[CrossRef](#)]
52. Pallagi, A.; Tasi, A.; Gácsi, A.; Csáti, M.; Pálkó, I.; Peintler, G.; Sipos, P. The solubility of Ca(OH)₂ in extremely concentrated NaOH solutions at 25 °C. *Cent. Eur. J. Chem.* **2012**, *10*, 332–337. [[CrossRef](#)]
53. Reardon, E.J.; Della Valle, S. Anion sequestering by the formation of anionic clays: Lime treatment of fly ash slurries. *Environ. Sci. Technol.* **1997**, *31*, 1218–1223. [[CrossRef](#)]
54. Rosenberg, S.P.; Armstrong, L. Layered double hydroxides in the Bayer process: Past, present and future. In *Essential Readings in Light Metals*; Springer: Berlin, Germany, 2005; pp. 157–161.
55. Sipos, P. The structure of Al (III) in strongly alkaline aluminate solutions—A review. *J. Mol. Liq.* **2009**, *146*, 1–14. [[CrossRef](#)]
56. Gácsi, A.; Kutus, B.; Kónya, Z.; Kukovecz, Á.; Pálkó, I.; Sipos, P. Estimation of the solubility product of hydrocalumite-hydroxide, a layered double hydroxide with the formula of [Ca₂Al(OH)₆]OH·nH₂O. *J. Phys. Chem. Solids* **2016**, *98*, 167–173. [[CrossRef](#)]
57. Artioli, G.; Secco, M.; Addis, A.; Bellotto, M. 5 Role of hydrotalcite-type layered double hydroxides in delayed pozzolanic reactions and their bearing on mortar dating. In *Cementitious Materials: Composition, Properties, Application*; Walter de Gruyter: Berlin, Germany, 2017.
58. Siedel, H.; Michalski, S.; Ullrich, B. Characterisation of dolomitic lime mortars from the Benedictine monastery in Riesa, Saxony (Germany). In *Historic Mortars*; Springer: Dordrecht, The Netherlands, 2012; pp. 115–124.
59. Brandon, C.J.; Hohlfelder, R.L.; Jackson, M.D.; Oleson, J.P. *Building for Eternity: The History and Technology of Roman Concrete Engineering in the Sea*; Oxbow Books: Oxford, UK; Philadelphia, PA, USA, 2014.
60. Massazza, F. Pozzolana and pozzolanic cements. In *Lea's Chemistry of Cement and Concrete*, 4th ed.; Hewlett, P., Ed.; Elsevier-Butterworth-Heinemann: Oxford, UK, 1998; pp. 471–635.
61. Sagredo, I. *Navarra: Castillos que Defendieron el Reino (Tomo III) La Navarra Occidental, la Frontera del Mar Alava, Bizkaia, el Duranguesado, Guipuzkoa*; PAMIELA: Pamplona, Spain, 2007.
62. Solaun, J.L.; Azcárate, A. El castillo de Portilla (Zambrana, Alava). Origen y significado de una fortaleza plenomedieval en territorio alavés (siglos XI–XII). *Munibe Antropol.-Arkeol.* **2016**, *67*, 167–183.
63. Ramsey, C.B.; Scott, M.; van der Plicht, H. Calibration for archaeological and environmental terrestrial samples in the time range 26–50 ka cal BP. *Radiocarbon* **2013**, *55*, 2021–2027. [[CrossRef](#)]
64. Reimer, P.J.; Bard, E.; Bayliss, A.; Beck, J.W.; Blackwell, P.G.; Ramsey, C.B.; Buck, C.E.; Cheng, H.; Edwards, R.L.; Friedrich, M.; et al. IntCal13 and marine13 radiocarbon age calibration curves 0–50,000 years cal BP. *Radiocarbon* **2013**, *55*, 1869–1887. [[CrossRef](#)]
65. Casadio, F.; Chiari, G.; Simon, S. Evaluation of binder/aggregate ratios in archaeological lime mortars with carbonate aggregate: A comparative assessment of chemical, mechanical and microscopic approaches. *Archaeometry* **2005**, *47*, 671–689. [[CrossRef](#)]
66. Warkentin, B.P.; Maeda, T. Physical and mechanical characteristics of andisols. In *Soils with Variable Charge*; Theng, B.K.G., Ed.; New Zealand Society of Soil Science: Lower Hutt, New Zealand, 1980; pp. 281–302.
67. Langmuir, D. *Aqueous Environmental Geochemistry*; Prentice Hall: London, UK, 1997.
68. Grover, K.; Komarneni, S.; Katsuki, H. Synthetic hydrotalcite-type and hydrocalumite-type layered double hydroxides for arsenate uptake. *Appl. Clay Sci.* **2010**, *48*, 631–637. [[CrossRef](#)]
69. Bakolas, A.; Biscontin, G.; Moropoulou, A.; Zendri, E. Characterization of structural byzantine mortars by thermogravimetric analysis. *Thermochim. Acta* **1998**, *321*, 151–160. [[CrossRef](#)]

70. Paama, L.; Pitkänen, I.; Rönkkömäki, H.; Perämäki, P. Thermal and infrared spectroscopic characterization of historical mortars. *Thermochim. Acta* **1998**, *320*, 127–133. [[CrossRef](#)]
71. Moropoulou, A.; Bakolas, A.; Anagnostopoulou, S. Composite materials in ancient structures. *Cem. Concr. Compos.* **2005**, *27*, 295–300. [[CrossRef](#)]
72. Yang, W.; Kim, Y.; Liu, P.K.T.; Sahimi, M.; Tsotsis, T.T. A study by in situ techniques of the thermal evolution of the structure of a Mg-Al-CO₃ layered double hydroxide. *Chem. Eng. Sci.* **2002**, *57*, 2945–2953. [[CrossRef](#)]
73. León, M.; Díaz, E.; Bennici, S.; Vega, A.; Ordóñez, S.; Auroux, A. Adsorption of CO₂ on hydrotalcite-derived mixed oxides: Sorption mechanisms and consequences for adsorption irreversibility. *Ind. Eng. Chem. Res.* **2010**, *49*, 3663–3671. [[CrossRef](#)]



© 2018 by the authors. Licensee MDPI, Basel, Switzerland. This article is an open access article distributed under the terms and conditions of the Creative Commons Attribution (CC BY) license (<http://creativecommons.org/licenses/by/4.0/>).

APPENDIX I.2

Comparison of sample preparation procedures for mortar radiocarbon dating. Case study of Irulegi Castle (Navarre, Spain)

Graciela Ponce-Antón, Alf Lindroos, Åsa Ringbom, Luis Angel Ortega, Maria Cruz Zuluaga,
Irka Hajdas, Jesper Olsen, Juanxo Agirre Mauleon

Submitted to Quaternary Geochronology

Comparison of sample preparation procedures for mortar radiocarbon dating. Case study of Irulegi Castle (Navarre, Spain)

Abstract: A comparison of two different mechanical separation procedures, a settling process and sieving process, was performed in the samples preparation for radiocarbon dating of archaeological lime mortars from the Tower Keep at Irulegi Castle (Navarre, Spain). The different fractions obtained by the two different mechanical separation procedures were converted to carbon dioxide by sequential dissolution in order to compare the yielded ^{14}C ages. Fifteen AMS ^{14}C measurements were performed from the lime mortars, as well as for a tooth and a charcoal fragment embedded in the mortar. Samples obtained by the settling process (grain-size window of 0.5-2 μm) led to more accurate radiocarbon results than samples obtained by sieving (grain-size window of 46-75 μm). The results point to Irulegi Castle existing during the 10th century as well as to the renovation of the castle defences and different repairs in the Tower Keep during the 13th and 14th centuries. Mineralogical characterization of samples was essential when discussing the radiocarbon dating results. For this end, petrographic microscopy, X-ray diffraction, thermogravimetric analyses and cathodoluminescence analyses were performed.

Keywords: lime mortar; sample preparation; particle-size differentiation; mineralogy; radiocarbon dating

1. Introduction

Lime mortars are artificial materials used in masonry mainly composed of a mixture of a lime binder and aggregates, resulting in a plastic material with bonding properties. Mortar manufacture (Fig. 1) begins with the limestone burning in a limekiln; during the calcination process the calcium carbonate (CaCO_3) of limestone breaks down releasing carbon dioxide (CO_2) to give rise to calcium oxide (CaO) or quicklime. This quicklime is slaked with water to form portlandite $\text{Ca}(\text{OH})_2$ whereafter the resulting putty is mixed with aggregates to make the mortar. Once the mortar is applied in the masonry, it begins to harden and water evaporation and atmospheric carbon dioxide absorption take place, forming again CaCO_3 . When the neoformed calcite (CaCO_3) fixes the atmospheric CO_2 , the ^{14}C present in the atmosphere is also captured.

Determining the chronology of historical buildings is one of the main goals in interdisciplinary studies in building archaeology, particularly in the absence of written records of the first construction period of buildings. Since lime mortars are among of the most often used materials in historical/archaeological constructions it is a suitable material to be dated.

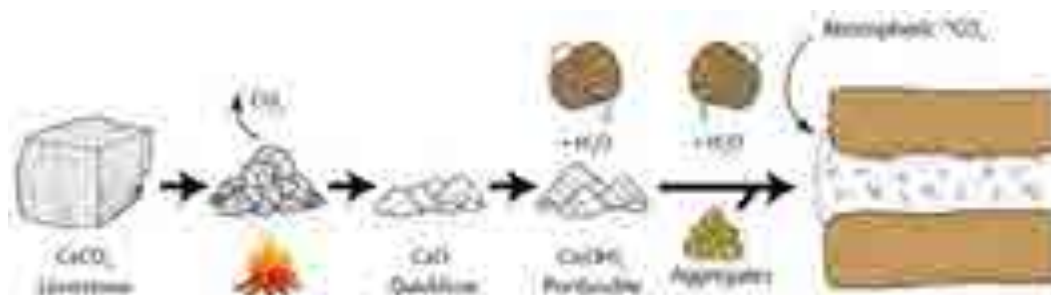


Fig. 1. Lime mortar manufacturing process (modified from Hale et al., 2003).

Lime mortars have been used for radiocarbon dating since the 1960s (Labeyrie and Delibrias, 1964; Stuiver and Smith, 1965). Nevertheless, carbonated aggregates and/or unburned limestone relicts present in the mortar constitute a contamination problem in mortar radiocarbon dating since introducing CO₂ of geological origin leads to an increase in radiocarbon ages (Baxter and Walton, 1970; Van Strydonck et al., 1986). In order to avoid contamination, different methodologies in sample preparation procedures have been reported (Folk and Valastro, 1976; Hajdas et al., 2017; Heinemeier et al., 1997; Heinemeier et al., 2010; Lindroos et al., 2007; Lindroos et al., 2018; Nawrocka et al., 2005; Ortega et al., 2012b; Ponce-Antón et al., 2018; Sonninen and Jungner, 2001; Van Strydonck et al., 1992).

Besides other materials could be accidentally incorporated into the mortar, such as bone or textile fragments. Since these organic aggregates are presumably coetaneous to the mortar manufacture they can be recovered and used as a proxy in the radiocarbon dating.

To obtain reliable radiocarbon dates it is not only necessary to isolate the binder fraction composed of neoformed calcite but also essential to select an adequate fine grain-size of binder to ensure particles of chemical origin (i.e. produced during the hardening process) and excluding particles of geological origin. Fine-grained particles only have a chemical origin and are formed by the flocculation and growth of colloids (Davis and Kent, 1990; Wilson and Spengler, 1996). Experimental studies on limestone grinding demonstrate that the finer grain-size fraction of the carbonates is absent in geological materials since particles dissolve quickly in natural waters due to weathering and transport processes (Ortega et al., 2012a).

Mortar binder does not only consist of neoformed calcite but can also contain other carbonated minerals formed during the hardening process. Therefore, accurate mineralogical characterization of each studied sample and each obtained sample-fraction is fundamental for radiocarbon dating (Ortega et al., 2012b; Ponce-Antón et al., 2018).

The aim of the present study is to compare two different sample preparations combined with sequential dissolution hydrolysis for mortar radiocarbon dating in order to contrast the obtained ¹⁴C ages. Sample preparations were based on settling and sieving of lime mortars. Accurate mineralogical and chemical characterizations of different grain size fractions were essential throughout both procedures. Three archaeological mortar samples from the Tower Keep of Irulegi Castle (Navarra, Spain) were selected for the comparison of the two sample preparation procedures and in order to determine the age of Irulegi Castle.

2. Archaeological background

Irulegi Castle was strategically located on Irulegi Hill on the eastern border of the Pamplona Basin (Navarre, Spain). The emplacement allowed the visual control of Pamplona, capital of the Kingdom of Navarre, and the transit route through the Pyrenees along the Izagaondoa valley during the Middle Ages (Fig. 2).

Irulegi Castle is characterized by a walled rectangular floor in which the Tower Keep stands out (Fig.3). Dismantling the south outer wall of the Tower Keep and the subsequent construction of the vertex-shaped structure transformed the original square floor of the tower into the current polygonal floor. Walls of the original square structure shows pseudoisodrom bonding built with high quality ashlar in which no constructive differences are observed, indicating that the original structure was built in the same construction period (Buces Cabello et al., 2013).

The archaeological site of Irulegi was settled continuously from the Late Bronze Age to the Late Middle Ages. However, neither written sources nor archaeological excavations have established the first construction period of Irulegi Castle; thus the origin of the castle is still unknown. The first mention of Irulegi Castle goes back to 1230 during the kingdom of Sancho VII of Navarre, «Michaele de Gueretz in Hyrulegui» (Goñi Gaztambide, 1997). However, Cañada Juste (1976) suggested that Irulegi Castle could be one of the defensive constructions destroyed by Abd Al-Rahman III in 924 during the military campaign against

Pamplona. Irulegi Castle was remodelled during the 12th, 13th and 14th centuries adding both defensive and residential elements. Written sources refer to different repairs on the Tower Keep in 1285, 1318, 1358 and 1371. The development of construction techniques over time led to important renovations on the defensive elements of the castle in the 1370s, resulting in renovation of the castle defences. The castle was demolished in 1494 since it was considered unnecessary for the defence of the Kingdom; «[...] una comisión dreçada a mossen Johan de Garro e al capitan Remonet para que fagan derribar el castillo de Urylegui [...]», «[...] e por el poco seruitio e hutilidad e prouecho quel dicho castillo fazia, vista que ninguna cosa aprovechava para en defension e guarda de nuestro regno lo hauemos fecho derribar», (« [...] a commission addressed to Monsignor Johan de Garro and to Captain Remonet to demolish the Urylegui Castle [...] », « [...] and for the little service and utility and benefit that this castle did, since it did not serve to defend and guard our kingdom, we have brought it down ») (AGN, 1494; Buces Cabello et al., 2013; Martinena Ruiz, 1980). After the castle was demolished in 1494 it was abandoned until the first archaeological excavation work in 2007.



Fig. 2. Geographic location of Irulegi Castle (Navarre, Spain).

3. Materials and Methods

3.1. Materials

Three archaeological non-hydraulic mortar samples from the Tower Keep of Irulegi Castle were selected (Fig.3 and Table 1) in order to obtain reliable historical ages. According to Heinemeier et al. (2010), the three samples (Samples CI-T-9, CI-T-10 and CI-T-13) come from a single building unit to ensure reliable results. A tooth and a charcoal fragment embedded in Sample CI-T-13 were also analysed.

Sampling is a fundamental issue in mortar radiocarbon dating. Therefore once sampling points were selected it was important not to take samples either at the surface or in the inner part of the walls. Sampling was avoided at the surface because the mortar weathering results in the precipitation of new carbonates and in the inner part because the inner mortars carbonated later and thus both samples would yield younger radiocarbon results.



Fig. 3. Location of studied samples in the Tower Keep at Irulegi Castle (modified from Ponce-Antón et al., 2019).

Table 1. List of sample fractions analysed by X-ray diffraction (XRD), thermogramimetric analyses (TGA) and cathodoluminescence (CL). Sample Code [i.e. CI-T-9B.1]: CI: Irulegi Castle, T: Tower, 9: Number of sample, B: grain-size (B: 46-75 μm grain-size window, T: 0.5-2 μm grain-size window); .1: The final number in the sample code corresponds to the number of the CO_2 fraction obtained by sequential solution.

Bulk mortar	Bulk mortar fraction (46-75 μm)	CO_2 fraction of Bulk mortar fraction	Binder mortar fraction (0.5-2 μm)	CO_2 fraction of Binder mortar fraction
CI-T-9	CI-T-9B	CI-T-9B.1	CI-T-9T	CI-T-9T.1
		CI-T-9B.2		CI-T-9T.2
		CI-T-9B.3		
CI-T-10	CI-T-10B	CI-T-10B.1	CI-T-10T	CI-T-10T.1
		CI-T-10B.2		CI-T-10T.2
		CI-T-10B.3		
CI-T-13	CI-T-13B	CI-T-13B.1	CI-T-13T	CI-T-13T.1
		CI-T-13B.2		CI-T-13T.2
		CI-T-13B.3		

3.2. Sample preparation

In order to isolate the neofomed calcite from the mortar binder, two sample preparation procedures were performed. Both sample preparations aim to avoid contamination due to carbonated aggregates and/or unburned limestone relicts present in the mortar. One of the sample preparations was based on the settling of mortar binder and the other on the sieving of crushed mortar (Fig.4). Selected preparation products from each procedure were hydrolysed by a sequential dissolution process (Fig.5).

The elementary principles of the procedures are widely described and detailed in Ortega et al. (2012b) and Ponce-Antón et al. (2018) for sample preparation by the settling process and in Lindroos et al. (2007) and Heinemeier et al. (2010) for sample preparation by the sieving process and a sequential dissolution process.

Before carrying out both processes, the upper surface of all mortar samples was removed using a scraper to eliminate the organic coating of inorganic crusts formed by atmospheric exposure and avoid additional contamination problems.

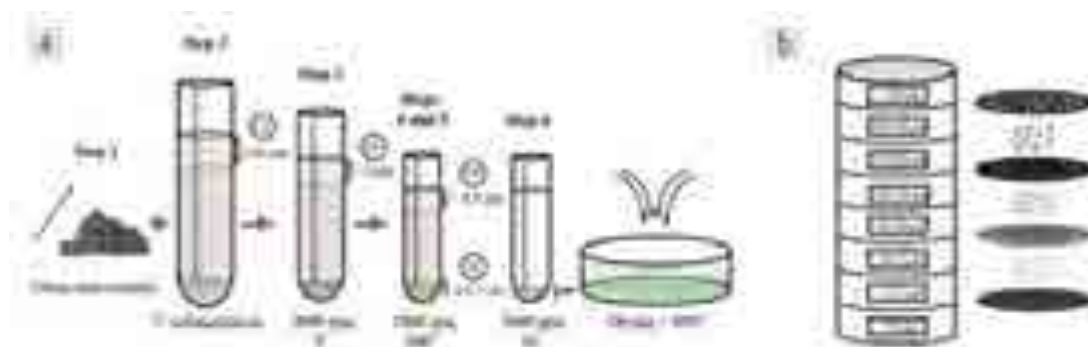


Fig. 4. Sample preparation procedures for mortar radiocarbon dating. (a) Sample preparation by the settling process (modified from Ponce-Antón et al., 2018). CF: coarse fraction, FF: fine fraction, UF: ultrafine fraction, TF: target fraction. Selected fraction corresponds to the 0.5-2 μm grain-size window (b) Sample preparation by the sieving process. Selected fraction corresponds to the 46-75 μm grain-size window.

3.2.1. Sample preparation procedure by a settling process

Sample preparation procedure by the settling process was performed in the Clay Minerals Laboratory at the University of the Basque Country (UPV/EHU) (Leioa, Spain). The procedure is based on a particle-fractionation technique used in soil and clay mineralogical studies (Laird and Dowdy, 1994; Soukup et al., 2008). Mortar samples were first manually disaggregated to avoid mechanical crumbling, preventing the homogenization of the grain size distribution and the formation of potential contaminating small grain-size particles of carbonated aggregates (de Groot, 2004). The organic components found embedded in the mortar were picked out, removed and preserved separately. Thereafter, to improve gentle sample disaggregation the ultrasonic bath for wet samples was used preserving the original grain-size. Different grain-size fractions were extracted by differential settling of the particles in ultrapure water buffered at $\text{pH} = 8$ by adding pure NH_4OH (Fig.4a). The 0.5-2 μm grain-size fraction of mortar binder was selected to perform sample hydrolysis by sequential dissolution for radiocarbon dating. Extraction procedure is repeated until sufficient binder is obtained for chemical-mineralogical and AMS analyses. Samples obtained by the settling preparation procedure have been named with a “T” at the end (Table 1).

3.2.2. Sample preparation procedure by a sieving process

Sample preparation procedure by the sieving process was performed in the Geology and Mineralogy Laboratory at Åbo Akademi University (Turku, Finland). Mortar samples were covered with a plastic film and crushed with pliers while dry. The crushed material was sieved in a sieve series with decreasing mesh size ranging between 20 and 500 μm (Fig.4b). The 46-75 μm grain-size fraction of bulk mortar was flushed with ultrapure water and selected to perform sample hydrolysis by sequential dissolution for radiocarbon dating. Samples obtained by the settling preparation procedure have been named with a “B” at the end (Table 1).

3.2.3. Sample hydrolysis by sequential dissolution

Between 38 and 44 mg of sample obtained by the settling process (0.5-2 μm grain-size window) and 80 mg of sample obtained by the sieving process (46-75 μm grain-size windows) were used for sample hydrolysis by sequential dissolution (Fig.5). Preparation products from each procedure were digested in 5 ml of 85% phosphoric acid (H_3PO_4) at room temperature (from 20 to 25°C). The CO_2 generated by the chemical reaction was isolated in several fractions. The time of dissolution for each fraction varies until a minimum of 0.2 mg

of C is reached in the vial. For samples obtained by the settling process the first two successive CO₂ fractions (a total of six CO₂ fractions) were isolated, and for samples obtained by sieving the first three successive CO₂ fractions (a total of nine CO₂ fractions) were isolated. The isolated CO₂ fractions were used for radiocarbon dating.

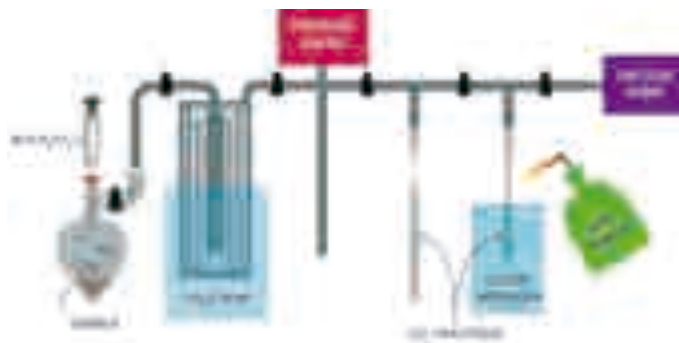


Fig. 5. Preparation line for sample hydrolysis by sequential dissolution (modified from Ringbom et al., 2014).

3.3. Methods

Hand sample observations were carried out by means of a Dino-Lite Premier AM7013MZT digital handheld microscope provided with a Microtouch II sensor for better observation of organic components embedded in the mortar. Magnification working distance was up to 200x and both measurements, acquisition and calibrations were carried out using DinoCapture 2.0 software.

A Nikon Eclipse LV100POL microscope equipped with a DS F-11 digital camera and DS L2 camera control unit was used for the petrographic studies of mortars. Mineralogical and microtextural characteristics of samples were analysed on polished thin-sections using both plane and crossed-polarized light modes.

The mineralogical composition of samples was determined by means of X-ray diffraction (XRD) using a Philips X'Pert diffractometer (Malvern PANalytical, Almelo, The Netherlands) in polycrystalline powder samples. The diffractometer was provided with a monochromatic Cu- α 1 X-radiation operating at 40 kV and 20 mA. The data collection was made by a continuous scan in the range 5-70° 2 θ , at an acquisition rate of 0.02° per second. Mineral phases identification was carried out with X'Pert HighScore Plus 3.0 software by PANalytical.

Thermogravimetric analysis (TGA) were carried out in a TA SDT 2960 TG-DSC thermogravimetric analyser (TA Instruments, New Castle, DE, USA) by heating 10 mg of powder sample at 10°C min⁻¹ from room temperature (from 20 to 25°C) to 900 °C under air atmosphere in a Pt crucible.

Cathodoluminescence (CL) was performed in powder sample by using a Technosyn Cold Cathode unit–luminescence 8200 MK II attached to an Olympus BH–II microscope equipped with an Olympus Camedia C 7070 camera.

The carbonation test was carried out for the visual assessment of the mortar carbonation degree using a phenolphthalein indicator solution (2% in ethanol).

Radiocarbon dating of samples was performed by means of Accelerator Mass Spectrometry (AMS) in the Laboratory for Ion Beam Physics ETH (Zurich, Switzerland) (Synal, 2013; Synal et al., 2007) following the procedure described by Hajdas (2008). A charcoal fragment found embedded in the mortar was also dated in the Aarhus AMS Centre (AARAMS), Aarhus University (Aarhus, Denmark). Charcoal was pre-treated by the acid-alkali-acid (AAA) method prior to conversion to CO₂ (Bird et al., 1999). The ¹⁴C ages are

reported in conventional radiocarbon years BP (Before Present = AD 1950) according to the international convention (Stuiver and Polach, 1977). Calculated ^{14}C ages were corrected for natural isotopic fractionation based on the $^{14}\text{C}/^{13}\text{C}$ ratio measurement to be equivalent to the standard $\delta^{13}\text{C}$ value of -25‰ VPDB. The conventional ^{14}C ages were calibrated to calendar ages using the IntCal13 atmospheric calibration curve (Reimer et al., 2013) by means of OxCal v4.2.3 calibration software (Bronk Ramsey, 2017). The probability method was used to calculate the calibrated age ranges and will be reported at the 95.4 % confidence level (2σ). The reported $\delta^{13}\text{C}$ values are AMS derived values.

Collagen from a tooth found embedded in the mortar was extracted for radiocarbon dating using pre-cleaned ultra-filters of the Millipore Amicon Ultra-4 type with MW=30 kDa at the AARAMS (Brown et al., 1988).

4. Results and Discussion

Macroscopically all mortar samples showed a heterogeneous texture with small charcoal fragments dispersed in the binder-matrix (Fig.6a). Small bone fragments (Figs. 6b and c) and an animal tooth (Fig.7) visible to the naked eye were also found in Sample CI-T-13. The tooth was identified as a lower right first or second molar (M1, M2) of a sheep/goat (J. Rofes, pers. comm., January 2019).



Fig. 6. Organic fragments embedded in the Irulegi Castle lime mortars. (a) Representative charcoal fragment. (b) and (c) bone fragment from the Sample CI-T-13.



Fig. 7. (a) Animal tooth embedded in the Sample CI-T-13. Images of the different faces of the tooth found embedded in the mortar binder matrix: (b) Occlusal face. (c) Apical face. (d) Buccal face. (e) Lingual face. (f) Mesial face. (g) Distal face.

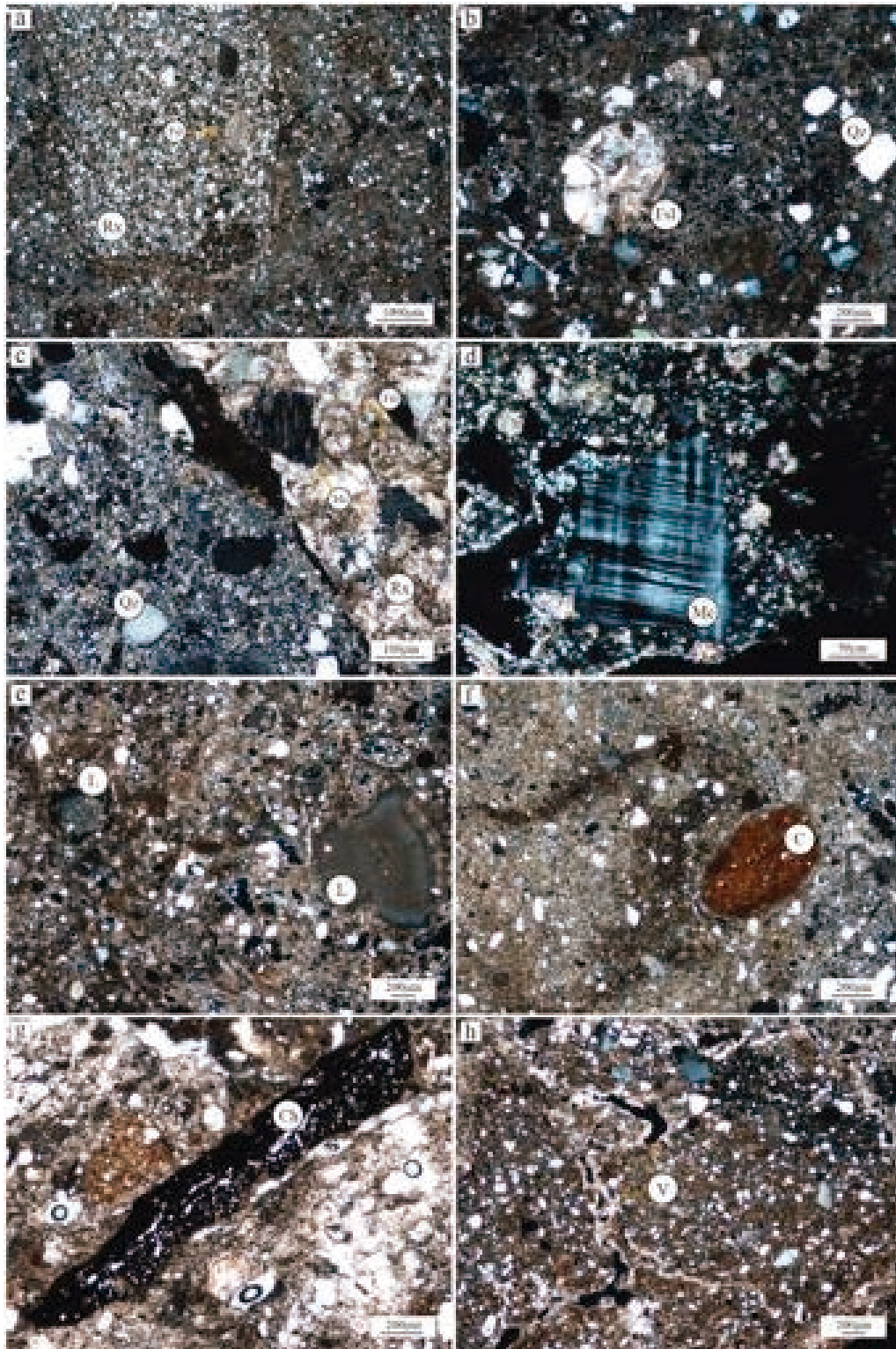


Fig. 8. Thin section photomicrographs in cross-polarized light, XPL and plane-polarized light, PPL. The most representative textures showing the heterogeneous binder matrix-supported texture of historic lime mortars from Irulegi Castle. (a) Subangular sandstone fragment (XPL). (b) Bryozoan fragment (XPL). (c) Sandstone aggregate showing microcline crystals (XPL). (d) Microcline crystal embedded in the binder-matrix (XPL). (e) Lime lumps embedded in the binder-matrix (XPL). (f) Rounded ceramic fragment embedded in the binder-matrix (XPL). (g) Charcoal fragment (PPL). (h) Secondary calcite crystals filling cavities (XPL). Qtz: quartz, Rx: Rock fragment, Fsl: fossil; Mc: microcline, L: Lump, C: ceramic, Ch: charcoal.

Thin sections of archaeological mortars were subjected to petrographic analyses under polarized-light microscopy in order to observe the overall mortar texture and to identify the binder and aggregates nature. All samples show a heterogeneous binder matrix-supported texture. All mortars are composed by a micritic calcite binder and angular to subangular quartz grains and heterometric fragments of sandstones, marls and calcarenites as aggregates (Fig. 8). Bioclast fragments (e.g. echinoderm plates, foraminifers and molluscs) and angular microcline crystals (K-feldspar) are observed scattered in the binder-matrix as a result of crushing the rocks used as aggregates, (Fig. 8a, b, c and d). Lumps < 1 mm in size, rounded ceramic fragments < 5 mm in size and charcoal fragments are also observed dispersed in the binder-matrix (Fig. 8e, f, g). The use of lime lumps for mortar radiocarbon dating (Lindroos et al., 2007; Lindroos et al., 2014; Lindroos et al., 2018; Pesce et al., 2009; Pesce et al., 2012; Van Strydonck et al., 1992) was not possible in Irulegi Castle mortars. The lime lumps were not sufficiently abundant or large enough to achieve the required amount of sample to ensure a reliable radiocarbon date. Additionally, secondary calcite crystals have been observed filling cavities, particularly in Sample CI-T-9 (Fig. 8h). Sample CI-T-13 shows scarce and small bone fragments as was also observed macroscopically (Fig. 9).



Fig. 9. Thin section photomicrographs of bone fragments in Sample CI-T-13. (a) in crossed-polarized light (b) in plane polarized light. (c) on the left in crossed-polarized light and on the right in plane polarized light. Bx: bone fragment.

To check sample alkalinity, the carbonation test was also carried out to assess the mortar carbonation degree visually since alkaline samples are problematic for mortar radiocarbon dating (Lichtenberger et al., 2015). According to the test results, samples were fully-carbonated since they remained colourless after reacting with the phenolphthalein, indicating a non-alkaline pH and therefore the absence of portlandite in the binder.

Table 1 summarizes the sample fractions obtained both by the sieving process (46-75 μm grain-size window named with a B) and settling process (0.5-2 μm grain-size window named with a T). Carbonation test was performed in all sample fractions before analyzing them by means of X-ray diffraction (XRD), thermogravimetric analyses (TGA), cathodoluminescence analysis (CL) and AMS analysis.

Calcite and quartz were the main mineral phases identified by XRD in all extracted fractions while K-feldspar and plagioclase were identified in minor amounts in samples CI-T-9B, CI-T-10B and CI-T-13B and as traces in Sample CI-T-9T (Fig. 10, Table 2). Traces of illite-like phyllosilicates were also present in Samples CI-T-9B, CI-T-10B and CI-T-13B and in minor amounts in Samples CI-T-9T, CI-T-10T and CI-T-13T.

Samples in the 46-75 μm grain-size window show higher amounts of quartz, K-feldspar and plagioclase compared with samples in the 0.5-2 μm grain-size window. K-feldspars and plagioclases come from the rock fragments used as aggregates (Fig. 8c). The larger amount of these phases indicates the presence of aggregate remains in the 46-75 μm grain-size window. Aggregate remains could be attributed to the small aggregate fragments mixed with the lime

putty in the mixing process and to the aggregate fragments resulting from bulk mortar crushing in the sample preparation by sieving.

Moreover, it should be noted that layered double hydroxide phases (LDHs) were not identified by XRD in either of the grain-size windows. LDHs have a high CO_3^{2-} anion capture capacity due to their ion-exchange properties that could improve the carbonation resistance of mortar (Ma et al., 2019; Miyata, 1983). Nevertheless, the identification of LDHs in samples for radiocarbon dating is essential. The high CO_3^{2-} affinity of LDHs makes them a potentially contaminating mineral phase group in mortar radiocarbon dating since they could incorporate CO_3^{2-} from the aggregates and introduce dead carbon into the system, thus ageing radiocarbon dates (Grover et al., 2010; Miyata, 1983; Ponce-Antón et al., 2018).

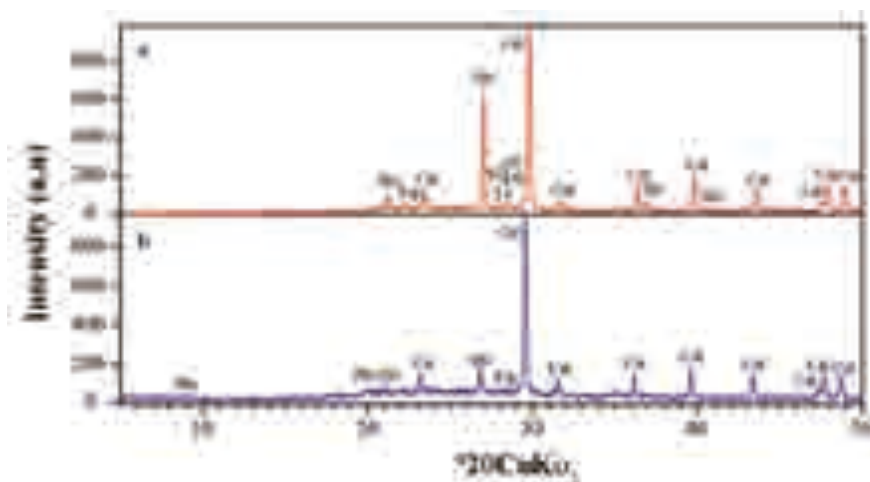


Fig. 10. X-ray diffraction patterns of the representative samples obtained by sieving and settling processes (a) sample obtained by sieving (46-75 μm grain-size window), (b) sample obtained by settling (0.5-2 μm grain-size window). Qtz: quartz, Cal: Calcite; Plg: plagioclase, K-Fsp: potassium feldspar, Fsp: feldspars s.l., Phy: illite-like phyllosilicates.

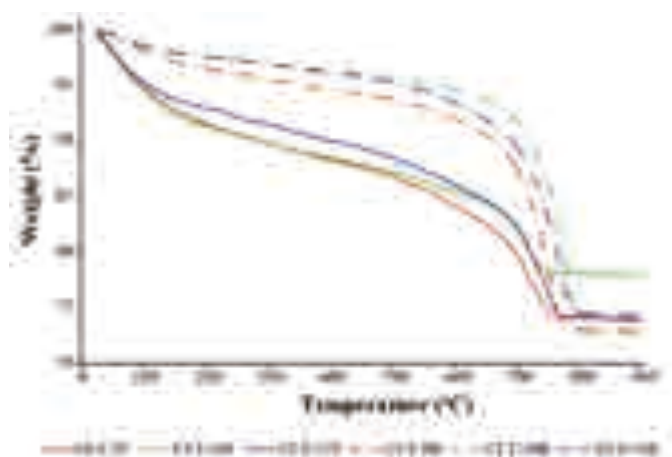


Fig. 11. Thermo-gravimetric analyses (TGA) of the different bulk mortar fractions and binder fractions obtained by sieving (46-75 μm grain-size window) and by settling (0.5-2 μm grain-size window), respectively.

Thermogravimetric analyses (TGA) of studied fractions show a continuous thermogravimetric profile with four main weight losses (Fig.11). Initial weight loss takes place between room temperature (from 20 to 25°C) and 120 °C due to the presence of adsorption water (inter-particle water) while the second weight loss between 120 °C and

200 °C was attributed to the crystallization water (interlayer water). The third weight loss between 200 °C and 600°C corresponds to dehydroxylation resulting from the loss of the structural hydroxyl groups (OH⁻). The fourth and most important weight loss occurs at temperatures above 600 °C when the CO₂ is lost due to the carbonates decomposition (Bakolas et al., 1998; Moropoulou et al., 2005; Paama et al., 1998).

Samples in the 0.5-2 µm grain-size window (CI-T-9T, CI-T-10T and CI-T-13T) show a total weight loss varying from 22% to 26.1%, while samples in the 46-75 µm grain-size window (CI-T-9B, CI-T-10B and CI-T-13B) from 25.4% to 27.1%. The presence of the phyllosilicates identified by XRD was confirmed by TGA. The weight loss in the temperature range of 400 °C to 550 °C in the thermogravimetric curve is associated with phyllosilicate dehydroxylation and varies with structure and composition (Cheng and Heidari, 2017; Drits and McCarty, 2007; Grim, 1962). Water-retention capacity of phyllosilicates has led to a high weight loss of the adsorption water and interlayer water varying from 7.1% to 8.7% in samples in the 0.5-2 µm grain-size window, while the weight loss in the 46-75 µm grain-size window ranges from 2.4% to 3.5%. Above 600 °C, the weight loss related to carbonates decomposition ranges between 7.4% and 12.11% for samples in the 0.5-2 µm grain-size window and from 18.9% to 21.9% for samples in the 46-75 µm grain-size window.

LDHs have not been identified by XRD because they could be under the detection limit of the analytical method. Nevertheless, the TGA confirms the absence of LDHs in all studied samples. The two continuous weight losses between 200 and 500 °C related to OH⁻ groups loss bonded to Al³⁺ and to Mg²⁺ corresponding to the LDHs thermal decomposition were not observed (Ficicilar and Dogu, 2006; León et al., 2010; Ma et al., 2019; Yang et al., 2002).

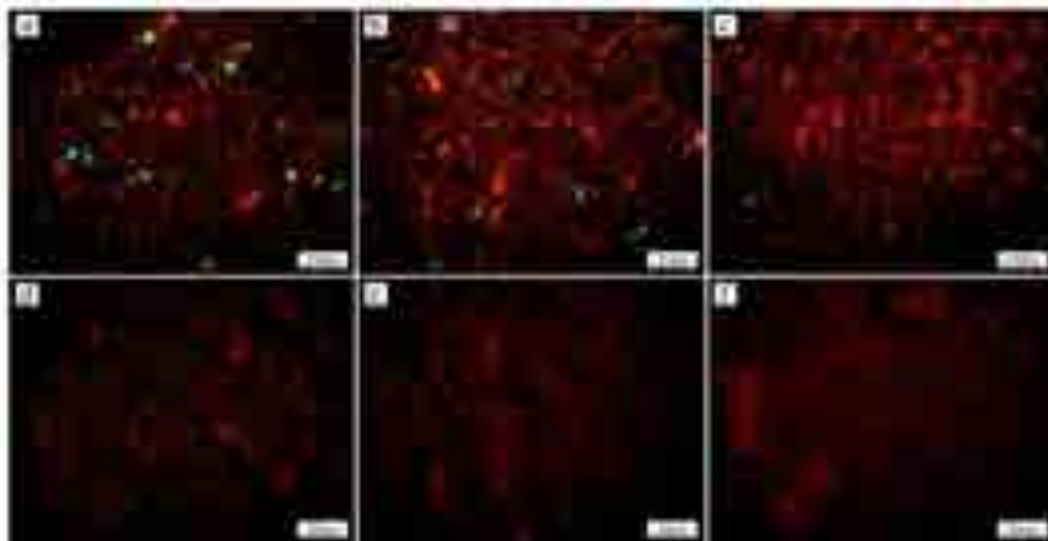


Fig. 12. Cathodoluminescence (CL) photomicrographs of bulk mortar fractions and binder mortar fractions. (a) Sample CI-T-9B. (b) Sample CI-T-10B. (c) Sample CI-T-13B. (d) Sample CI-T-9T. (e) Sample CI-T-10T. (f) Sample CI-T-13T. Blue: quartz or K-feldspar. Greenish-yellow: plagioclase. Tile-red: binder calcite. Red-orange: carbonated aggregates of geogenic origin

The CL analyses support the mineralogical composition determined by XRD and verified by TGA. Calcitic mortar binders of fractions obtained by settling and sieving show a tile-red to dark brown luminescence colour in CL (Fig. 12). Grains with a bright red-orange luminescence colour associated with carbonated aggregates of geogenic origin are observed in the 46-75 µm bulk mortar fraction samples (Fig.12a, b and c) while in the 0.5-2 µm binder fraction samples they are not observed (Fig. 12d, e and f). The blue luminescence of K-feldspar differs from the greenish-yellow colour of plagioclases (Götze et al., 2000) but blue luminescence can also be related to quartz grains. Samples CI-T-10T and CI-T-13T show

a scarce presence or even absence of carbonated aggregates, quartz, K-feldspar and plagioclase grains.

The use of CL microscopy alone is not sufficient for mineral determination (Pagel et al., 2000). Colour observation in CL makes mineralogical interpretation difficult since differences in luminescence colours can also be a result of small variations in the composition of a mineral (Marshall, 1988). Nevertheless, CL was useful to identify the carbonated aggregate remains (bright orange luminescence) since by XRD and TGA the calcite from carbonated aggregates (geogenic calcite) cannot be differentiated from the neoformed calcite. The CL analyses show the presence of geogenic calcite in the bulk mortar fraction samples in the 46-75 μm grain-size window obtained by sieving but not in the binder fraction samples in the 0.5-2 μm grain-size window obtained by settling. The presence of geogenic calcite (carbonated aggregates) in samples in the 46-75 μm grain-size window would explain the higher carbonate content in the TGA analyses (Fig. 11). Geogenic calcite contributes to sample contamination since during sample hydrolysis it incorporates geological carbon into the system resulting in an ageing of radiocarbon dates.

Table 2. Results of the mineralogical composition of bulk mortar fractions and binder mortar fractions determined by X-ray diffraction. Cal: calcite, Qz: quartz, Fsp: feldspars s.l.; Phy: illite-like phyllosilicates ****: predominant compounds; ***: high proportion; **: medium proportion; *: low proportion; tr: trace; -: undetected.

Sample Mineralogy	CI-T-9B	CI-T-10B	CI-T-13B	CI-T-9T	CI-T-10T	CI-T-13T
	Size fraction 46-75 μm			Size fraction 0.5-2 μm		
Cal	***	***	***	****	****	****
Qz	**	**	**	*	*	*
Fsp	*	*	*	tr	-	-
Phy	tr	tr	tr	*	*	*

Bulk mortar fractions (46-75 μm grain-size window) and binder mortar fractions (0.5-2 μm) were hydrolysed and three and two CO_2 fractions were obtained, respectively (Table 2, Fig. 5). Each isolated CO_2 fraction was analysed by AMS for radiocarbon dating. A total of fifteen AMS ^{14}C measurements from three mortar samples from the Tower Keep of the Irulegi Castle were performed, six from bulk mortar fractions obtained by settling and nine from mortar binder fractions obtained by sieving.

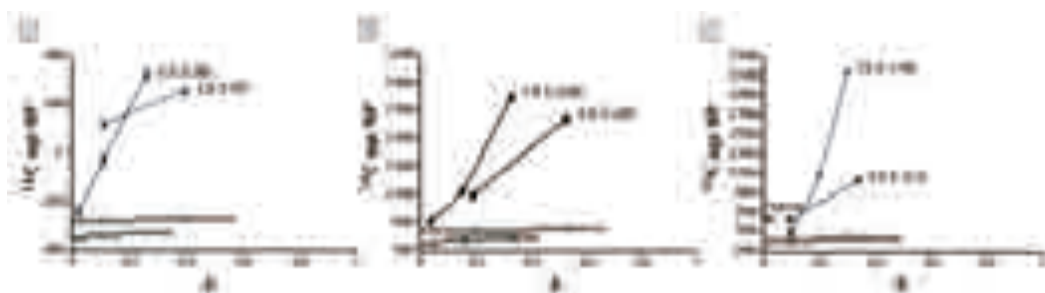


Fig. 13. ^{14}C age profiles of obtained fractions from three mortar samples from the Tower Keep at Irulegi Castle. Grey bars along the abscissas show the relative size of each CO_2 increment. F: dissolution progress (scale 0 to 1 instead of 0 to 100%).

The ^{14}C age profiles are named as B-profiles for samples in the 46-75 μm grain-size window and T-profiles for samples in the 0.5-2 μm grain-size window (Fig. 13). The B-profiles show a vertical trend whereas T-profiles display a more horizontal trend. The ^{14}C age profiles with more horizontal trends indicate less contamination in the samples

(Heinemeier et al., 2010; Lindroos et al., 2007). Since the T-profiles are flatter than the B-profiles it would show that more contaminants were removed by settling than by sieving, as was observed by CL analyses (Fig. 12).

Table 3 and Figure 14 show the obtained radiocarbon dating results in conventional radiocarbon ages (BP), calibrated into calendar ages (AD) and reported at the 95.4 % confidence level (2σ).

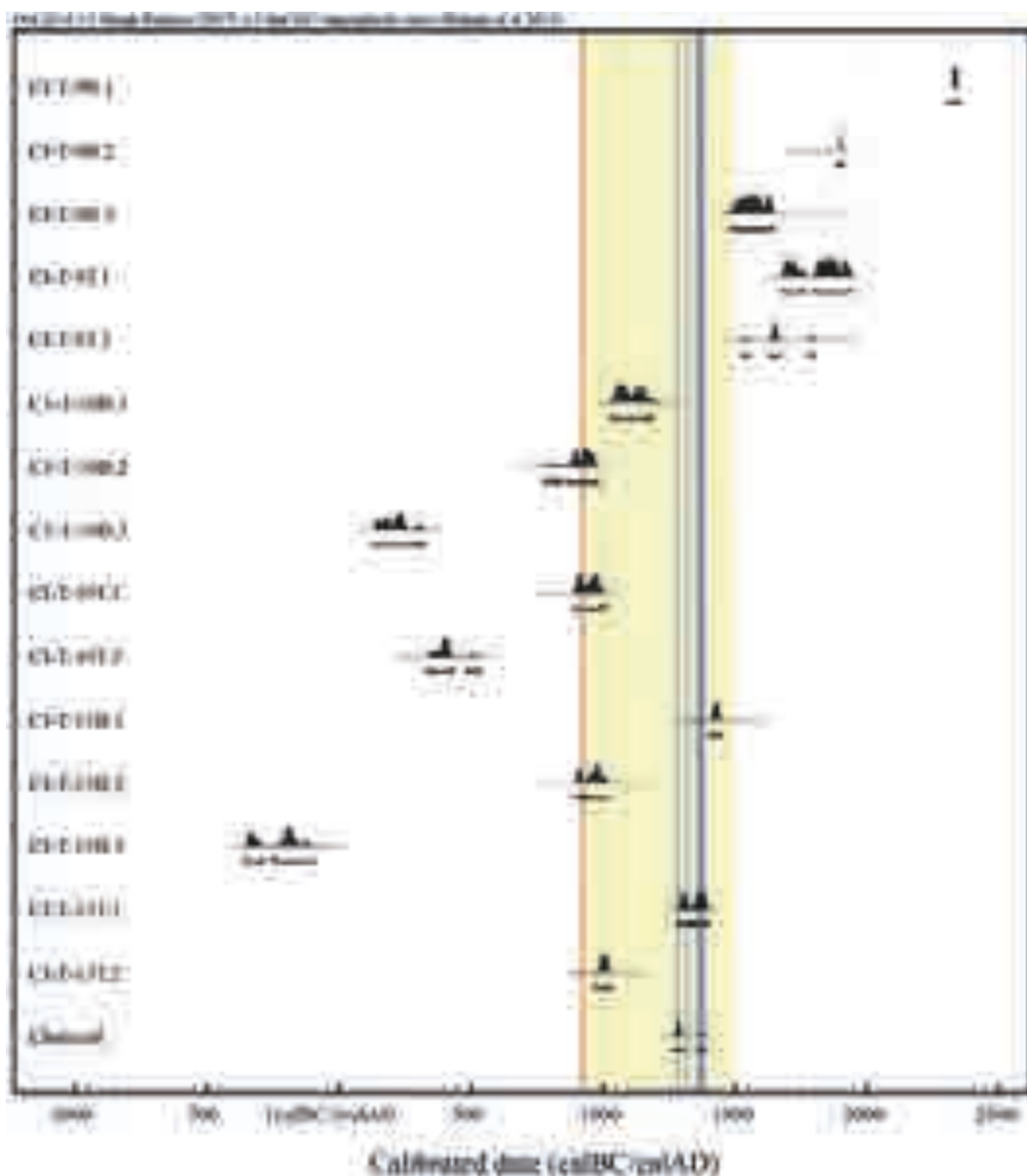


Fig. 14. Calendar calibration of AMS ^{14}C dates of bulk mortar fractions, binder mortar fractions and a charcoal fragment. In red, the military campaign of Abd Al-Rahman III in 924. In blue, the different repairs carried out in the Tower Keep and the decade of castle defence renovation. Sample code explanation in Table 1.

Secondary calcite observed within the mortar could explain the rejuvenated dates (Fig. 8h). Presence of portlandite ($\text{Ca}(\text{OH})_2$) would indicate the alkaline nature of the sample which would react with the more recent atmospheric carbon dioxide forming secondary calcite that would yield rejuvenated radiocarbon dates. Nevertheless portlandite was not detected in the alkalinity test nor identified by XRD. Furthermore, natural meteoric water incorporates atmospheric CO_2 , leading to a decrease in pH and the acidification of water.

Percolation of this acidified water into the masonry and its circulation through the mortar could lead to the partial dissolution of calcitic binder and the subsequent secondary calcite precipitation within cavities (Langmuir, 1997; MacLeod et al., 1990, 1991).

Although the studied samples were very closely located to each other Sample CI-T-9 show greater secondary calcite than Samples CI-T-10 and CI-T-13. Considering the porous system of these materials, the high interconnection between the pores in Sample CI-T-9 could favour meteoric water flow inside the mortar (Ponce-Antón et al., 2019).

Table 3. Results of AMS ^{14}C dates for different isolated CO_2 fractions of bulk mortar fractions (46-75 μm grain-size window, named with a “B”) and binder mortar fractions (0.5-2 μm grain-size window, named with a “T”). Sample code explanation in Table 1. Conventional radiocarbon ages (BP) are calibrated into calendar ages (AD) and reported at the 95.4 % confidence level (2σ) giving the probability in brackets. Charcoal fragment ^{14}C data is also reported. AD: Anno Domini. BP: Before present (present = AD 1950).

Sample	Grain-size (μm)	Weight (mg)	Reaction Time (s)	C content (mg)	^{14}C age (BP) (years)	$\pm 1\sigma$ (years)	Calibrated age (years)	$\delta^{13}\text{C}$ (‰)	Laboratory Nr
CI-T-9B.1	46-75	80	12	0.22	-240	27	Future age	-21	ETH-89320
CI-T-9B.2			30	0.51	-31	23	1891-1909 (95.4)	-17.6	ETH-89329
CI-T-9B.3			100	0.77	324	25	1485-1644 (95.4)	-15.1	ETH-89330
CI-T-9T.1	0.5-2	43.9	6	0.28	119	25	1680-1764 (30.9)	-29.4	ETH-89547
CI-T-9T.2			16	0.48	256	22	1801-1939 (64.5) 1527-1553 (8.8) 1633-1669 (73.3) 1781-1799 (13.3)	-17.2	ETH-89548
CI-T-10B.1	46-75	80	21	0.22	911	26	1034-1186 (95.4)	-14.8	ETH-87870
CI-T-10B.2			41	0.46	1136	24	777-791 (3.1) 807-819 (1.5) 825-842 (2.5) 862-983 (88.3)	-17.7	ETH-87861
CI-T-10B.3			55	0.62	1801	24	132-258 (84.9) 284-290 (1.0) 295-322 (9.5)	-16.1	ETH-87862
CI-T-10T.1	0.5-2	38.3	16	0.22	1095	25	891-997 (94.2)	-20.4	ETH-89549
CI-T-10T.2			45	0.17	1645	27	1007-1012 (1.2) 335-433 (85.9) 489-533 (9.5)	-11.5	ETH-89550
CI-T-13B.1	46-75	80	21	0.22	491	28	1406-1449 (95.4)	-19.5	ETH-89321
CI-T-13B.2			36	0.41	1082	25	895-929 (27.7) 940-1017 (67.7)	-11.0	ETH-89322
CI-T-13B.3			56	0.73	2155	27	356-285 (35.9) 253-250 (0.3) 235-100 (59.3)	-8.1	ETH-89331
CI-T-13T.1	0.5-2	43.1	8	0.22	633	26	1286-1329 (39.0) 1340-1397 (56.4)	-25.0	ETH-89551
CI-T-13T.2			23	0.41	1033	24	973-1030 (95.4)	-14.8	ETH-89552
Charcoal					691	22	1270-1305 (78.3) 1365-1385 (17.1)	-25	AAR-28207

The conventional radiocarbon age of the first CO_2 fraction of sample CI-T-10T (CI-T-10T.1) was 1095 ± 25 BP corresponding to the calendar age cal AD 891-997 (at 94.2% probability). The second CO_2 fraction from Sample CI-T-10B (CI-T-10B.2) yielded a ^{14}C age of 1136 ± 24 BP, which corresponds to the calendar age cal AD 862-983 at 88.3% probability, slightly older than the ^{14}C age of Sample CI-T-10T.1. Beside, Cañada Juste (Cañada Juste, 1976) suggested Irulegi Castle was one of the defensive constructions destroyed by Abd Al-Rahman III in 924 during the military campaign against Pamplona. Therefore, the ^{14}C AMS results obtained for Samples CI-T-10T.1 and CI-T-10B.2 would support that the castle was already built in the 10th century.

The radiocarbon date for the first CO₂ fraction from Sample CI-T-13T (CI-T-13T.1) yielded a ¹⁴C age of 633 ± 26 BP, which corresponds to the calendar ages cal AD 1286-1329 at 39% probability and cal AD 1340-1397 at 56.4% probability. Furthermore, radiocarbon dating of the charcoal fragment found embedded in Sample CI-T-13 (Fig. 7a) yielded the ¹⁴C age of 691 ± 22 BP, which corresponds to the calendar ages cal AD 1270-1305 at 78.3% probability and cal AD 1365-1385 at 17.1% probability. The tooth found embedded in Sample CI-T-13 was also dated (Fig. 7) yielded the ¹⁴C age of 1453 ± 75 BP corresponding to the calendar ages cal AD 538-660 at 68.2% probability and cal AD 420-686 at 95.4% probability. Nevertheless, the radiocarbon dating of the tooth was not reliable since the C content after ultrafiltration was scarce (0.1 mg C) because of the deficient preservation of the tooth and the poor quality of the extracted collagen. The ¹⁴C age of Sample CI-T-13T.1 is very close to the one obtained for the charcoal. The radiocarbon dating age ranges coincide with the historical written sources for the different repairs carried out in the Tower Keep in the 13th and 14th centuries (1285, 1318, 1358 and 1371) but also with the renovation of the castle defences in the 1370s (Buces Cabello et al., 2013). The location of Sample CI-T-13 was close to the south outer wall of the Tower Keep, which could be part of the area involved in the vertex-shaped structure construction (Fig. 3). Thus, it is not possible to dismiss either of the two calendar ages obtained.

A sample in the 0.5-2 µm grain-size window obtained by the settling process gave a radiocarbon result closer to the expected documented historical ages than the samples in the 46-75 µm grain-size window obtained by sieving process. According to the obtained chemical-mineralogical and radiocarbon results, the settling process resulted more efficient than sieving process at removing contaminants since it yielded finer grain-size particles and avoided the presence of geogenic carbonates.

5. Conclusions

A comparison of two mechanical sample preparation procedures for mortar radiocarbon dating was performed with lime mortar samples from the Tower Keep in Irulegi Castle.

The settling process resulted more efficient than the sieving process since a finer grain-size prevents the presence of mechanical particles of geogenic origin, leading to radiocarbon results closer to the expected historical ages.

Radiocarbon dating results would imply the assumption that Irulegi Castle was already built in the 10th century and are in agreement with the repairs carried out in the Tower Keep and the renovations in the castle defences during the 13th and 14th centuries.

Rejuvenated ages were obtained because of the presence of secondary calcite while the aged results were due to the presence of geogenic calcite.

Mineralogical and chemical characterization of samples is essential to assess the results obtained by radiocarbon dating. Not only sample grain-size but also the sample preparation procedure is important to obtain reliable radiocarbon ages.

Acknowledgments: This work was supported financially by GIC18/133 Research Group of the University of the Basque Country (UPV/EHU) and the International Mortar Dating Project supported by The Academy of Finland, The Finnish Society of Sciences and Letters, The Foundation for Åbo Akademi University Research Institute and The Åland Cultural Foundation. G.P.-A. also acknowledges the PhD research grant of the Basque Government [2015-1-02-35]. The authors would like to thank Peter Smith for reviewing the use of English in the manuscript.

Declaration of Competing Interest: The authors declare no conflict of interest.

References

- AGN, 1494. Royal and General Archive of Navarre, Comptos Section. Box 165, N. 80, ff. 51v and 71v.
- Bakolas, A., Biscontin, G., Moropoulou, A., Zendri, E., 1998. Characterization of structural byzantine mortars by thermogravimetric analysis. *Thermochimica Acta* 321, 151-160.
- Baxter, M.S., Walton, A., 1970. Radiocarbon dating of mortars. *Nature* 225, 937-938.
- Bird, M.I., Ayliffe, L.K., Fifield, L.K., Turney, C.S., Cresswell, R.G., Barrows, T.T., David, B., 1999. Radiocarbon dating of "old" charcoal using a wet oxidation, stepped-combustion procedure. *Radiocarbon* 41, 127-140.
- Bronk Ramsey, C., 2017. Methods for summarizing radiocarbon datasets. *Radiocarbon* 59, 1809-1833.
- Brown, T.A., Nelson, D.E., Vogel, J.S., Southon, J.R., 1988. Improved collagen extraction by modified Longin method. *Radiocarbon* 30, 171-177.
- Buces Cabello, J., Moraza Barea, A., Agirre Mauleon, J., Pescador Medrano, A., Legorburu Arzamendi, M., 2013. Un enclave estratégico en la Cuenca de Pamplona: el castillo medieval de Irulegi (Lakidain, Navarra). Balance de los trabajos arqueológicos (2007-2012). *Trabajos de arqueología Navarra*, 143-170.
- Cañada Juste, A., 1976. La campaña musulmana de Pamplona. Año 924. Diputación Foral de Navarra, Institución Príncipe de Viana, Pamplona.
- Cheng, K., Heidari, Z., 2017. Combined interpretation of NMR and TGA measurements to quantify the impact of relative humidity on hydration of clay minerals. *Applied Clay Science* 143, 362-371.
- Davis, J.A., Kent, D.B., 1990. Surface complexation modeling in aqueous geochemistry, In: Hochella, M.F., White, A.F. (Eds.), *Mineral-Water Interface Geochemistry*. Mineralogical Society of America, pp. 177-260.
- de Groot, P.A., 2004. *Handbook of Stable Isotope Analytical Techniques*, Volume I. Elsevier.
- Drits, V.A., McCarty, D.K., 2007. The nature of structure-bonded H₂O in illite and leucophyllite from dehydration and dehydroxylation experiments. *Clays and Clay Minerals* 55, 45-58.
- Ficiclar, B., Dogu, T., 2006. Breakthrough analysis for CO₂ removal by activated hydrotalcite and soda ash. *Catalysis Today* 115, 274-278.
- Folk, R.L., Valastro, S.J., 1976. Successful technique for dating of lime mortar by carbon-14. *Journal of Field Archaeology* 3, 203-208.
- Goñi Gaztambide, J., 1997. Colección diplomática de la catedral de Pamplona 829-1243. Gobierno de Navarra, Pamplona.
- Götze, J., Krbetschek, M.R., Habermann, D., Wolf, D., 2000. High-resolution cathodoluminescence studies of feldspar minerals, *Cathodoluminescence in geosciences*. Springer, Berlin, pp. 245-270.
- Grim, R.E., 1962. *Applied clay mineralogy*. Mc Graw-Hill, New York.
- Grover, K., Komarneni, S., Katsuki, H., 2010. Synthetic hydrotalcite-type and hydrocalumite-type layered double hydroxides for arsenate uptake. *Applied Clay Science* 48, 631-637.
- Hajdas, I., 2008. The Radiocarbon dating method and its applications in Quaternary studies. *E&G Quaternary Science Journal* 57, 2-24.
- Hajdas, I., Lindroos, A., Heinemeier, J., Ringbom, Å., Marzaioli, F., Terrasi, F., Passariello, I., Capano, M., Artioli, G., Addis, A., Secco, M., Michalska, D., Czernik, J., Goslar, T., Hayen, R., Van Strydonck, M., Fontaine, L., Boudin, M., Maspero, F., Panzeri, L., Galli, A., Urvanová, P., Guibert, P., 2017. Preparation and dating of mortar samples—Mortar Dating Inter-comparison Study (MODIS). *Radiocarbon* 59, 1845-1858.
- Hale, J., Heinemeier, J., Lancaster, L., Lindroos, A., Ringbom, Å., 2003. Dating ancient mortar. *American Scientist* 91, 130-137.
- Heinemeier, J., Jungner, H.g., Lindroos, A., Ringbom, Å., von Konow, T., Rud, N., 1997. AMS ¹⁴C dating of lime mortar. *Nuclear Instruments and Methods in Physics Research Section B: Beam Interactions with Materials and Atoms* 123, 487-495.
- Heinemeier, J., Ringbom, A., Lindroos, A., Sveinbjornsdottir, A.E., 2010. Successful AMS ¹⁴C dating of non-hydraulic lime mortars from the medieval churches of the Aland Islands, Finland. *Radiocarbon* 52, 171-204.
- Labeyrie, J., Delibrias, G., 1964. Dating of old mortar by Carbon-14 method. *Nature* 201, 742-743.

- Laird, D.A., Dowdy, R.H., 1994. Preconcentration techniques in soil mineralogical analyses, In: Luxmoore, R.J. (Ed.), *Quantitative Methods in Soil Mineralogy*. Soil Science Society of America, Madison, WI, pp. 236-266.
- Langmuir, D., 1997. *Aqueous Environmental Geochemistry*. Prentice Hall, Upper Saddle River, NJ.
- León, M., Díaz, E., Bennici, S., Vega, A., Ordóñez, S., Auroux, A., 2010. Adsorption of CO₂ on Hydrotalcite-Derived Mixed Oxides: Sorption Mechanisms and Consequences for Adsorption Irreversibility. *Industrial & Engineering Chemistry Research* 49, 3663-3671.
- Lichtenberger, A., Lindroos, A., Raja, R., Heinemeier, J., 2015. Radiocarbon analysis of mortar from Roman and Byzantine water management installations in the Northwest Quarter of Jerash, Jordan. *Journal of Archaeological Science: Reports* 2, 114-127.
- Lindroos, A., Heinemeier, J., Ringbom, Å., Braskén, M., Sveinbjörnsdóttir, Á., 2007. Mortar dating using AMS 14C and sequential dissolution: examples from medieval, non-hydraulic lime mortars from the Åland Islands, SW Finland. *Radiocarbon* 49, 47-67.
- Lindroos, A., Ranta, H., Heinemeier, J., Lill, J.O., 2014. 14C chronology of the oldest Scandinavian church in use. An AMS/PIXE study of lime lump carbonate in the mortar. *Nuclear Instruments and Methods in Physics Research Section B: Beam Interactions with Materials and Atoms* 331.
- Lindroos, A., Ringbom, Å., Heinemeier, J., Hodgins, G., Sonck-Koota, P., Sjöberg, P., Lancaster, L., Kaisti, R., Brock, F., Ranta, H., Caroselli, M., Lugli, S., 2018. Radiocarbon Dating Historical Mortars: Lime Lumps and/or Binder Carbonate? *Radiocarbon* 60, 875-899.
- Ma, J., Duan, P., Ren, D., Zhou, W., 2019. Effects of layered double hydroxides incorporation on carbonation resistance of cementitious materials. *Journal of Materials Research and Technology* 8, 292-298.
- MacLeod, G., Hall, A.J., Fallick, A.E., 1990. An applied mineralogical investigation of concrete degradation in a major concrete road bridge. *Mineralogical Magazine* 54, 637-644.
- MacLeod, G., Hall, A.J., Fallick, A.E., 1991. The mechanism of carbonate mineral growth on concrete structures as elucidated by carbon and oxygen isotope analyses. *Chemical Geology* 86, 335-343.
- Marshall, D.J., 1988. *Cathodoluminescence of Geological Materials*. Unwin Hyman, London.
- Martinena Ruiz, J.J., 1980. *Navarra castillos y palacios*. Caja de Ahorros de Navarra, Pamplona.
- Miyata, S., 1983. Anion-exchange properties of hydrotalcite-like compounds. *Clays and Clay Minerals* 31, 305-311.
- Moropoulou, A., Bakolas, A., Anagnostopoulou, S., 2005. Composite materials in ancient structures. *Cement and Concrete Composites* 27, 295-300.
- Nawrocka, D., Michniewicz, J., Pawlyta, J., Pazdur, A., 2005. Application of radiocarbon method for dating of lime mortars. *Geochronometria* 24, 109-115.
- Ortega, L.A., Zuluaga, M.C., Alonso-Olazabal, A., Insausti, M., Murelaga, X., Ibañez, A., 2012a. Improved Sample Preparation Methodology on Lime Mortar for Reliable ¹⁴C Dating. *Radiometric Dating*. In Tech, 3-20.
- Ortega, L.A., Zuluaga, M.C., Alonso-Olazabal, A., Murelaga, X., Insausti, M., Ibañez-Etxeberria, A., 2012b. Historic lime-mortar ¹⁴C dating of Santa María la Real (Zarautz, northern Spain): Extraction of suitable grain size for reliable 14C dating. *Radiocarbon* 54, 23-36.
- Paama, L., Pitkänen, I., Rönkkömäki, H., Perämäki, P., 1998. Thermal and infrared spectroscopic characterization of historical mortars. *Thermochimica Acta* 320, 127-133.
- Pagel, M., Barbin, V., Blanc, P., Ohnenstetter, D., 2000. Cathodoluminescence in geosciences: an introduction, *Cathodoluminescence in geosciences*. Springer, Berlin, pp. 1-21.
- Pesce, G., Quarta, G., Calcagnile, L., D'Elia, M., Cavaciocchi, P., Lastrico, C., Guastella, R., 2009. Radiocarbon Dating of Lumps from Aerial Lime Mortars and Plasters: Methodological Issues and Results from San Nicolò of Capodimonte Church (Camogli, Genoa, Italy). *Radiocarbon* 51, 867-872.
- Pesce, G.L.A., Ball, R.J., Quarta, G., Calcagnile, L., 2012. Identification, extraction, and preparation of reliable lime samples for ¹⁴C dating of plasters and mortars with the "pure lime lumps" technique. *Radiocarbon* 54, 933-942.
- Ponce-Antón, G., Arizzi, A., Zuluaga, M.C., Cultrone, G., Ortega, L.A., Agirre Mauleon, J., 2019. Mineralogical, Textural and Physical Characterisation to Determine Deterioration Susceptibility of Irulegi Castle Lime Mortars (Navarre, Spain). *Materials* 12, 584.

- Ponce-Antón, G., Ortega, L.A., Zuluaga, M.C., Alonso-Olazabal, A., Solaun, J.L., 2018. Hydrotalcite and Hydrocalumite in Mortar Binders from the Medieval Castle of Portilla (Álava, North Spain): Accurate Mineralogical Control to Achieve More Reliable Chronological Ages. *Minerals* 8, 326.
- Reimer, P.J., Bard, E., Bayliss, A., Beck, J.W., Blackwell, P.G., Ramsey, C.B., Buck, C.E., Cheng, H., Edwards, R.L., Friedrich, M., Grootes, P.M., Guilderson, T.P., Haflidason, H., Hajdas, I., Hatté, C., Heaton, T.J., Hoffmann, D.L., Hogg, A.G., Hughen, K.A., Kaiser, K.F., Kromer, B., Manning, S.W., Niu, M., Reimer, R.W., Richards, D.A., Scott, E.M., Southon, J.R., Staff, R.A., Turney, C.S.M., van der Plicht, J., 2013. IntCal13 and Marine13 Radiocarbon Age Calibration Curves 0–50,000 Years cal BP. *Radiocarbon* 55, 1869-1887.
- Ringbom, A., Lindroos, A., Heinemeier, J., Sonck-Koota, P., 2014. 19 years of mortar dating: learning from experience. *Radiocarbon* 56, 619-635.
- Sonninen, E., Jungner, H., 2001. An improvement in preparation of mortar for radiocarbon dating. *Radiocarbon* 43, 271-273.
- Soukup, D.A., Buck, B.J., Harris, W., 2008. Preparing soils for mineralogical analyses, In: Ulery, A.L., Drees, L.R. (Eds.), *Methods of Soil Analysis. Part 5—Mineralogical Methods*. Soil Science Society of America, Inc, Madison, pp. 12-31.
- Stuiver, M., Polach, H.A., 1977. Discussion of reporting ^{14}C data. *Radiocarbon* 19, 355.
- Stuiver, M., Smith, C.S., 1965. Radiocarbon dating of ancient mortar and plaster. *Proceedings of the 6th International ^{14}C Conference*, 338-343.
- Synal, H.A., 2013. Developments in accelerator mass spectrometry. *International Journal of Mass Spectrometry* 349-350, 192–202.
- Synal, H.A., M., S., Suter, M., 2007. MICADAS: A new compact radiocarbon AMS system. *Nuclear Instruments & Methods in Physics Research B* 259, 7–13.
- Van Strydonck, M., Dupas, M., Dauchotdehon, M., Pachiaudi, C., Marechal, J., 1986. The influence of contaminating (fossil) carbonate and the variations of delta-C-13 in mortar dating. *Radiocarbon* 28, 702-710.
- Van Strydonck, M.J.Y., Van der Borg, K., De Jong, A.F.M., Keppens, E., 1992. Radiocarbon dating of lime fractions and organic material from buildings. *Radiocarbon* 34, 873–879.
- Wilson, R., Spengler, J.D., 1996. *Particles in our air : concentrations and health effects*. Harvard University Press, Cambridge, Mass.
- Yang, W., Kim, Y., Liu, P.K.T., Sahimi, M., Tsotsis, T.T., 2002. A study by in situ techniques of the thermal evolution of the structure of a Mg-Al- CO_3 layered double hydroxide. *Chemical Engineering Science* 57, 2945–2953.

APPENDIX II

Characterization of Historical Lime Mortars Focused on Architectural Heritage Conservation

APPENDIX II.1

Mineralogical, Textural and Physical Characterisation to Determine Deterioration Susceptibility of Irulegi Castle Lime Mortars (Navarre, Spain)

Graciela Ponce-Antón, Anna Arizzi, Maria Cruz Zuluaga, Giuseppe Cultrone,
Luis Angel Ortega, Juantxo Agirre Mauleon

Materials 2019; 12(4):584

Article Metrics

✓ Journal Citation Reports

Citations: 3

Impact Factor

2018	5 Years
2.972	3.532

JCR® Rank	Classification	Quartile	Percentile
Materials Science Multidisciplinary	102 of 293	Q2	65.358

✓ Scopus

Citations: 2

CiteScore 2018	3.26
SJR 2018	0.686
SNIP 2018	1.200

CiteScore Rank	Classification	Percentile
Materials Science (General Materials Science)	97 of 438	77

✓ Google Academic

Citations: 3

Article

Mineralogical, Textural and Physical Characterisation to Determine Deterioration Susceptibility of Irulegi Castle Lime Mortars (Navarre, Spain)

Graciela Ponce-Antón ^{1,*} , Anna Arizzi ² , Maria Cruz Zuluaga ¹, Giuseppe Cultrone ² , Luis Angel Ortega ¹  and Juantxo Agirre Mauleon ³

¹ Department of Mineralogy and Petrology, Faculty of Science and Technology, University of the Basque Country-UPV/EHU, Sarriena s/n, 48940 Leioa, Bizkaia, Spain; mcruz.zuluaga@ehu.eus (M.C.Z.); luis.ortega@ehu.eus (L.A.O.)

² Department of Mineralogy and Petrology, Faculty of Sciences, University of Granada, Avda. Fuentenueva s/n, 18002 Granada, Spain; arizzina@ugr.es (A.A.); cultrone@ugr.es (G.C.)

³ Aranzadi Society of Sciences, Zorroagaina 11, 20014 Donostia-San Sebastián, Gipuzkoa, Spain; zuzendaritza@aranzadi.eus

* Correspondence: graciela.ponce@ehu.eus; Tel.: +34-946-015-456

Received: 29 January 2019; Accepted: 12 February 2019; Published: 15 February 2019



Abstract: Archaeological lime mortars from the Tower Keep and West perimeter wall of Irulegi Castle (Navarre, Spain) were analysed to determine susceptibility to deterioration. Chemical, mineralogical, textural and physical characterisation was performed by different tests and multianalysis techniques in order to determine the intrinsic features of the original historical mortars at the castle. Samples from the Tower Keep are more prone to deteriorate compared with the West perimeter wall due to high water absorption capacity and high porosity. A high degree of pore interconnection, high desorption index and the presence of high pore volume in the 0.01 to 1 μm size range affect the mortar durability since pores retain water longer inside the mortar. Local environment conditions with persistent annual rainfall, high humidity and temperature variations contribute to the decay process of the original mortar. Characterisation of historical mortars not only allows better understanding of susceptibility to deterioration but also helps the design of compatible and durable repair mortar for future interventions on historical heritage. Compatibility of new materials with the historical mortar will be ensured by studying mortar characteristics and properties.

Keywords: lime mortar; mineralogy; texture; durability; deterioration; hydric behaviour; pore system

1. Introduction

The preservation of built heritage requires suitable materials and techniques to enable effective restoration interventions [1]. The characterisation of original historical mortars is an important step before carrying out any repair interventions since the characteristics of the new mortar must be as similar as possible to those of the ancient mortar [2]. Differences in the material properties lead to a lack of compatibility between the new and original mortar reducing their durability [3]. Several authors have carried out chemical, mineralogical and physical analyses prior to the formulation of repair mortars [4–7]. Comparative studies using different limes and additives also have been carried out [8–10]. In addition, the material is exposed to different environmental conditions to determine how they affect the mortar properties and which factors are involved in their decay [11–15]. Studies of the repair material properties are performed in order to select the most suitable mortar mixture for restoration work [16].

Environmental factors condition material deterioration processes [11,17]. Water, in liquid or vapour form (e.g., as humidity), favours the irreversible phenomenon of decay, giving place to different physical, chemical and biological deterioration processes [18,19]. Chemical degradation of mortars takes place mainly due to hydrolysis, hydration or oxidation processes. Volume increase within the pores, by such processes as crystallization of water into ice or swelling of some clay minerals, leads to physical degradation of the material [20]. Furthermore, water can incorporate dissolved salts into the material that may crystallize after water evaporation, as well as gaseous species such as CO₂ that can dissolve the calcareous materials under specific conditions [21].

Durability of materials does not only depend on the environmental factors but also on their intrinsic mineralogical and textural features [22,23]. The pore system plays an important role in mortar durability since weathering processes often depend on the circulation of water inside the pores, accelerating the physical, chemical and biological deterioration [24]. Studies on hydric behaviour have been carried out to understand water deterioration mechanisms in building materials since the parameters associated with fluid uptake and transport inside the pores directly influence material deterioration [3,5]. Water circulation through the material is also conditioned by the presence of anisotropies and the interconnection degree between the pores [17,25].

Not only compatibility but also authenticity of the restoration material with the original mortar is one of the main goals in heritage conservation. Achieving aesthetic features in terms of visual appearance (e.g., texture and colour) is another important requirement in the restoration process [2,26]. Colour is a sensorial perception between the object, the lighting and the observer, so visual variations in colour between restored and original materials is an issue of interest in restoration [27,28]. In addition to chemical, mineralogical, physical and aesthetic characterisation, the workability is another important feature to consider in mortar formulation [26].

Irulegi Castle (Navarre, northern Spain) was built in a defensible site. Geographically the castle is located in a mid-latitude climate zone with a suboceanic west coastal maritime climate [29]. Regional climate is characterised by a moderately warm climate with cool summers and abundant rainfall well distributed throughout the year, although with two dry months.

The aim of this study is to assess the hydric behaviours of lime-based archaeological mortars from Irulegi Castle in order to establish their susceptibility to deterioration. Taking into account the climatic conditions to which historical mortars are exposed, knowledge of chemical, mineralogical and physical properties will allow the formulation of an adequate repair mortar to ensure the compatibility and authenticity of the restoration material with the original mortar.

2. Archaeological Background

The medieval archaeological site of Irulegi Castle is on the eastern border of the Pamplona Basin (Figure 1). It is a rock castle on Irulegi Mountain in the east of Aranguren mountain range (Navarre, Spain). The historical strategic emplacement of the castle allowed visual control of the Navarre kingdom capital and the routes to the pass over the Pyrenees along the Izagaondoa valley.

The walled archaeological site is characterised by a rectangular floor 39 m × 15 m in size with an area of approximately 460 m². Within the castle structures, mortars from the Tower Keep and the West perimeter wall were studied. The Tower Keep presents pseudoisodom bonding with high quality ashlars. The absence of compositional differences in the tower ashlars indicates that all the structure was built in the same construction period [30]. Nevertheless important renovations in the defensive elements of the castle were undertaken as a result of the constructive techniques developed over time. The remodelling of the Tower Keep resulted in the dismantling of the south outer wall and the original rectangular floor was transformed into the current polygonal floor with a vertex-shaped structure. This remodelling increased the floor area from 90 m² to 105 m². The west perimeter wall shows lower-quality irregular bonding and has average dimensions of 1.25 m width and 11.35 m length (Figure 2). A continuous settlement sequence from the Late Bronze Age to the Late Middle Ages has been recognised in the archaeological site. However, the earliest fortification building is

unknown since no documentary data about the first building period of the castle exist. The oldest mentions of Irulegi Castle are dated in the second half of the 12th century and beginning of the 13th century. The castle was demolished at the end of the 15th century and currently only ruins remain standing [30,31].



Figure 1. Geographic location of Irulegi Castle (Navarre, Spain).



Figure 2. Location of studied samples in the Tower Keep and West perimeter wall at Irulegi Castle.

3. Materials and Methods

3.1. Materials

Eight archaeological mortar samples, seven from the Tower Keep and one from the West perimeter wall at Irulegi Castle (Navarre, Spain) were collected and analysed (Table 1 and Figure 2). While the Tower Keep structure is still unconsolidated, the West perimeter wall was consolidated in 2017 but the sample corresponding to this wall was collected before the consolidation of the castle

ruins. Considering the studied mortars correspond to archaeological materials, sample selection was determined on the basis of the minimum volume required to perform the capillary tests.

Table 1. Studied samples from different structures at Irulegi Castle.

Archaeological Structure	Sample
West perimeter wall	CI-M-3
	CI-T-8
Tower Keep	CI-T-9
	CI-T-10
	CI-T-11
	CI-T-12
Tower Keep extension	CI-TE-8
	CI-TE-9

3.2. Methods

Different analytical techniques and tests were performed to determine the mineralogy, chemistry, texture and physical properties of the collected archaeological mortars.

3.2.1. Mineralogical, Chemical and Petrographic Characterisation

The mineralogical composition of samples was determined by means of X-ray diffraction (XRD) using a Philips X'Pert diffractometer (Leioa, Spain) equipped with a monochromatic Cu- $k_{\alpha 1}$ X-radiation operating at 40 kV and 20 mA. The data collection on the powder sample was performed by a continuous scan in the range from 5 to 70° 2 θ , at an acquisition rate of 0.02° per second. Mineral phase identifications were performed with X'Pert HighScore Plus 3.0 software by PANalytical (Leioa, Spain).

Chemical composition of major elements in bulk mortar was established by means of X-ray Fluorescence (XRF) in powder sample. Measurements were taken by Wavelength Dispersive X-ray Fluorescence (WDXRF) using a PANalytical Axios Advanced PW4400 XRF spectrometer (4 kW Rh anode SST-mAX X-ray tube, Leioa, Spain). Fused beads were obtained after heating a sample and lithium borate flux (Spectromelt A12, Merck, Leioa, Spain) mixture in approximate 20:1 proportions at ~1200 °C for 3 min in Pt/Au crucibles using a PANalytical Perl'X3 fusion machine. Detection lower limits for major elements are in the range of 0.01 wt %. The loss on ignition (LOI) has been calculated after heating a powder sample of bulk mortar at 1050 °C for one hour.

The mortar texture and nature of components were determined in polished thin sections using a Nikon Eclipse LV100POL microscope (Leioa, Spain) equipped with DS F-I1 digital camera and a DS L-2 control unit.

3.2.2. Characterisation of Pore System and Hydric Behaviour

Mercury intrusion porosimetry (MIP) was used to determine the pore size distribution and the open porosity (P_{MIP}) by a Poremaster-60 GT (Quantachrome Instruments, Alicante, Spain), with a maximum injection pressure of 414 MPa, measuring the pore diameter range from approximately 0.003 to 360 μm . Mortar sample fragments about 1 cm^3 were oven-dried for 24 h at 60 °C before the analysis.

To obtain a complete vision of the pore system, hydric tests (HT) were carried out in samples of 3 cm^3 in size; previously oven-dried at 80 °C for 24 h. Measurements were taken under controlled thermo-hygrometric conditions at 25 °C and 50% relative humidity. The test measurements were performed on no more than two or three samples per mortar type, since samples are archaeological materials.

The free (A_b) and forced (A_f , under vacuum) water absorption values and absorption coefficient (C_a) were determined following the UNE-EN 13755 [32] standard. The degree of interconnection

between the pores (A_x) [33] and the saturation coefficient (S) [34] were also determined. These hydric parameters were calculated as follows

$$A_b = \frac{M_L - M_0}{M_0} \cdot 100 \quad (1)$$

where M_0 is the mass of the dried sample and M_L is the mass of the sample saturated under water at atmospheric pressure (until constant mass is reached):

$$A_f = \frac{M_s - M_0}{M_0} \cdot 100 \quad (2)$$

$$A_x = \frac{A_f - A_b}{A_f} \cdot 100 \quad (3)$$

$$C_a = \frac{A_b}{\sqrt{t}} \quad (4)$$

where M_s is the mass of the sample saturated with water under vacuum. The absorption coefficient (C_a) is determined as the slope of the curve representing the weight increase as a function of the square root of time 4 min after the beginning of the test:

$$S = \frac{M_{48h} - M_0}{M_s - M_0} \cdot 100, \quad (5)$$

where M_{48h} is the mass of the sample after 48 h immersion in water at atmospheric pressure.

Drying index (D_i) is defined as the definite integral of the drying curve from the beginning (t_0) to the end (t_f) times of the test in which M_t represents a decreasing water weight content starting from the saturation values (under vacuum) as a function of time. The D_i was measured according to the NORMAL 29/88 [35]:

$$D_i = \frac{\int_{t_0}^{t_f} f(M_t) dt}{M_s \cdot t_f} \quad (6)$$

The capillarity coefficient (C_c) and the capillarity height (H_c) of samples were calculated according to the UNE-EN 1925 [36] standard:

$$C_c = \frac{M_t - M_0}{A \cdot \sqrt{t}}, \quad (7)$$

where M_t is the amount of water absorbed at time t and A is the surface of the sample in contact with the water:

$$H_c = \frac{h}{\sqrt{t}} \quad (8)$$

where h is the height of water rise by capillarity at time t .

Finally, UNE-EN 1936 [37] standard was used to determine the open porosity (P_{HT}) and skeletal (ρ_{Hsk}) and bulk (ρ_{Hb}) densities as follows

$$P_{HT} = \frac{M_s - M_0}{M_s - M_H} \cdot 100 \quad (9)$$

$$\rho_{Hsk} = \frac{M_0}{M_0 - M_H} \quad (10)$$

$$\rho_{Hb} = \frac{M_0}{M_s - M_H}, \quad (11)$$

where M_H is the mass of the sample saturated with water under vacuum and weighted in water.

3.2.3. Nondestructive Tests

In order to assess mortar compactness, ultrasonic wave propagation was measured using a Control ultrasonic pulse velocity tester model 58-E4800 with a couple of nonpolarised piezoelectric transducers of 54 MHz (Granada, Spain). A viscoelastic couplant gel was applied to ensure a good contact between the transducers and the sample (Transonic gel). The propagation velocity of ultrasonic pulses (V_p) was measured on samples of 3 cm³ in size (previously oven-dried at 80 °C for 24 h) according to the ASTM D 2845-05 [38] standard under controlled thermo-hygrometric conditions at 25 °C and relative humidity of 50%. V_p values were useful to determine the structural anisotropy (ΔM) [39] as follows:

$$\Delta M = \left(1 - \frac{2V_{pmin}}{V_{pmax} + V_{pmean}} \right) \cdot 100, \quad (12)$$

where V_{pmax} is the mean maximum velocity, V_{pmin} is the mean minimum velocity and V_{pmean} is the mean intermediate velocity in each of the three orthogonal directions.

The colour characterisation of samples was carried out by spectrophotometry according to the CIELab system following the UNE-EN 15886 [40] standard. The lightness (L^*) and chromatic (a^* and b^*) parameters were determined by means of a portable Konica-Minolta CM-700d spectrophotometer (8 mm diameter; D65 illuminant; 10° view angle; SCI/SCE mode; 400–700 nm light radiation range, Granada, Spain). Colour was measured in five points of each mortar sample and mean values were calculated.

4. Results and Discussion

4.1. Mineralogical, Chemical and Petrographic Studies

The mineralogy obtained by XRD shows calcite and quartz to be the most abundant mineral phases in all mortars, although in different relative amounts. Sample CI-T-9 displays the highest quartz content. Feldspars and phyllosilicates are present in all samples but in minor amounts. Only Samples CI-T-9 and CI-TE-9 contain iron oxides (hematite and goethite) corresponding to the rock fragments used as aggregates (Table 2).

Table 2. Results of mineralogical composition of bulk mortar determined by X-ray diffraction. Cal: calcite, Qtz: quartz, Fsp: feldspar s.l.; Phy: phyllosilicates s.l.; Fe ox: iron oxides. The amount was expressed as follows: ****: predominant compounds; ***: high proportion; **: medium proportion; *: low proportion; tr: trace; -: undetected.

Sample	Cal	Qtz	Phy	Fsp	Hem
CI-M-3	****	**	*	tr	-
CI-T-8	***	**	*	tr	-
CI-T-9	**	****	*	*	tr
CI-T-10	***	**	*	tr	-
CI-T-11	***	**	*	*	-
CI-T-12	***	**	*	tr	-
CI-TE-8	***	**	*	tr	-
CI-TE-9	***	**	*	*	*

Table 3 shows the quantitative chemical results of major elements determined by X-ray fluorescence. The chemical composition is in accordance with the identified mineral phases. High values of Si in all samples are related to such silicates as quartz, phyllosilicates and feldspars. In fact, sample CI-T-9 shows the highest SiO₂ value (~41 wt %) corresponding to a quartz-enriched sample. On the contrary sample CI-M-3 has the lowest SiO₂ value (~32 wt %). The high Ca content is mainly due to the presence of calcite, as well as the LOI value. CI-M-3 sample shows the highest CaO (~32 wt %) and LOI values (~29 wt %), indicating the major content of calcite in this sample. On the contrary, samples CI-T-9, CI-T-10 and CI-T-11 have the lowest Ca values (~26 wt %), indicating low

carbonate content. Samples CI-M-3, CI-T-9, CI-T-10 and CI-T-11 display the highest Al, K, Mg and Ti values related to the relatively high phyllosilicate contents. Iron content is related to the presence of iron oxides/hydroxides (i.e., hematite and goethite) and phyllosilicates and the highest values correspond to samples with high Al, K, Mg and Ti values (i.e., samples CI-M-3, CI-T-9, CI-T-10 and CI-T-11).

Textural and mineralogical differences of mortars imply variations in the hydric characteristics since the pore system could vary [41]. Macroscopically all samples show a heterogeneous texture both in aggregate size and nature (Figure 3a,b). Nevertheless, some samples contain aggregates that are bigger in size (Figure 3c) and in large amounts (Figure 3d) particularly in the case of Sample CI-T-9. Reused mortar fragments more than 1 cm in size (Figure 3e–g) and cracks can also be seen with the naked eye (Figure 3h). Within the heterogeneous texture of mortar samples, CI-M-3 has fewer aggregates in a more homogeneous texture compared with the other samples (Figure 3i). Porosity at the edge of larger aggregates can be observed (Figure 3c).

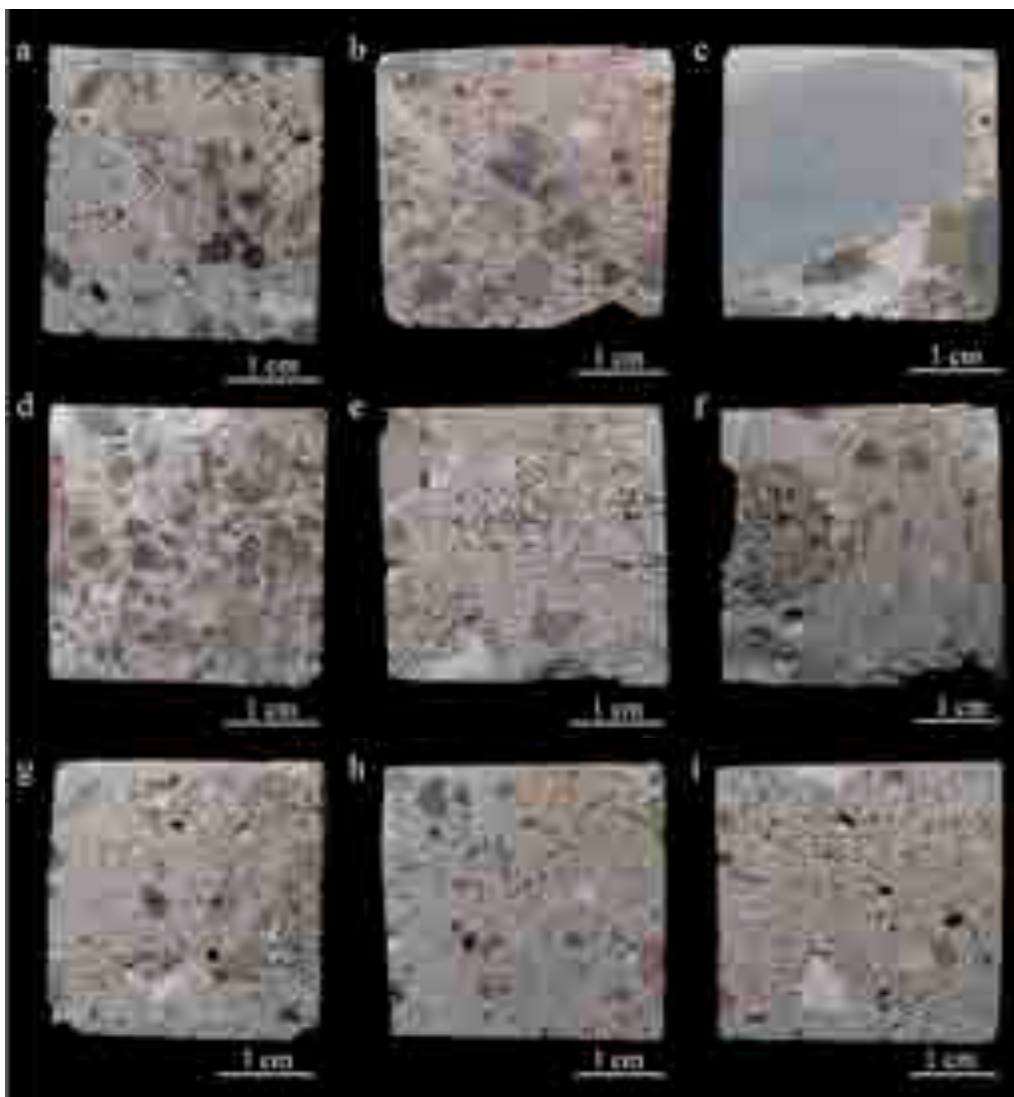


Figure 3. Images of archaeological mortar hand samples showing the heterogeneous texture. (a) Sample CI-T-8; (b) sample CI-T-10; (c) sample CI-T-9, mortar with a big size sandstone aggregate showing porosity at the grain edge; (d) sample CI-T-9, mortar with abundant presence of rock fragments; (e) sample CI-T-11, (f) Sample CI-T-12 and (g) sample CI-TE-9, mortars with reused mortar fragments; (h) sample CI-TE-8, cracked mortar; and (i) sample CI-M-3, showing the most homogeneous texture.

Table 3. Result of chemical composition of major elements of bulk mortar determined by X-ray fluorescence expressed as oxides in wt %. The iron content has been expressed as total Fe₂O_{3t}. LOI: loss on ignition (%).

	SiO ₂	Al ₂ O ₃	Fe ₂ O _{3t}	MnO	MgO	CaO	Na ₂ O	K ₂ O	TiO ₂	P ₂ O ₅	SO ₃	LOI
CI-M-3	31.95	3.27	1.82	0.06	0.63	31.69	0.08	0.56	0.28	0.06	0.11	28.86
CI-T-8	38.08	2.95	1.25	0.03	0.60	28.77	0.09	0.74	0.23	0.12	0.06	26.57
CI-T-9	40.60	3.26	1.34	0.03	0.69	26.90	0.07	0.76	0.25	0.13	0.07	24.40
CI-T-10	38.67	3.42	1.39	0.03	0.74	26.93	0.11	0.79	0.25	0.10	0.03	25.07
CI-T-11	36.07	3.42	1.52	0.03	0.70	26.49	0.08	0.76	0.25	0.27	0.07	26.39
CI-T-12	38.44	2.55	1.37	0.03	0.55	31.03	0.08	0.57	0.2	0.09	0.07	23.99
CI-TE-8	35.46	2.32	1.16	0.03	0.65	29.39	0.04	0.43	0.18	0.08	0.10	25.98
CI-TE-9	37.40	2.37	1.29	0.03	0.56	32.29	0.06	0.47	0.2	0.08	0.05	23.97

The petrographic study improves the observed macroscopic features. Microscopically all the samples also exhibit heterogeneous texture (Figure 4). The matrix is formed by micritic calcite. Aggregates consist of heterometric and angular to subangular detrital quartz, sandstone, marl and calcarenite rock fragments (Figure 4a,b). A great variety of bioclast fragments (echinoderm plates, foraminifers and molluscs) are present due to the crushing of the rocks used as aggregate (Figure 4c,d). The quartz grains range from 0.05 µm to 0.25 µm in size. The smaller rock fragments are subangular while the largest are rounded (Figure 4b,e). Some sandstone fragments contain iron oxides (Figure 4e). Rounded ceramic fragments < 1 mm in size and charcoal fragments can also be seen dispersed in the matrix (Figure 4e,f). In samples CI-T-11, CI-T-12 and CI-TE-9, reused mortar fragments of <2 cm in grain size have also been observed (Figure 4c). Heterometric quartz-bearing lime lumps can be observed within the binder matrix (Figure 4g). The pores in the matrix are irregularly shaped and <200 µm in size and some show recrystallizations of secondary calcite inside (Figure 4d). Porosity at the edge of some aggregates can also be observed microscopically (Figure 4c). Samples CI-T-11, CI-T-12, CI-TE-8 and CI-TE-9 display microcracks in the matrix (Figure 4h). Sample CI-M-3 is characterised by fewer sandstone fragments and a more homogeneous texture compared with the rest of the samples.

The petrographic characteristics confirm the mineralogical and chemical composition of mortars. Samples with a large number of sandstone fragments correspond to the samples with the highest silica content. The matrix-supported texture of samples and the presence of fossils and calcareous rock fragments explain the high Ca content and the calcite identified by XRF and XRD, respectively. Sample CI-M-3 shows the lowest siliceous aggregate content as well as the highest presence of calcite as reflected in the Ca and LOI content obtained by chemical analysis (Table 2). The iron contents are associated with hematite and goethite present in sandstones and with the phyllosilicates in the matrix. The iron phases were not detected by XRD in most samples since the content is under the detection limit of the analytical method.

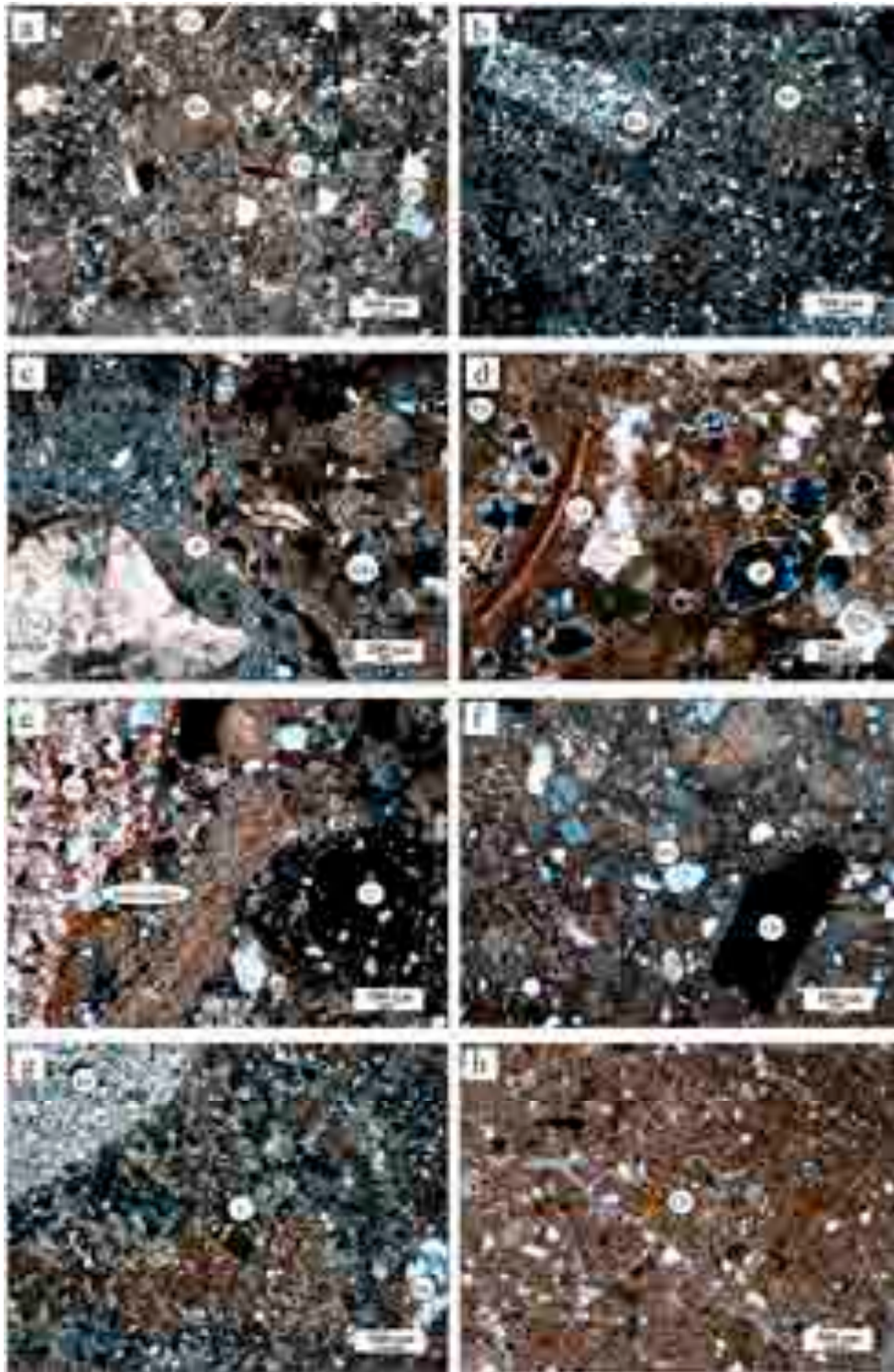


Figure 4. Photomicrographs show the most representative textural features of historic lime mortars from Irulegi Castle. (a) Mortar with quartz grains and rock and fossil fragments, (b) mortar with angular fragments of sandstone and (c) mortar with fossil (left) and reused mortar (right) fragments. Porosity between the mortar fragment and the matrix can be observed, (d) mortar with pores that show recrystallizations inside, (e) mortar with rounded ceramic fragment, (f) mortar with charcoal fragment, (g) mortar with quartz-bearing lumps and (h) mortar matrix with microcracks. C: ceramic, Ch: charcoal, Ck: crack, Fsl: fossil, L: lump, MFr: Mortar fragment, P: pore, Qtz: quartz, R: recrystallization, Rx: rock fragments.

4.2. Pore System and Hydric Behaviour

Mercury intrusion porosimetry (MIP) values are summarised in Table 4. Samples CI-T-10 and CI-TE-9 show the highest porosity values (50.27% and 42.76%, respectively). Samples CI-T-11 and CI-TE-8 have the lowest PMIP values (20.44% and 2.48%, respectively) due to the presence of coarse aggregate with low porosity, resulting in an anomalous MIP value. The small sample size required in the measurement could include coarse and low porous aggregates affecting the results.

Table 4. Parameters obtained by hydric tests (HT) and mercury intrusion porosimetry (MIP) of Irulegi Castle lime mortars. A_b : Free water absorption (%); A_f : forced water absorption (%); A_x : degree of pore interconnection (%); S : Saturation coefficient (%); C_a : absorption coefficient ($\text{g}/\text{min}^{0.5}$); D_i : drying index; P_{HT} and P_{MIP} : open porosity (%); ρ_{HB} : bulk density (g/cm^3); ρ_{Hsk} : skeletal density (g/cm^3); C_c : capillarity coefficient ($\text{g}/\text{cm}^2 \text{min}^{0.5}$); H_c : Height of the water level during capillary uptake ($\text{mm s}^{-0.5}$).

	CI-M-3	CI-T-8	CI-T-9	CI-T-10	CI-T-11	CI-T-12	CI-TE-8	CI-TE-9
A_b	18.80	26.35	36.63	33.83	20.08	20.94	33.61	28.86
A_f	19.90	27.87	37.45	35.57	21.29	22.50	35.11	30.04
A_x	5.54	5.43	2.20	4.91	5.68	6.95	4.28	3.92
S	89.17	92.00	93.68	90.17	91.08	90.11	93.11	94.26
C_a	9.40	13.18	18.31	16.91	10.04	10.47	16.81	14.43
D_i	0.264	0.266	0.261	0.262	0.270	0.269	0.262	0.267
ρ_{HB}	1.62	1.39	1.24	1.27	1.62	1.51	1.31	1.39
ρ_{Hsk}	2.39	2.26	2.33	2.31	2.47	2.28	2.41	2.38
C_c	0.010	0.013	0.009	0.021	0.011	0.018	0.021	0.008
H_c	0.42	0.52	0.52	0.77	0.65	0.65	0.65	0.52
P_{HT}	32.25	38.63	46.55	45.06	34.48	33.88	45.86	41.68
P_{MIP}	35.43	38.74	-	50.27	20.44	-	2.48	42.76

Another fundamental characteristic of the pore system is the pore size distribution since the pore size affects the water circulation in the material [42,43]. MIP results indicate a large volume of small pores ($0.01 < r < 1 \mu\text{m}$) connected to larger pores ($1 < r < 10 \mu\text{m}$) in all samples (Figure 5). In this type of network, larger pores empty first whereas smaller pores remain full of liquid and dry more slowly [44]; therefore, the presence of two main families of pores strongly influences the drying behaviour of the material. However, pore size distribution is not the same in all samples (Figure 5a). Samples CI-M-3 and CI-TE-9 possess a nearly unimodal size distribution ranging between $0.01 \mu\text{m}$ and $1 \mu\text{m}$ although a second smaller family of pores ranging between $1 \mu\text{m}$ and $10 \mu\text{m}$ can be observed (Figure 5b,c). Sample CI-T-8 has a bimodal distribution of large pores of between 0.1 and $1 \mu\text{m}$ and a second smaller family between $0.01 \mu\text{m}$ and $0.1 \mu\text{m}$ in size (Figure 5d). Samples CI-T-10 and CI-T-11 have a more heterogeneous pore size distribution but the Sample CI-T-10 possesses a large pore volume (Figure 5e,f).

To complete the study on the pore system, hydric tests were also carried out (Figure 6). Table 4 shows the results of the hydric behaviour of mortar samples and their porosity accessible to water and mercury. Although the open porosity values obtained from the hydric tests (P_{HT}) and by mercury intrusion porosimetry (P_{MIP}) are very similar, the MIP values are always slightly higher. These differences are due to the fact that different liquids are used (H_2O and Hg , respectively) and at different pressures (atmospheric pressure in the hydric tests and an injection pressure of 414 MPa in MIP analysis). Open porosity (P_{HT}) has a direct effect on the durability of mortars because it allows water circulation within the structure favouring the entry of aggressive agents contained in the water. Therefore, the accessible porosity values are an important parameter to evaluate the possible deterioration of materials [45]. Samples CI-T-9, CI-T-10, CI-TE-8 and CI-TE-9 present the highest open porosity values ($P_{HT} > 40\%$) while CI-M-3 shows the lowest values (35.43%).

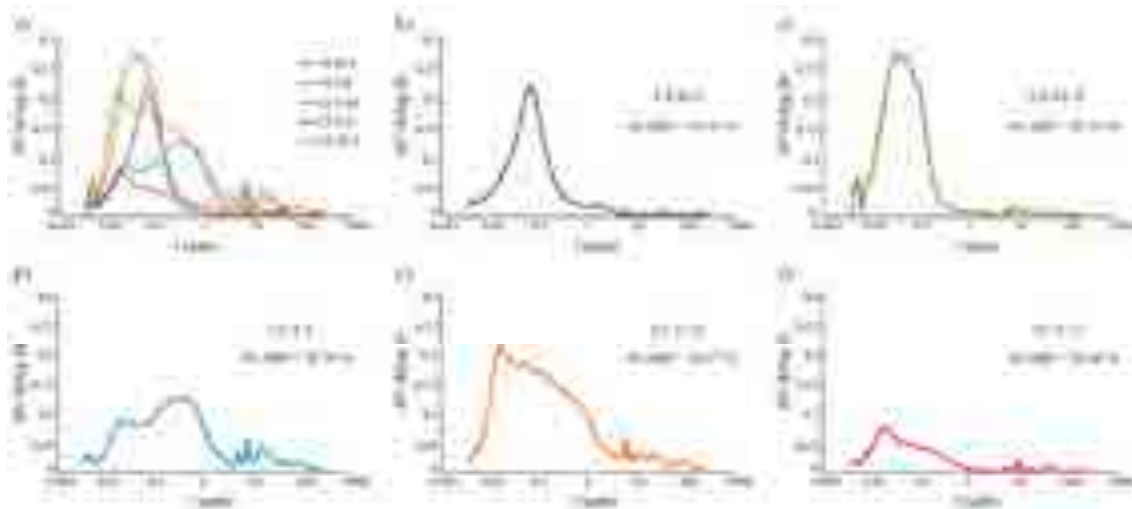


Figure 5. Mercury intrusion porosimetry pore size distribution curves for Irulegi Castle lime mortars: (a) all samples, (b) CI-M-3, (c) CI-TE-9, (d) CI-T-8, (e) CI-T-10, (f) CI-T-11. Pore radius (in μm) is represented versus incremental pore volume (in cm^3/g).

Samples CI-T-9, CI-T-10, CI-TE-8 and CI-TE-9 display the highest free water absorption (A_b , $>28\%$) and forced water absorption (A_f , $>30\%$) levels whereas sample CI-M-3 shows the lowest values ($A_b = 18.80\%$ and $A_f = 19.90\%$). Samples CI-T-8, CI-T-11 and CI-T-12 have intermediate water absorption and forced water absorption values (Table 4, Figure 6a). The lowest degree of pore interconnection values (A_x) are in samples CI-T-10, CI-TE-8 and CI-TE-9 and, above all, in CI-T-9, indicating that water flows more easily inside mortars due to a better interconnection between the pores. On the contrary, CI-T-12 has the highest A_x values (almost 7%) indicating a more tortuous pore system hindering the flow of water inside the mortar (Table 4). The saturation coefficient (S) is directly related to the interconnectivity of the pores. In fact, the higher values are in samples CI-T-9, CI-TE-8 and CI-TE-9 ($>93\%$). The absorption coefficient (C_a) values are the highest ($>15 \text{ g}/\text{min}^{0.5}$) in samples CI-T-9, CI-T-10 and CI-TE-8. This value together with the degree of interconnection affects the water content capacity.

During the drying, two different drying phases occur. In the first drying phase, the evaporation of water from the wet surface is constant (constant rate drying) and the porosity has no significant influence on the drying rate [44,46]. In the second phase, drying depends on the pore radii and the degree of interconnection. When drying goes from constant velocity to a decreasing velocity the critical moisture content is reached and the drying rate changes. Then the water loss depends on the movement of water towards the surface through the capillary pores (falling rate period) [44,47]. Drying velocity is given by the desorption index (D_i). Samples CI-T-9, CI-T-10 and CI-TE-8 present lower D_i values indicating fast drying, while CI-T-11, CI-T-12 and CI-TE-9 present with higher values took longer to dry (Table 4). Samples showing lower D_i values correspond to samples with lower degree of pore interconnection (A_x) indicating that water flows easily outwards. On the contrary samples with high D_i and A_x values dry more slowly, indicating that water is retained longer in the mortar pore system, thus affecting its durability.

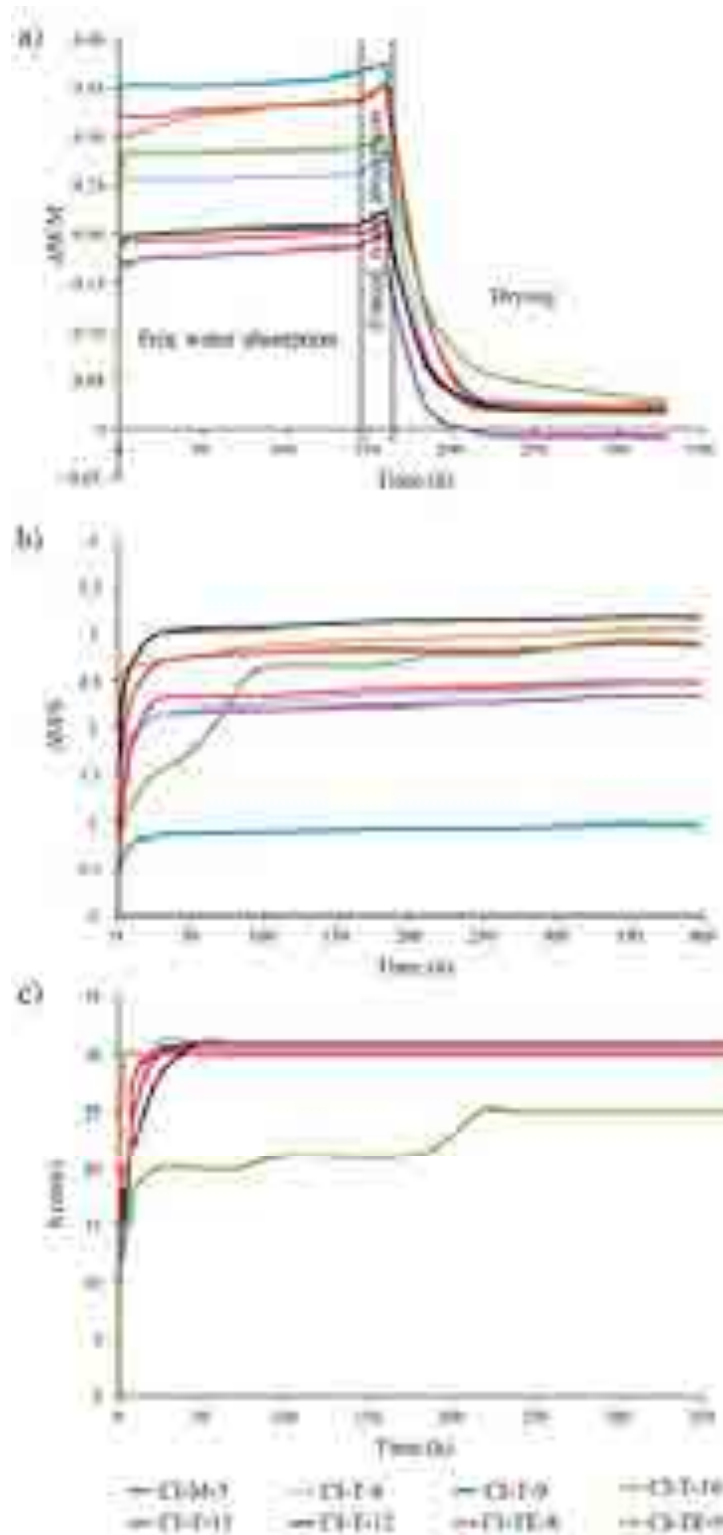


Figure 6. Hydric behaviours of Irulegi Castle lime mortars. (a) Free water absorption, forced water absorption and drying curves. Weight variation ($\Delta M/M$) versus time (in hours). (b) Capillary uptake curves: Weight variation ($\Delta M/S$) versus time (in hours) and (c) capillarity front curves. Height (in mm) versus time (in hours).

Regarding capillary uptake curves, samples absorb water quickly at the beginning of the test and as samples become saturated in water the velocity of capillary rise decreases and stabilizes reaching an equilibrium value (Figure 6b), following the most common capillary rise trend found for lime

mortars [5]. The nonlinear curves showing two sections with different slopes are due to the presence of two main families of pores in the mortars [48] as MIP analysis revealed ($0.01 \mu\text{m} < r < 1 \mu\text{m}$ and $1 \mu\text{m} < r < 10 \mu\text{m}$). Samples CI-T-10 and CI-TE-8 have high capillarity coefficient (C_C) values because they absorb water faster than samples CI-M-3 and CI-TE-9, which indeed show lower C_C values (Table 4). The capillary front reached the top of all samples after 48 h except in Sample CI-TE-9 where water did not reach the top until 216 h (nine days) after the beginning of the test (Figure 6c). However, this visual saturation does not coincide in time with the real saturation that occurs after 400 h (~16 days) (Figure 6b,c). This delay confirms the presence of two families of pores, which are filled at different velocities by water (smaller pores are filled first). Saturation is achieved when all connected pores are filled.

Samples CI-M-3 and CI-T-11 show the highest values of both bulk (ρ_{Hb}) and skeletal (ρ_{Hsk}) density (Table 4). Differences between skeletal and bulk densities are related to the porosity of mortars. This difference is greater in the more porous samples (CI-T-9, CI-T-10, CI-TE-8 and CI-TE-9).

4.3. Nondestructive Tests

Table 5 summarizes the ultrasound measurements in mortar samples. Considering lime mortar as an ideal two-phase media of aggregate embedded in a calcitic matrix, V_p values depend on the wave velocity both in the matrix and the aggregates, since ultrasonic wave propagation is different in each phase. The V_p decreases considerably when the wave propagates from an aggregate to the matrix [49]. No relationship between the V_p and aggregate size has not been found probably because aggregates act as a homogeneous structure considering size a constant parameter [50]. However, aggregate mineralogy is important in ultrasonic wave propagation velocity [51]. In fact, waves propagate more quickly through calcite (approximately 6660 m/s) than through quartz (approximately 5800 m/s) [52]. Therefore, P-wave velocity is directly related to the petrographic characteristic of the mortar. V_p values decrease in all mortar samples due to the presence of a large amount of siliceous aggregates, except in Sample CI-M-3, which contains the lowest amount of aggregates. Porosity also affects the ultrasonic wave propagation velocity since when the wave propagates from a solid (aggregates or matrix) through a gaseous medium (pores) the ultrasonic wave propagation velocity decreases [15]. Ultrasound data, indeed, are in agreement with the above-mentioned porosity results (Tables 4 and 5). The presence of small cracks also affects V_p , causing a fall in velocity [53], as in samples CI-T-11, CI-T-12, CI-TE-8 and CI-TE-9.

Table 5. Results of ultrasonic wave propagation through lime mortars from Irulegi Castle. V_{P1} , V_{P2} and V_{P3} (in m/s): P-wave velocity in three orthogonal directions; ΔM_p : total anisotropy coefficient of P-waves.

	CI-M-3	CI-T-8	CI-T-9	CI-T-10	CI-T-11	CI-T-12	CI-TE-8	CI-TE-9
V_{P1}	1815.48	186.75	178.77	130.80	158.19	150.49	178.77	151.83
V_{P2}	1828.91	197.60	340.66	134.20	159.79	169.49	191.62	183.43
V_{P3}	1820.90	197.60	358.70	132.78	197.37	157.36	203.82	177.51
ΔM	0.52	5.49	48.88	2.01	11.43	7.92	9.58	15.87

The total anisotropy coefficient of P-waves (ΔM_p) confirms the textural homogeneity of CI-M-3 sample and the textural heterogeneity of the rest of the samples. Sample CI-M-3 gave the lowest ΔM_p value and sample CI-T-9 the highest (Table 5).

The chromatic parameters of each mortar are summarised in Table 6. Colorimetric analyses showed that the lightness value (L^*) was lower for samples CI-M-3, CI-T-9, CI-T-10 and CI-T-11, while samples CI-T-12, CI-TE-8 and CI-TE-9 show the higher L^* values. The chromatic axes (a^* and b^*) values tend towards the light grey field due to a luminosity value close to 80. The a^* values are very similar in all samples except for Sample CI-M-3 which presents the highest values. Samples CI-T-12

and CI-TE-9 have the lowest b^* values. Lower L^* is due to the presence of aggregates, phyllosilicate phases and iron oxides, as petrographic and XRD analyses indicate.

Table 6. Chromatic parameters of mortar samples. Lightness (L^*), chromatic coordinates (a^* and b^*), chroma (C^*), hue angle (H).

	CI-M-3	CI-T-8	CI-T-9	CI-T-10	CI-T-11	CI-T-12	CI-TE-8	CI-TE-9
L^*	72.31	78.31	76.76	73.69	73.41	80.79	80.55	80.24
a^*	3.22	2.36	2.35	2.95	2.38	2.15	2.81	2.04
b^*	13.79	11.83	11.26	14.67	12.8	9.63	12.86	9.76
C^*	14.16	12.07	11.51	14.96	13.02	9.86	13.17	9.97
H	76.85	78.71	78.06	78.63	79.46	77.45	77.82	78.22

According to the measured parameters, samples CI-T-9, CI-T-10, CI-TE-8 and CI-TE-9 (South-Southeast face of the Tower Keep) present the highest free water absorption values ($A_b > 25\%$), high porosity values (P_{HT} and $P_{MIP} > 40\%$) with good pore interconnection (lowest A_x values), favouring the incorporation of dissolved salts and gaseous species such as CO_2 into the material that could deteriorate the mortar. Samples CI-T-11 and CI-T-12 (Southwest wall of the Tower Keep) display the worst pore interconnection (higher A_x values) and dry more slowly (higher D_i values), indicating a longer water retention also affecting mortar durability. Only sample CI-M-3 from the West perimeter wall shows less potential of deterioration due to the low free water absorption values ($A_b < 19\%$), fast drying and lower porosity (P_{HT} and $P_{MIP} \sim 32\%$).

Additionally, environmental factors condition mortar durability due to the presence of water both as humidity (water vapour) and as rainfall (liquid water). The climatic conditions at Irulegi Castle favour mortar deterioration since the average annual precipitation is around 858 mm and in 10 months rainfall is above 50 mm. The annual average humidity is $\sim 76\%$ but in summer periods the humidity is higher than the average values. Moreover, the average temperature is $11.8\text{ }^\circ\text{C}$ but the absolute average minimum and maximum temperatures are $-12.4\text{ }^\circ\text{C}$ and $39.9\text{ }^\circ\text{C}$, respectively [54]. The wide variation between absolute maximum and minimum temperature together with the high humidity favour the physical weathering of mortars. Material exposure to temperature variations leads to thermal expansion and temperatures below freezing result in frost wedging causing cracking of mortars. Additionally, the persistent rainfall favours dissolved salts and CO_2 incorporation into the mortars producing crystal growth and carbonate species dissolution, respectively.

5. Conclusions and Perspectives

The mineralogical, chemical and physical properties of eight archaeological lime mortar samples from Irulegi Castle were determined to enable an understanding of their susceptibility to deterioration.

High pore volume in the 0.01 to $1\text{ }\mu\text{m}$ size range is one of the reasons for the durability problems that the studied mortars might suffer in the future, since smaller pores retain water longer and dry more slowly. Related with their pore system, samples from the Tower Keep show high susceptibility to deterioration compared with the West perimeter wall sample. Samples from the south-southeast face of the Tower Keep show higher water absorption capacity and porosity (with good pore interconnection), while samples from the Southwest wall present the worst pore interconnection and dry more slowly.

Not only do the intrinsic features of the original mortars of Irulegi Castle, but also the local environmental exposure conditions, affect mortar deterioration. The persistent rainfall during the year, high humidity and temperature variations in this area certainly contribute to weathering processes in the original mortars. To design durable and compatible repair material for this castle, original mortar characteristics and environmental conditions should be taken into account.

Considering that the studied mortars are archaeological medieval mortars, differences in the physical properties among nearby samples would not necessarily indicate different mortar

manufacturing processes but could instead correspond to the typical heterogeneity of this type of material.

This study was able to determine the chemical-mineralogical characteristics and physical properties of the original historical mortars at Irulegi Castle, with positive implications for the design of compatible and durable repair mortar in future interventions. It will be essential to select the most appropriate mortar composition to ensure a satisfactory and long-lasting repair intervention. Compatibility, durability, authenticity and reversibility of the repair materials are indeed crucial requirements in any restoration work to be carried out in the future in this castle.

In the future, additional decay tests, including salt crystallization, wet and dry cycles, rainfall exposure and freeze-thaw cycles, should be carried out to assess the deterioration processes due to environmental agents in the area.

Author Contributions: Conceptualization, G.P.-A., A.A., G.C., M.C.Z. and L.A.O.; Data Curation, G.P.-A.; Writing—Original Draft Preparation, G.P.-A.; Writing—Review & Editing, G.P.-A., M.C.Z., A.A. and G.C.; Funding Acquisition, A.A., G.C., L.A.O. and J.A.M. All authors read and approved the final manuscript.

Funding: This study was possible thanks to the financial support of Junta de Andalucía Research Group RNM179 and Research Project MAT2016-75889-R.

Acknowledgments: G.P.-A. acknowledges the PhD research grant of the Basque Government [2015-1-02-35]. The authors would like to thank Peter Smith for reviewing the use of English in the manuscript.

Conflicts of Interest: The authors declare no conflicts of interest.

References

1. ICOMOS Declaration of Amsterdam-1975. Available online: <https://www.icomos.org/en/and/169-the-declaration-of-amsterdam> (accessed on 14 February 2019).
2. Schueremans, L.; Cizer, Ö.; Janssens, E.; Serré, G.; Balen, K.V. Characterization of repair mortars for the assessment of their compatibility in restoration projects: Research and practice. *Constr. Build. Mater.* **2011**, *25*, 4338–4350. [[CrossRef](#)]
3. Groot, C.; Ashall, G.J.; Hughes, J.J.; Bartos, P.J. Characterisation of old mortars with respect to their repair: A state of the art. *Rilem Rep.* **2007**, *28*, 1.
4. Hughes, J.J.; Cuthbert, S.J. The petrography and microstructure of medieval lime mortars from the west of Scotland: Implications for the formulation of repair and replacement mortars. *Mater. Struct.* **2000**, *33*, 594–600. [[CrossRef](#)]
5. Arizzi, A.; Cultrone, G. The water transfer properties and drying shrinkage of aerial lime-based mortars: An assessment of their quality as repair rendering materials. *Environ. Earth Sci.* **2014**, *71*, 1699–1710. [[CrossRef](#)]
6. Morillas, H.; Vazquez, P.; Maguregui, M.; Marcaida, I.; Silva, L.F.O. Composition and porosity study of original and restoration materials included in a coastal historical construction. *Constr. Build. Mater.* **2018**, *178*, 384–392. [[CrossRef](#)]
7. Nogueira, R.; Ferreira Pinto, A.P.; Gomes, A. Design and behavior of traditional lime-based plasters and renders. Review and critical appraisal of strengths and weaknesses. *Cem. Concr. Compos.* **2018**, *89*, 192–204. [[CrossRef](#)]
8. Arizzi, A.; Cultrone, G. The difference in behaviour between calcitic and dolomitic lime mortars set under dry conditions: The relationship between textural and physical–mechanical properties. *Cem. Concr. Res.* **2012**, *42*, 818–826. [[CrossRef](#)]
9. Arizzi, A.; Cultrone, G. Aerial lime-based mortars blended with a pozzolanic additive and different admixtures: A mineralogical, textural and physical-mechanical study. *Constr. Build. Mater.* **2012**, *31*, 135–143. [[CrossRef](#)]
10. Silva, B.A.; Ferreira Pinto, A.P.; Gomes, A. Natural hydraulic lime versus cement for blended lime mortars for restoration works. *Constr. Build. Mater.* **2015**, *94*, 346–360. [[CrossRef](#)]
11. Charola, A.; Kwiatkowski, D.; Löfvendahl, R. Stone deterioration in historic buildings and monuments. In Proceedings of the 10th International Congress on Deterioration and Conservation of Stone, Stockholm, Sweden, 27 June–2 July 2004.

12. Cultrone, G.; Sebastian, E. Laboratory simulation showing the influence of salt efflorescence on the weathering of composite building materials. *Environ. Geol.* **2008**, *56*, 729–740. [CrossRef]
13. Izaguirre, A.; Lanas, J.; Álvarez, J.I. Ageing of lime mortars with admixtures: Durability and strength assessment. *Cem. Concr. Res.* **2010**, *40*, 1081–1095. [CrossRef]
14. Arizzi, A.; Viles, H.; Cultrone, G. Experimental testing of the durability of lime-based mortars used for rendering historic buildings. *Constr. Build. Mater.* **2012**, *28*, 807–818. [CrossRef]
15. Arizzi, A.; Hueriga, G.M.; Sebastián, E.; Cultrone, G. Mineralogical, textural and physical-mechanical study of hydraulic lime mortars cured under different moisture conditions. *Mater. Construcc.* **2015**. [CrossRef]
16. Lanas, J.; Alvarez-Galindo, J.I. Masonry repair lime-based mortars: factors affecting the mechanical behavior. *Cem. Concr. Res.* **2003**, *33*, 1867–1876. [CrossRef]
17. Charola, A.E.; Lanzzarini, L. Material Degradation Caused by Acid Rain. In *ACS Symposium*; Baboian, R., Ed.; American Chemical Society: Washington, DC, USA, 1986; pp. 250–258.
18. Kühnel, R.A. Driving forces of rock degradation. In *Protection and Conservation of the Cultural Heritage of the Mediterranean Cities*; Galan, E., Zezza, F., Eds.; Swets & Zeitlinger: Lisse, The Netherlands, 2002; pp. 11–17.
19. Veniale, F.; Setti, M.; Lodola, S. Diagnosing stone decay in built heritage. Facts and perspectives. *Mater. Construcc.* **2008**, *58*, 11–32. [CrossRef]
20. Esbert, R.; Montoro, M.; Ordaz, J. Rock as a construction material durability deterioration and conservation. *Mater. Construcc.* **1991**, *41*, 61–73. [CrossRef]
21. Winkler, E.M. Weathering and weathering rates of natural stone. *Environ. Geol. Water Sci.* **1987**, *9*, 85–92. [CrossRef]
22. Ordóñez, S.; Fort, R.; Del Cura, M.G. Pore size distribution and the durability of a porous limestone. *Q. J. Eng. Geol. Hydrogeol.* **1997**, *30*, 221–230. [CrossRef]
23. Török, Á.; Vársárhelyi, B. The influence of fabric and water content on selected rock mechanical parameters of travertine, examples from Hungary. *Eng. Geol.* **2010**, *115*, 237–245. [CrossRef]
24. Molina, E.; Cultrone, G.; Sebastián, E.; Alonso, F.J.; Carrizo, L.; Gisbert, J.; Buj, O. The pore system of sedimentary rocks as a key factor in the durability of building materials. *Eng. Geol.* **2011**, *118*, 110–121. [CrossRef]
25. Hall, C.; Hoff, W.D. *Water Transport in Brick, Stone and Concrete*; Taylor & Francis: London, UK, 2002.
26. Van Balen, K.; Hendrickx, R. Preservation of workmanship or workmanship for preservation. In *Proceedings of the 6th International Conference on Structural Analysis of Historical Constructions: Preserving Safety and Significance*, Bath, UK, 2–4 July 2008; pp. 3–12.
27. Lozano, R.D. *El Color y su Medición: Con Una Introducción a la Óptica Fisiológica y al Estudio de la Visión*; Américalee S.R.L.: Buenos Aires, Argentina, 1978.
28. López, A.; Guzmán, G.A.; Di Sarli, A.R. Color stability in mortars and concretes. Part 1: Study on architectural mortars. *Constr. Build. Mater.* **2016**, *120*, 617–622. [CrossRef]
29. Peel, M.C.; Finlayson, B.L.; McMahon, T.A. Updated world map of the Köppen-Geiger climate classification. *Hydrol. Earth Syst. Sci.* **2007**, *11*, 1633–1644. [CrossRef]
30. Buces Cabello, J.; Moraza Barea, A.; Agirre Mauleon, J.; Pescador Medrano, A.; Legorburu Arzamendi, M. Un enclave estratégico en la Cuenca de Pamplona: el castillo medieval de Irulegi (Lakidain, Navarra). Balance de los trabajos arqueológicos (2007–2012). Available online: http://www.aranzadi.eus/wp-content/files_mf/1390899077Irulegi.pdf (accessed on 14 February 2019).
31. Martinena Ruiz, J.J. *Navarra Castillos y Palacios*; Caja de Ahorros de Navarra: Pamplona, Spain, 1980.
32. UNE-EN 13755, *Natural Stone Test Methods Determination of Water Absorption at Atmospheric Pressure*; AENOR: Madrid, Spain, 2008.
33. Cultrone, G.; De La Torre, M.J.; Sebastián, E.; Cazalla, O. Evaluation of bricks durability using destructive and nondestructive methods (DT and NDT). *Mater. Construcc.* **2003**, *53*, 41–59. [CrossRef]
34. RILEM. Recommended test to measure the deterioration of stone and to assess the differences of treatment methods. *Mater. Struct.* **1980**, *13*, 175–253. [CrossRef]
35. *NORMAL 29/88, Misura Dell'indice di Asciugamento (Drying Index)*; CNR-ICR: Rome, Italy, 1988.
36. UNE-EN 1925, *Natural Stone Test Methods. Determination of Water Absorptioncoefficient by Capillarity*; AENOR: Madrid, Spain, 2000.
37. UNE-EN 1936, *Natural Stone Test Methods. Determination of Real Density and Apparent Density, and of Total and Open Porosity*; AENOR: Madrid, Spain, 2007.

38. ASTM D 2845-05, *Standard Method for Laboratory Determination of Pulse Velocities and Ultrasonic Elastic Constants of Rock*; ASTM International Standards Worldwide: West Conshohocken, PA, USA, 2005.
39. Guyader, J.; Denis, A. Wave propagation in anisotropic rocks under stress evaluation of the quality of slates. *Bull. Int. Assoc. Eng. Geol.* **1986**, *33*, 49–55. [[CrossRef](#)]
40. UNE-EN 15886, *Conservation of Cultural Property. Test Methods. Colour Measurement of Surfaces*; AENOR: Madrid, Spain, 2011.
41. Valdeón, L.; Eibert, R.M.; Grossi, C.M. Hydric properties of some Spanish building stones: a petrophysical interpretation. *Mater. Issues Art Archaeol.* **1993**, *3*, 911–916. [[CrossRef](#)]
42. Alejandro Sánchez, F.J. *Historia, Caracterización y Restauración de Morteros*; Universidad de Sevilla: Sevilla, Spain, 2002.
43. Benavente, D. Why pore size is important in the deterioration of porous stones used in the built heritage. *Macla* **2011**, *15*, 41–42.
44. Scherer, G.W. Theory of Drying. *J. Am. Ceram. Soc.* **1990**, *73*, 3–14. [[CrossRef](#)]
45. Rodríguez-Navarro, C. Técnicas de análisis del sistema poroso de un material pétreo ornamental. In *Cuadernos Técnicos "Técnicas de Diagnóstico Aplicadas a la Conservación de los Materiales de Construcción en los Edificios Históricos"*; Instituto Andaluz del Patrimonio Histórico: Sevilla, Spain, 1996; Volume 2, pp. 51–65.
46. Cultrone, G.; Madkour, F. Evaluation of the effectiveness of treatment products in improving the quality of ceramics used in new and historical buildings. *J. Cult. Herit.* **2013**, *14*, 304–310. [[CrossRef](#)]
47. Kirk, R.E.; Othmer, D.F. *Encyclopedia of Chemical Technology*; Wiley: New York, NY, USA, 2004.
48. Beck, K.; Al-Mukhtar, M.; Rozenbaum, O.; Rautureau, M. Characterization, water transfer properties and deterioration in tuffeau: building material in the Loire valley-France. *Build. Environ.* **2003**, *38*, 1151–1162. [[CrossRef](#)]
49. Arizzi, A.; Martínez-Martínez, J.; Cultrone, G. Ultrasonic wave propagation through lime mortars: An alternative and non-destructive tool for textural characterization. *Mater. Struct.* **2013**, *46*, 1321–1335. [[CrossRef](#)]
50. Philippidis, T.P.; Aggelis, D.G. Experimental study of wave dispersion and attenuation in concrete. *Ultrasonics* **2005**, *43*, 584–595. [[CrossRef](#)] [[PubMed](#)]
51. Schön, J.H. *Physical Properties of Rocks: Fundamentals and Principles of Petrophysics*; Pergamon: Oxford, UK, 1996.
52. Carmichael, R.S. *Practical Handbook of Physical Properties of Rocks and Minerals*; CRC press: Boca Raton, FL, USA, 1989.
53. Molina, E.; Benavente, D.; Sebastian, E.; Cultrone, G. The influence of rock fabric in the durability of two sandstones used in the Andalusian Architectural Heritage (Montoro and Ronda, Spain). *Eng. Geol.* **2015**, *197*, 67–81. [[CrossRef](#)]
54. Beortegi GN. Available online: <http://meteo.navarra.es/climatologia/selfichaclima.cfm?IDEstacion=12&tipo=AUTO> (accessed on 17 January 2019).



© 2019 by the authors. Licensee MDPI, Basel, Switzerland. This article is an open access article distributed under the terms and conditions of the Creative Commons Attribution (CC BY) license (<http://creativecommons.org/licenses/by/4.0/>).

APPENDIX II.2

Lime mortars from Amaiur Castle (Navarre, Spain): mineralogical and physical characterization to assess their durability

Graciela Ponce-Antón, Anna Arizzi, Maria Cruz Zuluaga, Giuseppe Cultrone,
Luis Angel Ortega, Juantxo Agirre Mauleon

Submitted to Construction and Building Materials

Lime mortars from Amaïur Castle (Navarre, Spain): mineralogical and physical characterization to assess their durability

Abstract: Mineralogical, chemical and physical characterizations were performed on the archaeological lime mortars from different structures at Amaïur Castle (Navarre, Spain) in order to determine their durability. Samples from the south-east of the filling mortar and 16th century bastion and the samples from the south-east of the 17th century bastion may decay more easily. The high porosity and water absorption capacity, the poor interconnection of pores and the difficulty for drying are the main factors involved in their deterioration. A south-east sample from the 16th century bastion was also susceptible to deterioration and could be related to the repairs performed during the 16th century as described in written sources. Water absorption capacity of mortars from the cistern could affect the preservation of the remains of the cistern vault. Mineralogical characterization allowed an approach to the technological knowledge used in the mortar manufacturing process at Amaïur Castle. Hydrotalcite and hydromagnesite identified in the mortar binder support the use of the traditional hot-mixing method in the mortar manufacture. The hot-mixing method would be advantageous in the damp and cold climate conditions prevailing in the region where Amaïur Castle is located.

Keywords: lime mortar; deterioration; hydric behaviour; hydromagnesite; hydrotalcite; hot-mixed mortar

1. Introduction

Knowledge of the composition and behaviour of historical mortars has improved since the first studies at the end of the 19th century [1]. Chemical and mineralogical characterizations of these materials have been increasing since the approval of the Venice Charter in 1964 [2] and the foundation of the International Council on Monuments and Sites (ICOMOS) in 1975.

Mineralogical, chemical and physical characterization of historical mortars is essential to assess compatibility between the original and repair mortars in restoration projects [3, 4] and thus ensure architectural heritage conservation [5].

Knowledge of the hydric behaviour of porous materials such as mortars is essential to assess their durability over time. Water is one of the most harmful agents and its flow through a porous system plays an important role in building material deterioration [6, 7]. Furthermore, the climate conditions not only influence the mortar hardening process but also conditioned the water presence in the mortar affecting the mortar durability [8, 9].

Mineralogical, chemical and physical characterization and hydric behaviour studies have been performed to evaluate the durability of historical mortars and/or to ensure the quality of repair mortars used in the historical buildings [10-14].

Previous studies point to the use of the traditional hot-mixing method in the mortar manufacture at Amaïur Castle (Navarre Spain) [15]. The combination of chemical-mineralogical analyses and physical properties in the study of historical mortars are useful to investigate the traditional hot-mixing method and the different building phases of different periods at the castle.

The present study aims to characterize mineralogical, chemical and physical features of historical lime mortars from Amaïur Castle to assess their durability. The study of the pore

system and hydric behaviour of mortars will allow an assessment of their susceptibility to deterioration under the environmental conditions to which the materials are exposed. Results obtained by these studies could lead to significant implications to formulate compatible repair mortars.

2. Archaeological Background

Amaiur Castle is located in the north of the Baztan valley (Navarre, Spain) in a strategic emplacement during the Middle Ages since it allowed a visual control of the pass across the Pyrenees (Fig. 1). Archaeological work carried out in Amaiur Castle revealed an occupation period from the 13th century to the 17th century, but the first written sources mentioned the castle in the 12th century. Due to artillery development from the 14th century, the Amaiur Castle defences were largely remodelled during the 16th and 17th centuries. In the 16th century, the castle was reinforced giving rise to a circular bastion. New rounded structures were added and the medieval walls were thickened by filling the space between the 13th-14th and the 14th-15th century walls with lime mortar. In the 17th century, diamond-shaped structures were added that transformed the fortification into a *trace italienne* bastion [16, 17].



Fig. 1. Geographic location of Amaiur Castle (Navarre, Spain) and the plan of the castle with the sample locations marked by red circles. Modification from Ponce-Antón et al. (2020).

3. Materials and Methods

3.1. Materials

Fourteen lime mortars from different structures at Amaiur Castle were studied. Mortars were taken from the 14th-15th century wall, from the cistern and the rounded shape structures of the 16th century bastion, from the diamond-shaped structures of the 17th century bastion and from the fill between the 13th-14th and 14th-15th century walls (Fig.1 and Table 1).

Table 1. Studied mortar samples taken from the different structures at Amaiur Castle. * Lunette; **Barrel vault base; # Structure foundation. In green the samples located in the SE of the Castle.

Chronology	14th-15th centuries		1512-1522		1635
Archaeological Structure	Wall	Cistern	Core filling	16th Bastion	17th Bastion
Samples	CA-M2-1	CA-AL-2 *	CA-R-1	CA-B1-2	CA-B2-1
			CA-R-9	CA-B1-4	
	CA-M2-3	CA-AL-6 **	CA-R-7	CA-B1-11 #	CA-B2-3 #
			CA-R-8	CA-B1-13	

3.2. Methods

3.2.1. Mineralogical and Textural Characterisation

The mineral phases of mortars were determined by X-ray diffraction (XRD) in a powder sample using a Philips X'Pert diffractometer (Malvern PANalytical, Almelo, The Netherlands) equipped with a monochromatic Cu- $\text{K}\alpha 1$ X-radiation ($\lambda = 1.5405 \text{ \AA}$) operating at 40 kV and 20 mA analysis conditions. The data collection was performed by a continuous scanning angle in the range from 5 to 70° 2 θ and 0.02° s⁻¹ goniometer speed. Mineral phase identifications were performed with X'Pert HighScore Plus 3.0 software (Malvern PANalytical, Almelo, The Netherlands) using the experimental patterns of ICDD and ICSD diffraction databases.

The microtexture and mineralogical nature of mortar components were determined on polished thin-sections using a Nikon Eclipse LV100POL optical polarizing microscope equipped with DS F-I1 digital camera and a DS L-2 control unit in both transmitted and reflected polarized light modes. Comparison chart for visual percentage estimation was used to define the mortars binder/aggregate ratios [18].

3.2.2. Chemical Characterisation

Elemental chemical composition of major elements of mortars was determined by means of X-ray Fluorescence (XRF) using a Wavelength Dispersive X-ray Fluorescence (WDXRF) PANalytical Axios Advanced PW4400 XRF spectrometer with 4 kW Rh anode SST-mAX X-ray tube) with a detection limit of 0.01 wt %. Fused beads were obtained by melting the powder bulk mortar sample with lithium borate flux (Spectromelt A12, Merck) in 20:1 proportions at 1200 °C for 3 min in Pt/Au crucibles using a PANalytical PerI'X3. The loss on ignition (LOI) was calculated after heating the powder bulk mortar sample at 1050 °C for one hour.

3.2.3. Characterisation of Pore System and Hydric Behaviour

The pore size distribution and the open porosity (PMIP) were determined by mercury intrusion porosimetry (MIP) using a Poremaster-60 GT porosimeter (Quantachrome Instruments), with a maximum injection pressure of 414 MPa, measuring the pore diameter in a range of 0.003 to 360 μm . Mortar fragments of ca. 1 cm³ were oven-dried for 24 h at 60 °C

and then analysed. MIP analysis could not be performed in all samples due to the scarcity of the archaeological material.

Hydric tests (HT) were carried out to assess the parameters associated with fluid uptake and circulation through the pore system. Measurements were performed under controlled thermo-hygrometric conditions at 25 °C and 50% relative humidity on mortar samples 3 cm³ in size previously oven-dried at 80 °C for 24 h. Due to the archaeological nature of the samples, the hydric tests were performed on no more than two or three samples per mortar type. The free water absorption (A_b), forced water absorption (A_f , under vacuum) and absorption coefficient (C_a) were calculated following the UNE-EN 13755 [19] standard. The degree of pore interconnection (A_x) [20] and the saturation coefficient (S) [21] were also calculated. UNE-EN 1936 [22] standard was used to determine the open porosity (PHT) and skeletal ($\rho_{H_{sk}}$) and bulk (ρ_{H_b}) densities. Drying index (D_i) was determined according to the NORMAL 29/88 [23]. The capillarity coefficient (C_c) and the capillarity height (H_c) were determined according to the UNE-EN 1925 [24] standard.

3.2.3. Non-destructive Tests

Propagation velocity of ultrasonic pulses was measured in order to assess the mortar compactness using a Controls 58-E4800 ultrasonic pulse velocity tester with non-polarised piezoelectric couple transducers of 54 MHz. A viscoelastic couplant gel (Transonic gel) was used to ensure a proper contact between the transducers and the mortar sample. Measurements were performed under controlled thermo-hygrometric conditions at 25 °C and relative humidity of 50% on samples 3 cm³ in size previously oven-dried at 80 °C for 24 h. Test were performed on no more than two or three samples per mortar type. The propagation velocity of ultrasonic primary waves (V_p) was calculated according to the ASTM D 2845-05 [25] standard and the V_p values were used to calculate the structural anisotropy (ΔM) [26].

The colour of samples was measured according to the CIELAB colour space system following the UNE-EN 15886 [27] standard. The lightness (L^*) and chromatic (a^* and b^*) parameters were obtained using a Konica-Minolta CM-700d portable spectrophotometer under measurement conditions of 8 mm diameter, 10° view angle, D65 standard illuminant, with SCI/SCE modes and 400–700 nm wavelength range. Colour measurements were performed in five different points for each mortar sample and the mean value was calculated.

4. Results and Discussion

4.1. Mineralogical, Chemical and Textural Characterization

X-ray diffraction (XRD) analysis results are showed in Figure 2 and Table 2. All samples are mainly composed of magnesium calcite [(Ca,Mg)CO₃] and dolomite [CaMg(CO₃)₂] in different relative amounts. Quartz [SiO₂] was identified in minor amounts, highlighting its presence in both samples from the cistern (Samples CA-AL-2 and CA-AL-6) and the 17th century bastion (Samples CA-B2-1 and CA-B2-3). Hydromagnesite [(Mg₅(CO₃)₄(OH)₂·4H₂O)] and hydrotalcite [Mg₆Al₂(CO₃)(OH)₁₆·4(H₂O)] were also detected.

Hydrotalcite formation is favoured during the slaking process in the presence of Mg²⁺ and Al³⁺, [28] and hydromagnesite formation is favoured under high humidity conditions and in the presence of available magnesium [29]. Besides, presence of the Mg-phases contribute to the strength and durability of the magnesian mortars [30]. Presence of hydrotalcite in the mortar binder also constitutes a potential contaminant mineral for radiocarbon dating [28].

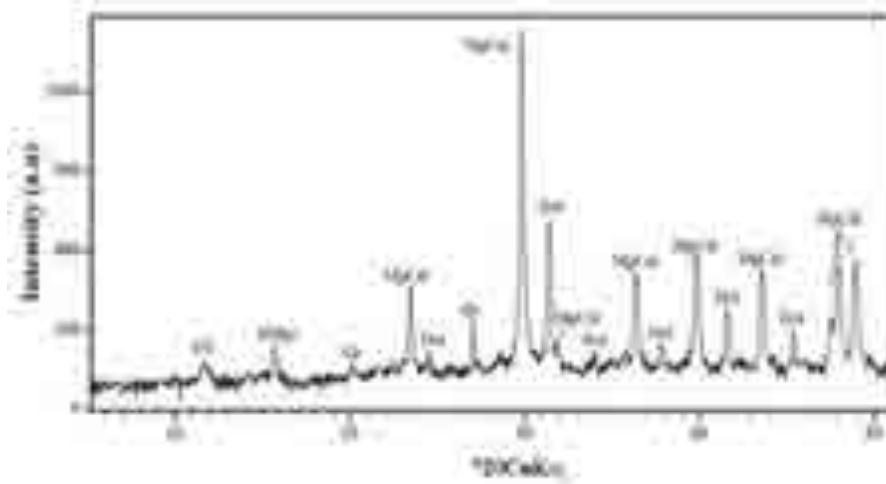


Fig. 2. The most representative X-ray diffraction pattern of the studied mortars. Dol: dolomite, HMgs: hydromagnesite, HT: hydrotalcite, Mg-Cal: magnesium calcite, Qz: quartz.

Table 2. X-ray diffraction results for the bulk lime mortar from Amaiur Castle. MgCal: magnesium calcite, Dol: dolomite; Qz: quartz, HMgs: hydromagnesite, HT: hydrotalcite. The amount is expressed as: -: undetected, tr: trace; *: low proportion; **: medium proportion; ***: high proportion; ****: predominant phase.

	CA-M2-1	CA-M2-3	CA-AL-2	CA-AL-6	CA-R-1	CA-R-7	CA-R-8	CA-R-9	CA-B1-2	CA-B1-4	CA-B1-11	CA-B1-13	CA-B2-1	CA-B2-3
MgCal	****	****	****	***	***	****	****	***	***	***	***	****	****	***
Dol	**	**	**	***	***	**	**	***	**	***	**	**	**	**
Qz	tr	*	*	*	tr	tr	tr	tr	*	tr	tr	tr	*	*
HMgs	-	*	-	-	tr	*	-	tr	-	-	-	tr	-	-
HT	tr	*	*	tr	tr	*	-	*	tr	tr	-	tr	-	-

The chemical composition determined by X-ray fluorescence (XRF in Table 3) is in accord with the mineral phases identified by XRD. The high CaO values (> 30 wt %) measured in all samples are mainly related to the calcite. However, MgO content is related to the presence of different amounts of dolomite, hydromagnesite and hydrotalcite. The Si values are mainly related to the presence of quartz in the samples, highlighting the higher values in samples CA-AL-2, CA-AL-6 and CA-M2-3. Al values are related to the hydrotalcite but the presence of Fe, K and Ti indicate the presence of phyllosilicates and feldspars that were not detected by XRD owing to them being under the detection limit of the technique. High LOI values (> 40 wt %) reflect the carbonated nature of the mineral phases of which mortars are mainly composed.

Table 3. X-ray fluorescence results of major elements in the bulk lime mortars from the Amaiur Castle. Results are expressed as oxides in wt%. Iron content is expressed as total Fe₂O_{3t}. LOI: loss on ignition (%).

	CA-M2-1	CA-M2-3	CA-AL-2	CA-AL-6	CA-R-1	CA-R-7	CA-R-8	CA-R-9	CA-B1-2	CA-B1-4	CA-B1-11	CA-B1-13	CA-B2-1	CA-B2-3
SiO ₂	3.27	4.29	4.56	4.34	2.57	2.24	3.89	3.42	3.43	3.45	2.22	2.25	2.33	3.39
Al ₂ O ₃	1.13	1.73	1.67	1.42	0.93	0.95	1.06	0.89	1.44	1.53	0.88	0.76	0.55	1.27
Fe ₂ O _{3t}	0.73	0.92	0.81	0.70	0.77	0.77	0.81	0.80	0.81	0.66	0.58	0.70	0.56	0.67
MnO	0.02	0.02	0.02	0.01	0.02	0.02	0.02	0.03	0.02	0.01	0.01	0.03	0.01	0.02
MgO	11.58	10.86	8.03	9.14	14.07	13.58	8.40	15.07	11.79	8.36	5.86	11.85	8.85	9.85
CaO	37.04	36.90	37.74	38.57	34.15	33.72	39.88	33.00	35.98	37.51	43.41	36.70	41.93	37.09
Na ₂ O	0.08	0.01	0.03	0.02	0.05	0.02	0.02	0.03	0.05	0.04	0.03	0.00	0.01	0.05
K ₂ O	0.17	0.22	0.36	0.33	0.20	0.16	0.23	0.25	0.32	0.20	0.15	0.11	0.08	0.17
TiO ₂	0.05	0.06	0.09	0.07	0.04	0.05	0.05	0.05	0.06	0.05	0.04	0.05	0.03	0.04
P ₂ O ₅	0.02	0.01	0.02	0.04	0.01	0.02	0.04	0.02	0.02	0.01	0.02	0.02	0.01	0.03
SO ₃	0.03	0.01	0.05	0.03	0.04	0.01	0.02	0.04	0.04	0.03	0.02	0.01	0.03	0.03
LOI	43.66	43.54	42.08	42.89	45.18	44.91	42.84	44.24	43.98	42.85	41.10	44.76	43.85	43.52



Fig. 3. Images of the most representative textures of the hand samples of the Amaïur Castle lime mortars. (a-c) Mortars showing a representative heterogeneous texture with angular to subangular carbonated aggregates. (d-f) Different grain sizes of subrounded ceramic fragments. (g) Filling mortar sample from the SE area showing the greatest amount of aggregates. (h) Filling mortar sample from the SW area showing the largest aggregates. (i) Mortar from the cistern showing the least amount of aggregates.

Macroscopically, all mortars show a heterogeneous texture in aggregate size, mainly of carbonated nature with angular to subangular shape (Fig. 3a-c). Subrounded ceramic fragments are also observed dispersed in the matrix of all samples (Fig. 3d and e) and the larger fragments of up to 1 cm in size correspond to the mortars from both bastions (Fig. 3f). Mortars from the fill stand out as they contain the highest aggregate content and largest in size, reaching more than 2 cm and poorly graded. Nevertheless, the filling mortars from the south-east area (Samples CA-R-1 and CA-R-9) show fewer aggregates than those from the south-west area (Samples CA-R-7 and CA-R-8) (Fig. 3g and h, respectively). On the other hand, mortar samples from the lunette and barrel vault base of the cistern (Samples CA-AL-2 and CA-AL-6, respectively) show the smallest amount of aggregates (Fig. 3i). Mineralogical nature, grading and shape of aggregates used in the mortar manufacture also play an important role in the mechanical behaviour of mortar and therefore they are important characteristics to consider in repair mortar formulation [31]. In this regard, the angular

carbonated aggregates with rough surface favour the nucleation of the binder calcite and the similar composition between both components leads to a better cohesion between the aggregates and binder, thus improving the mechanical strength of the mortar; e.g. [32-35]. Besides, the use of coarse aggregates in the manufacture of the filling mortar could have favoured the volume stability of the mixture, improving also the long-term strength [36].

The petrographic study reinforced the macroscopic observations, allowing a better characterization of the microtextural features of mortars. Microscopically, all samples show a heterogeneous binder matrix-supported texture with a binder/aggregate ratio between 1:2 and 1:1. Carbonated aggregates are angular to subangular dolostone fragments embedded in a micritic calcite matrix (Fig. 4a). Besides subrounded ceramic fragments (Fig. 4b), some subrounded sandstone fragments up to 2.5 mm in size are also observed (Fig. 4c). Quartz grains up to 0.6 μm in size are observed dispersed in the matrix; the largest appeared in the samples from the 17th bastion. All samples show heterometric dolostone fragments ranging from 0.1 mm to 2.5 mm in size whereas those larger than 5 mm were in the filling mortars (Fig. 4d). Lime lumps are also observed (Fig. 4e). Some samples show small dark spots in the binder related to an Mg-rich areas (Fig. 4f) from which, as well as from the edge of some pores, the growth of acicular crystals of hydromagnesite are observed, under both plane- and cross-polarized light (Figs. 4f and g). The presence of small hydromagnesite acicular crystals filling pores indicates that this Mg-phase was one of the last phases to crystallize. This is in agreement with the low Mg^{2+} and CO_2^{-3} concentrations needed for hydromagnesite crystallization [37]. Besides, the presence of hydromagnesite improves the cohesion between binder and aggregates, favouring the mortar strength [38].

Binder porosity is characterized by irregular shaped pores bigger than 500 μm in size. Sample CA-B1-4 from the 16th bastion stands out for its high porosity whereas the filling mortar samples from the SW area (Samples CA-R-7 and CA-R-8) show the lowest porosity (Figs. 4c and d). Dolostone fragments are characterized by vuggy porosity (Fig. 4g). Microcracks filled with secondary calcite can also be observed in the binder-matrix of Samples CA-AL-6, CA-B1-11 and CA-B2-3, and above all in Sample CA-M2-1 (Fig. 4h).

Dolomitic aggregates stand out because of their pronounced reaction zone, which can be observed in all images shown in Figure 4. According to the previous study [15], the reaction zone in the dolostone fragments was formed due to the dedolomitization of dolomitic aggregates as a result of a portlandite-dolomite reaction. This phenomenon, together with the fact that hydrotalcite has been detected in the binder, suggest that a traditional hot-mixing method was used for the manufacture of the studied mortars. Hot-mixed mortars are appropriate for damp and cold climates and show excellent workability and were frequently used for core filling and foundation works [39, 40]. In the traditional hot-mixing method the quicklime (CaO) is mixed with the aggregates and then slaked; reaching 200 °C and dropping below 100 °C as more water is added, until around 58 °C at the end of the slaking [41]. While hydrotalcite formation have been described in mortars cured at 60 °C [42, 43], temperatures over 50 °C are required for hydromagnesite crystallization [37, 44]. Thus, the presence of both phases supports the use of the hot-mixing method in the mortar manufacture at Amaiur Castle. Observed white lumps are also characteristic of hot-mixed mortars [40].

The high Ca and Mg values measured by XRF are consistent with the calcite binder matrix-supported texture of mortar and the dolomitic nature of the aggregates. Besides, even if they were not detected by XRD (Table 2), the K, Fe, Ti values are related to phyllosilicates, feldspars and oxides present in the ceramic fragments observed in the petrographic study.

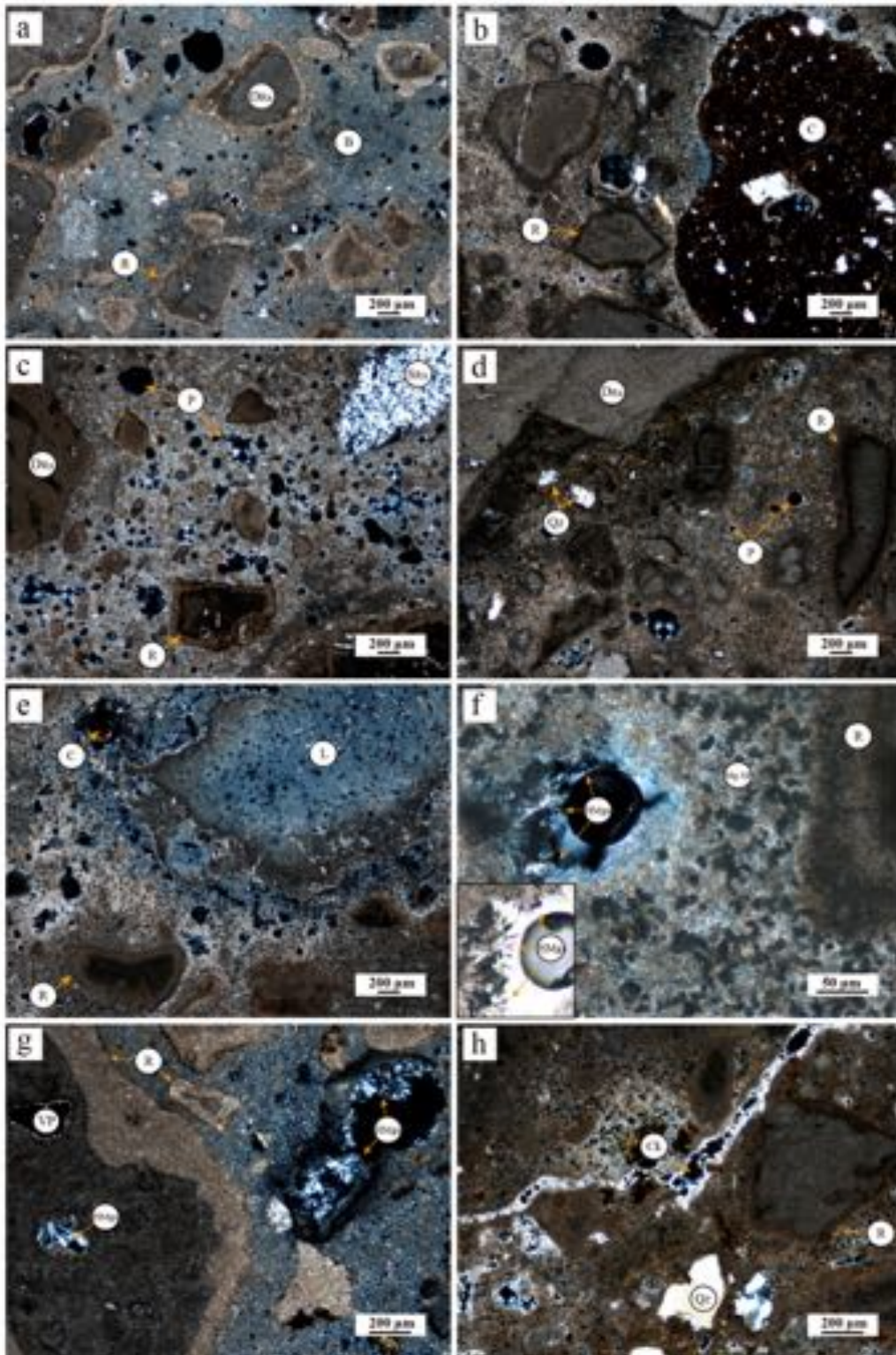


Fig. 4. Photomicrographs of the most representative microtextural features of the lime mortars from Amaïur Castle. (a) Heterogeneous binder matrix-supported texture with angular to subangular dolostone fragments embedded in a micritic calcite matrix. (b) Mortar with a subrounded ceramic fragment. (c) Sandstone aggregate in a mortar with high porosity. (d) Large dolostone aggregate in a mortar with low porosity. (e) Mortar with a lime lump. (f) Mortar with Mg-rich spots and hydromagnesite crystals. (g) Hydromagnesite crystals filling the binder pores and dolostone vuggy pores. (h) Microcracks with secondary calcite inside. Reaction zone in the dolomitic aggregates is shown in all photomicrographs. B: binder. C: ceramic fragment. SCal: secondary calcite. Ck: microcrack. DRx: dolostone. HMgs: hydromagnesite. L: lime lump. Mg-SP: Mg-rich spot. P: pore. Qz: quartz. R: reaction zone. SRx: sandstone. VP: vuggy porosity.

4.4. Characterization of Pore System and Hydric Behaviour

Mortars show a complex pore system since they are composed of both porous binder and different porous aggregates [45]. Water constitutes an important degradation agent for building materials since its circulation and retention within the porous materials causes their deterioration and in some cases irreversible damage. Therefore, mortar characterization through the porous system is essential since the porosity and pore size distribution affect the water circulation within the material [46, 47].

Mercury intrusion porosimetry (MIP) was used to evaluate the pore size distribution of the mortars. Table 4 summarises the obtained MIP values. The highest porosity values (PMIP) were measured in Samples CA-B1-4 and CA-B2-3 (45% and 37.8%, respectively), whereas the lowest value were measured in Sample CA-R-8 and Sample CA-B1-13 (26.3% and 27.7%, respectively).

Table 4. Hydric parameters and porosity values of the lime mortars from Amaiur Castle. A_b : Free water absorption (%). A_f : forced water absorption (%). A_x : degree of pore interconnection (%). S : Saturation coefficient (%). C_a : absorption coefficient ($\text{g}/\text{min}^{0.5}$). D_i : drying index. ρ_{Hb} : bulk density (g/cm^3). ρ_{Hsk} : skeletal density (g/cm^3). C_c : capillarity coefficient ($\text{g}/\text{cm}^2 \text{min}^{0.5}$). H_c : Height of the water level during capillary uptake ($\text{mm s}^{-0.5}$). P_{HT} and P_{MIP} : open porosity (%) determined by hydric tests (HT) and mercury intrusion porosimetry (MIP), respectively.

	CA-M2-1	CA-M2-3	CA-AL-2	CA-AL-6	CA-R-1	CA-R-7	CA-R-8	CA-R-9	CA-B1-2	CA-B1-4	CA-B1-11	CA-B1-13	CA-B2-1	CA-B2-3
A_b	24.10	19.38	20.40	18.90	15.80	29.58	22.63	15.18	18.61	31.59	16.49	16.34	17.99	17.58
A_f	25.05	20.04	20.96	19.24	16.30	31.54	25.22	16.28	19.27	33.13	19.59	17.98	22.60	17.75
A_x	3.81	3.30	2.67	1.76	3.06	6.22	10.28	6.75	3.40	4.65	15.85	9.11	20.41	1.00
S	91.95	93.40	94.46	96.92	96.37	90.25	87.76	92.16	91.84	91.16	72.91	90.65	78.78	96.00
C_a	12.05	9.69	10.20	9.45	7.90	14.79	11.32	7.59	9.31	15.79	8.24	8.17	8.99	8.79
D_i	0.246	0.249	0.248	0.249	0.251	0.244	0.247	0.251	0.249	0.240	0.248	0.249	0.247	0.249
ρ_{Hb}	1.57	1.68	1.68	1.73	1.79	1.34	1.52	1.79	1.72	1.34	1.63	1.64	1.49	1.72
ρ_{Hsk}	2.59	2.54	2.59	2.59	2.53	2.31	2.47	2.52	2.58	2.40	2.39	2.33	2.26	2.48
C_c	0.040	0.024	0.022	0.030	0.010	0.023	0.021	0.014	0.028	0.028	0.022	0.020	0.017	0.029
H_c	0.81	0.65	0.65	0.65	0.58	0.65	0.97	0.65	0.78	0.97	1.16	0.97	1.03	1.18
P_{HT}	39.3	33.8	35.1	33.3	29.2	42.2	38.4	29.1	33.2	44.3	31.9	29.6	33.8	30.5
P_{MIP}	34.1	31.4	31.6	-	31	-	26.3	-	31	45	-	27.7	29.2	37.8

Regarding the pore size distribution (Fig.5), all samples show a family of small pores of $0.01 < r < 1 \mu\text{m}$ connected to a family of large pores of $1 < r < 10 \mu\text{m}$, showing a greater volume of pores of $0.1 < r < 1 \mu\text{m}$ characteristic of the matrix of lime mortars [48, 49]. Samples CA-B1-2 and CA-B2-1 are also characterized by a family of large pores of $10 < r < 100 \mu\text{m}$. The bimodal pore size distribution with two main peaks situated at around $0.1 \mu\text{m}$ and at around $1 \mu\text{m}$ is characteristic in most of samples, except for Samples CA-M2-1 and CA-B2-3 that show a nearly unimodal pore size distribution with a main peak at around $1 \mu\text{m}$. The Samples CA-B1-4 and CA-B2-3 not only stand out for the highest PMIP values but also for, respectively, a marked bimodal and unimodal pore size distribution (Fig. 5).

The family of smaller pores is related to the aggregates porosity, although some dolostone fragments show scarce larger pores, whereas the larger pore family is related to the binder porosity (Fig. 4). Furthermore, the porosity and the pore distribution could have been modified due to deterioration, which would explain the higher porosity values and a larger pore size.

The study of the hydric properties is also of great importance to evaluate the pore system and to assess the susceptibility of mortars to deterioration. Hydric tests (HT) were performed for a better study of the pore system and to evaluate the hydric behaviour of samples (Fig. 6 and Table 4).

The degree of pore interconnection values (A_x) was lowest in Samples CA-AL-2, CA-AL-6 and CA-B2-3 ($< 3\%$), indicating a better pore interconnection that favours water flow through the mortar. In contrast, Samples CA-R-8, CA-B1-11, CA-B1-13 and CA-B2-1 show the highest A_x values ($> 9\%$), which indicates greater difficulty of water to flow due to worse pore interconnection. Considering the lowest A_x values of the samples from each structure (Table 4), Sample CA-AL-6, Sample CA-M2-3 (from the south-west) and Samples CA-R-1, CA-B1-2, CA-B1-4 and CA-B2-3 (from the south-east) show the lower A_x values. Samples with better pore interconnection are those that display a higher saturation coefficient (S), since S values are related to the A_x parameter.

Regarding the drying curve, at the beginning of the test the drying rate is constant. Curves closer to the vertical correspond to the samples that dry faster (Fig. 6a). Once the critical moisture content is reached the drying rate decreases and pore size and pore interconnection are the factors controlling the drying velocity [50]. Samples with highest drying index values ($D_i > 0.248$) dry more slowly and the porous system remains full of water for longer. Samples CA-R-1 and CA-R-9 stand out for taking the longest to dry ($D_i = 0.251$) while Sample CA-B1-4 for drying faster ($D_i = 0.240$).

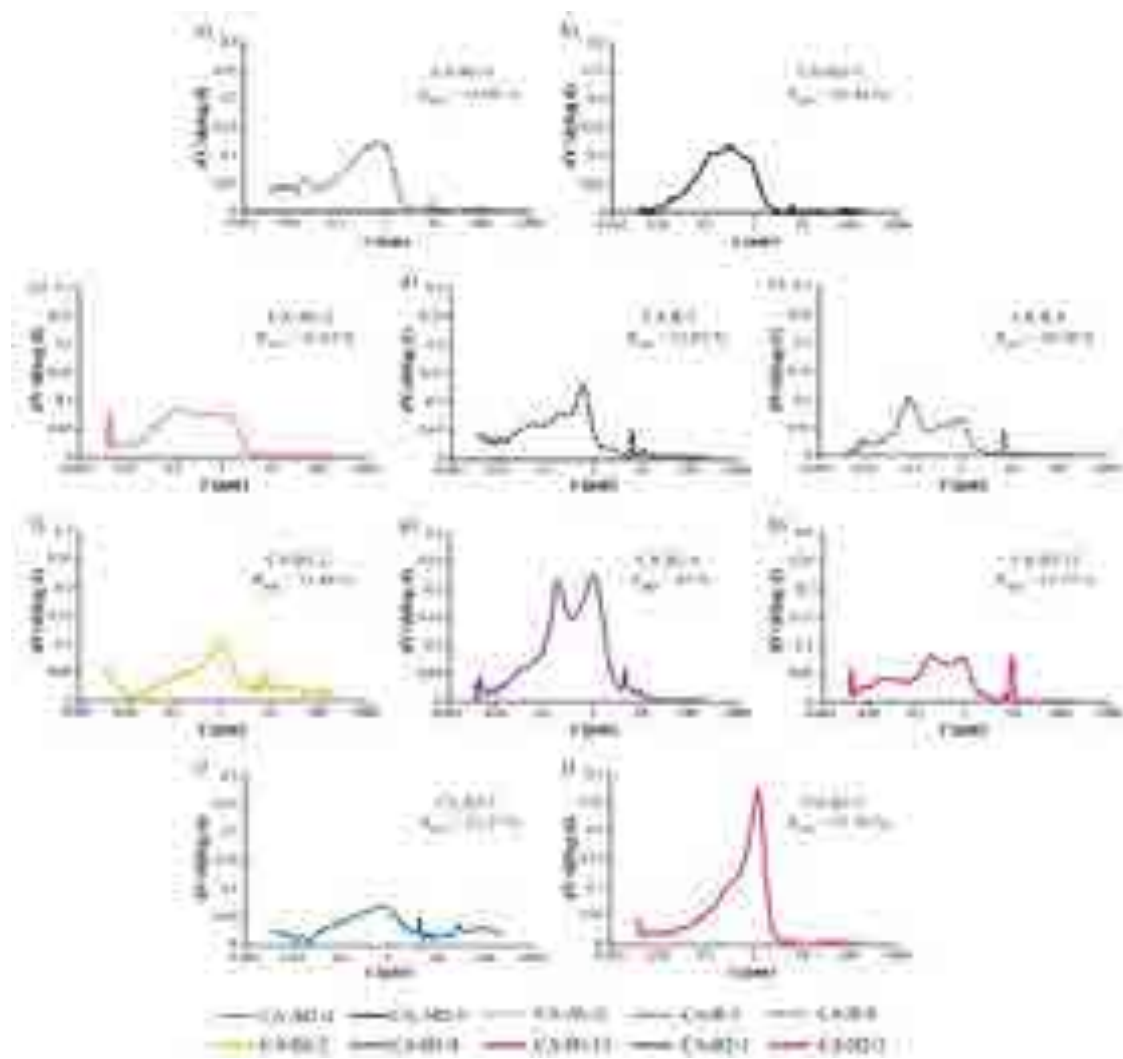


Fig. 5. Pore size distribution curves of lime mortars from Amaiur Castle obtained by mercury intrusion porosimetry. (a) CA-M2-1, (b) CA-M2-3, (c) CA-AL-2, (d) CA-R-1, (e) CA-R-8, (f) CA-B1-2, (g) CA-B1-4, (h) CA-B1-13, (i) CA-B2-1, (j) CA-B2-3. Accessible pore radius (in μm) vs. incremental pore volume (in cm^3/g) is represented.

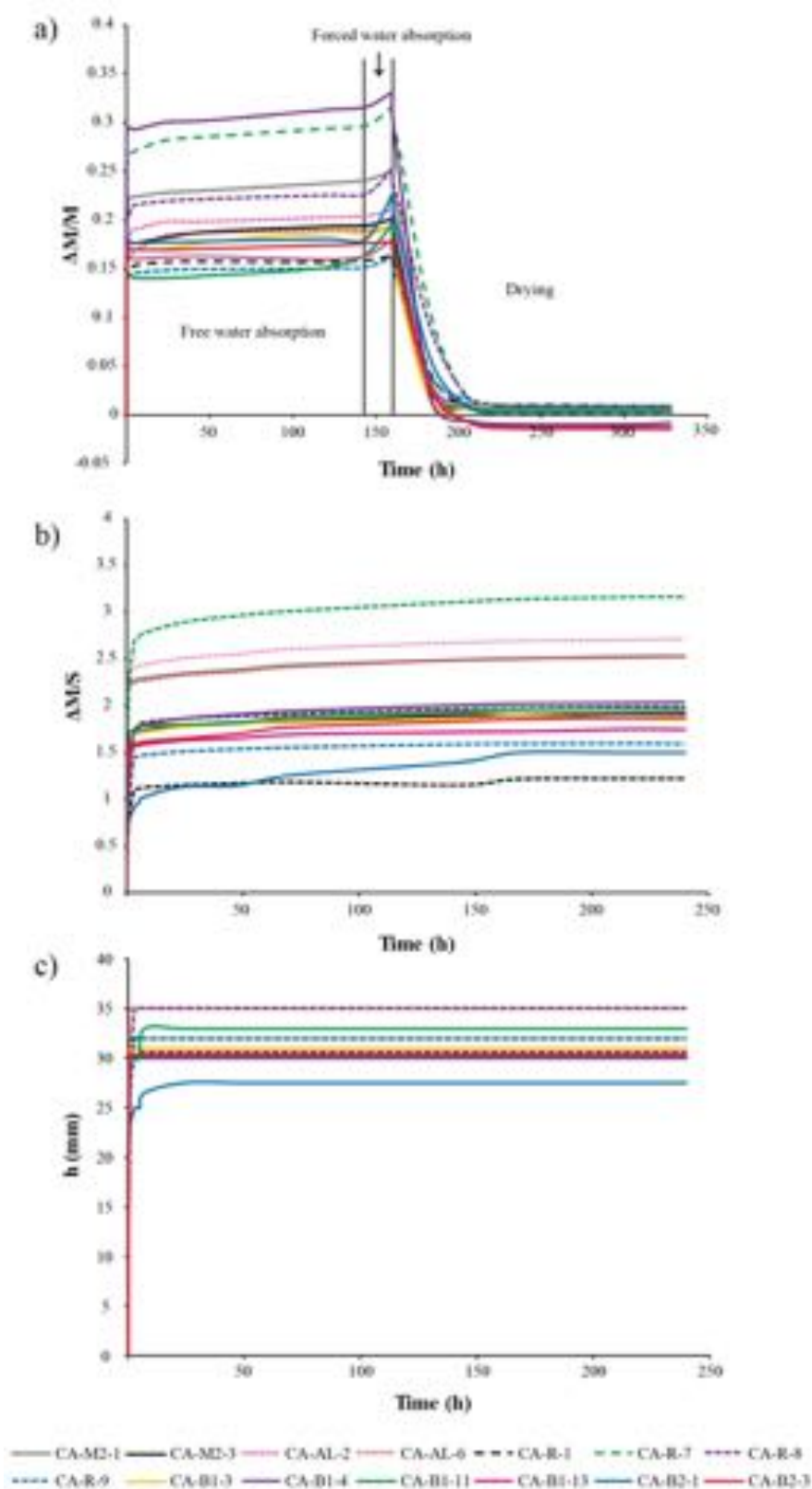


Fig. 6. Hydraic behaviour of the lime mortars from Amaiur Castle. (a) Free water absorption, forced water absorption and drying curves. Weight variation ($\Delta M/M$) versus time (in hours). (b) Capillarity curves. Weight variation ($\Delta M/S$) versus time (in hours) and (c) capillarity front curves. Height (in mm) versus time (in hours).

Capillary uptake curves (Fig. 6b) show the typical capillary rise trend for lime mortars characterized by two different slopes [51, 52]. The first sharp slope is related to rapid water absorption at the beginning of the test. From 24 h of the test, the absorption velocity decreased and the water uptake became slow and continuous leading to a more linear slope until saturation at 250 h. Capillary front of all samples also reached the top after 24 h (Fig. 6c). The two slopes in the capillary uptake curve and the time-lag between visual and real saturation confirms the two main pore families ($0.01 < r < 1 \mu\text{m}$ and $1 < r < 10 \mu\text{m}$) detected by MIP analysis in which the family of smaller pores saturates before the family of larger pores [51]. The water amount absorbed by capillarity was higher in Samples CA-A1-6 and CA-R-7 while Samples CA-R-1 and CA-B1-2 absorbed the least amount of water. Capillarity water uptake was faster in Samples CA-M2-1, CA-B1-2, CA-B1-4, CA-B2-3 and CA-AL-6, which showed a higher capillarity coefficient (CC) ($> 0.025 \text{ g/cm}^2 \text{ min}^{0.5}$) while Samples CA-R-1 and CA-R-9 displayed the slowest values ($< 0.015 \text{ g/cm}^2 \text{ min}^{0.5}$) (Table 4). Microcracks in Samples CA-M2-1 CA-AL-6 and CA-B2-3 (Fig. 3h) could have favoured the capillarity water uptake.

Open porosity values from the hydric tests (P_H) were highest in Samples CA-B1-4 and CA-R-7 (44.33% and 42.17%, respectively) and lowest in south-west filling mortars (Sample CA-R-1 with 29.17% and Sample CA-R-9 with 29.11%). Considering the higher P_H values of the samples from each structure (Table 4), the highest P_H values were obtained for mortars from the south-east medieval wall and bastions (Samples CA-M2-1, CA-B1-2, CA-B1-4 and CA-B2-1), south-west filling mortars (Samples CA-R-7 and CA-R-8) and mortar from the lunette vault (Sample CA-AL-2).

The greatest amount of water was absorbed by the samples with the highest P_H values (Table 4 and Fig. 6a). Samples CA-M2-1, CA-B1-4, CA-R-7, CA-R-8 and CA-A1-2 showed the highest values ($> 20\%$) of free water absorption (A_b) and forced water absorption (A_f) and were the fastest absorbing the water (high C_a values in Table 4). Sample CA-B2-1 also absorbed a large amount of water by forced absorption.

The P_H values were similar to the values obtained by mercury intrusion porosimetry (P_{MIP}). Nevertheless, the slight differences between both porosities are caused by the two different fluids used and the different exerted pressures (water at atmospheric pressure in the HT and mercury at 414 MPa in MIP analysis). Samples with the highest open porosity values show the greatest difference between skeletal and bulk densities (ρ_{Hsk} and ρ_{Hb} , respectively) (Table 4).

4.5. Ultrasonic Pulse Velocity Test

Ultrasonic pulse velocity test is a non-destructive test that allows to evaluate features concerning the porosity and anisotropies in the mortar [53]. Table 5 summarizes values of the propagation velocity of ultrasonic primary waves (V_p) and structural anisotropy (ΔM).

Table 5. Results of the ultrasonic pulse velocity test in the lime mortars from Amaiur Castle. V_{p1} , V_{p2} and V_{p3} : P-wave velocity in the three orthogonal directions (in m/s). ΔV_p : Average value of the P-wave velocities. σV_p : standard deviation. ΔM : structural anisotropy (%).

	CA-M2-1	CA-M2-3	CA-AL-2	CA-AL-6	CA-R-1	CA-R-7	CA-R-8	CA-R-9	CA-B1-2	CA-B1-4	CA-B1-11	CA-B1-13	CA-B2-1	CA-B2-3
V_{p1}	157.61	237.70	188.17	190.22	279.28	225.16	257.58	271.60	244.27	213.06	233.90	239.13	223.77	210.42
V_{p2}	160.40	244.09	204.82	211.18	295.77	253.73	277.31	285.09	248.06	224.49	250.03	253.77	229.39	216.81
V_{p3}	170.27	250	193.18	193.71	290.18	230.26	272.73	277.31	264.46	215.95	235.49	239.90	244.19	219.03
ΔV_p	162.76	243.93	195.39	198.37	288.41	236.38	269.21	278	252.26	217.83	239.81	244.27	232.45	215.42
σV_p	6.65	6.15	8.54	11.23	8.39	15.24	10.33	6.77	10.73	5.94	8.87	8.24	10.54	4.47
ΔM	4.67	3.78	5.44	6.04	4.67	6.95	6.34	3.42	4.68	3.25	3.64	3.12	5.49	3.44

P-wave velocity could vary according to the mineralogy, texture and porosity of the material [47, 54]. All studied samples show the same mineralogy with slight variations, thus the texture and porosity will be the main factors that affect the V_p values. While the variation in the velocity of the P-waves is not related to the size of aggregates, the high calcareous aggregate content favours the increase in velocity [55-57]. The higher V_p values were measured in samples with a larger amount of aggregates (Samples CA-R-1 and CA-R-9, corresponding to filling mortars from the SE area), whereas the lower values were obtained in the mortars with the lowest aggregates content (Samples CA-AL-2 and CA-AL-6 from the cistern) (Figs. 2 g-h and i, respectively). Propagation velocity of ultrasonic pulses is also affected by the porosity, with the V_p value decreasing with higher porosity [9, 57]. Accordingly, the lowest V_p values were detected in the samples with the highest porosity values as measured in MIP analysis and hydric tests (Table 4), and observed in the petrographic study (Figs. 4c and d). Besides, the small-scale anisotropies within the material such as microcracks not only affect the water circulation but also decrease the V_p values [58, 59]. Thus, the high frequency of microcracks in Sample CA-M2-1 (Fig. 4h) could explain the lowest V_p value measured in this sample (Table 5). Structural anisotropy (ΔM) confirms the heterogeneous mortar texture of all mortars. The large size of aggregates from the south-west filling mortar samples (Samples CA-R-7 and CA-R-8) explains the high ΔM values.

4.5. Colorimetry

Compatibility between the repair mortar and the original mortar in terms of visual appearance is also an important requirement to consider in restoration work [4, 60]. The colour of mortars was evaluated by non-destructive colorimetric analyses using the CIELAB (CIE 1976 $L^*a^*b^*$) colour space system proposed by the International Commission on Illumination (CIE). Chromatic parameters of each mortar sample are summarised in Table 6. The lightness (L^*) values around 80 and the values measured for the chromatic axes (a^* and b^*) indicated samples with a tendency toward to the light grey field. The lower L^* values were measured in Samples CA-AL-6, CA-R-8, CA-B1-4, CA-B2-1 and CA-B2-3. The a^* and b^* values are similar in all samples, although Samples CA-M2-1 and samples from the cistern (CA-AL-2, CA-AL-6) and from the 17th century bastion (CA-B2-1 and CA-B2-3) show higher values. The high chromatic axes values and the low L^* values of samples from the 17th century bastion are explained by the presence of ceramic fragments in the mortar.

Table 6. Chromatic parameters of historic lime mortar samples from Amaiur Castle. L^* : Lightness, a^* and b^* : chromatic coordinates, C^* : chroma, H: hue angle.

	CA-M2-1	CA-M2-3	CA-AL-2	CA-AL-6	CA-R-1	CA-R-7	CA-R-8	CA-R-9	CA-B1-2	CA-B1-4	CA-B1-11	CA-B1-13	CA-B2-1	CA-B2-3
L^*	80.70	83.60	82.05	77.41	80.10	85.19	77.92	80.83	81.02	84.37	83.14	79.24	79.42	73.70
a^*	2.75	1.70	1.806	2.00	1.46	2.05	1.81	1.32	2.00	1.47	2.18	2.52	2.49	3.89
b^*	12.06	8.76	10.76	10.94	7.87	9.02	8.37	8.76	9.99	7.76	9.77	9.56	10.44	13.99
C^*	12.37	8.93	10.91	11.13	8.00	9.26	8.56	8.86	10.19	7.90	10.02	9.89	10.73	14.52
H	77.25	79.10	80.48	79.63	79.63	77.04	77.83	81.49	78.62	79.20	77.45	75.22	76.59	74.46

The works and repairs carried out in the castle over time as a result of the conflicts in the region represent an additional complexity in the study of mortars. In the General Archives of Simancas, different repairs are documented, including a repair in the south-east structure of the 16th century bastion [17, 61, 62], the area where Sample CA-B1-4 was located. It could explain the clearly different hydric parameters and porosity values of this sample from the rest (Table 4).

4.6. Environmental considerations

Environmental factors such as relative humidity, rainfall and temperature also affect mortar durability. Geographically, Amaiur Castle is located in the Oceanic maritime west coast climate zone (Cfb in the Köppen-Geiger climate classification) [63, 64].

Annual average relative humidity in the area of the castle is 83.4%, reaching values above 86% in some months. The average annual precipitation is around 2040 mm, with rainfall above 90 mm throughout all months of the year and reaching above 200 mm in the wettest months [65, 66]. At relative humidity values between 65% and 95%, the water vapour and water liquid coexist leading to the continuous presence of water within the pore system [45]. However, besides moistening the mortar, the meteoric water could also incorporate soluble CO₂ and salts inside the pores. While dissolved CO₂ favours the partial dissolution of carbonates, the volume increase due to the crystallization of secondary carbonates and/or soluble salts within the pores results in mechanical stress contributing to the mortar deterioration [67-69].

Furthermore, mortars at Amaiur Castle are exposed to continuous temperature variations since, even if the annual average temperature is 12.9 °C, the annual absolute average minimum temperature reaches -19 °C and the annual absolute average maximum temperature 41 °C [65]. Continued temperature variations over time may lead to the cracking of mortar since the thermal expansion produced by the crystallisation of water into ice in colder periods also results in a mechanical stress [70].

Even if the cold and wet local environmental conditions at Amaiur Castle could have been advantageous for the hot-mixing method, since it was commonly used in cold-weather work [40], the high humidity, the continuous rainfall and the temperature variation over a broad range of the area contribute to the current weathering of Amaiur Castle lime mortars.

Considering the samples from each different structure, the high porosity, high water absorption capacity and poor pore interconnection (high A_x) of Samples CA-M2-1, CA-AL-2, CA-R-7, CA-R-8 and CA-B2-1 favour mortar decay since their tortuous pore system hinders the water flow outward. Although Samples CA-B1-4 dries the fastest (low D_i), its high porosity and water absorption capacity could also affect the durability. Sample CA-AL-6 is more susceptible to deterioration by capillarity since it not only absorbs a greater amount of water by capillarity but also uptakes the water faster. Furthermore, Samples CA-B1-11 and CA-B1-13 took longer to dry (high D_i) and show poor pore interconnection (high A_x), which leads to water retention inside for longer, favouring mortar decay.

5. Conclusions

Mineralogical, chemical and physical characterization performed in the present study has contributed to a better understanding of the historic lime mortars from Amaiur Castle and the results achieved have been able to address specific goals:

Susceptibility to mortar deterioration

Samples from the 14th-15th century wall show very similar mineralogical, chemical and textural characteristics, but the high presence of microcracks in the south-east sample point to its worst conservation.

The poor pore interconnection of samples from the SW structure of the 16th century bastion and the SE samples of the 17th century diamond-shaped structure makes them more susceptible to decay since water is retained longer.

The south-east sample from the 16th century bastion could be related to the repairs performed during the 16th century as the hydric parameters and porosity values are clearly differentiated in comparison with the rest of the samples.

The water absorption capacity of samples from the lunette and barrel vault base could affect the preservation of the only cistern vault remains currently preserved.

Filling mortar shows a different hydric behaviour and pore system between the south-east and south-west area. Filling mortars from the south-west area are more susceptible to deterioration not only because they show a higher porosity and water absorption capacity but also due to the poor interconnection of pores and the difficulty in drying.

Environmental conditions at Amaiur Castle (high humidity, continuous rainfall and the temperature variation over a broad range) also favour the weathering of mortars. On the other hand, the high humidity conditions could have favored the hydromagnesite crystallization in the binder.

Approach to technological knowledge

Mineralogical and textural characterization has also allowed an exploration of the technological knowledge used in the mortar manufacturing process.

Filling mortar shows larger aggregates, probably used to stabilize the mortar volume and to improve the long-term strength. Differences in aggregate size and in the physical features between the filling mortar from the south-west area and the south-east suggest at least two different filling periods.

Selection of angular carbonated aggregates would have improved the mechanical strength of the mortar.

Presence of hydrotalcite and hydromagnesite in the mortar binder would also have favoured the mortar strength.

Identification of hydromagnesite in the present study support the use of the traditional hot-mixing method in the mortar manufacture at Amaiur Castle, a method that might have been appropriate for the damp and cold area in which the castle is located.

Contribution to heritage conservation and future perspectives

The present study represents a valuable reference for the suitable formulation of a compatible repair mortar that ensures the architectural heritage conservation in future restoration works at Amaiur Castle.

Harsh environmental factors in the studied area make it necessary to perform future decay tests for a better assessment of historic lime mortar deterioration.

The different structures from different periods at Amaiur Castle, due to changes in the defences of the building, resulted in mortars with different textural characteristics.

Evolution in the Amaiur Castle defences led to the construction of different structures in different periods resulting in mortars with different textural characteristics. Future studies on the mechanical properties will be able to obtain a better understanding of changes in mortar manufacture according to the evolution of the defensive structures.

Acknowledgments

This study was supported by the GIC18/133 Research Group of the University of the Basque Country (UPV/EHU) and of Junta de Andalucía Research Group RNM179 and Research Project MAT2016-75889-R. G.P.-A. acknowledges the PhD research grant of the Basque Government [2015-1-02-35]. The authors also would like to thank Peter Smith for reviewing the use of English in the manuscript.

References

- [1] W. Wallace, On ancient mortars, *Chemical News* 11 (1865) 185-186.
- [2] Venice, Charter, International Charter for the Conservation and Restoration of Monuments and Sites. Available online: http://icomos.org/charters/venice_e.pdf (accessed on 27 March 2020). (1964).
- [3] C. Groot, G.J. Ashall, J.J. Hughes, P.J. Bartos, Characterisation of old mortars with respect to their repair: A state of the art, *RILEM REPORT* 28 (2007) 1.
- [4] L. Schueremans, Ö. Cizer, E. Janssens, G. Serré, K.V. Balen, Characterization of repair mortars for the assessment of their compatibility in restoration projects: Research and practice, *Construction and Building Materials* 25(12) (2011) 4338-4350.
- [5] ICOMOS, Declaration of Amsterdam. Available online: <https://www.icomos.org/en/and/169-the-declaration-of-amsterdam> (accessed on 10 January 2020). (1975).
- [6] N.S. Martys, C.F. Ferraris, Capillary transport in mortars and concrete *Cement and Concrete Research* 27(5) (1997) 747-760.
- [7] R.P.J. Van Hees, L. Binda, I. Papayianni, E. Toubakari, Characterisation and damage analysis of old mortars, *Materials and Structures* 37 (2004) 644-648.
- [8] C. Borges, A. Santos Silva, R. Veiga, Durability of ancient lime mortars in humid environment, *Construction and Building Materials* 66 (2014) 606-620.
- [9] A. Arizzi, G.M. Huerga, E. Sebastián, G. Cultrone, Mineralogical, textural and physical-mechanical study of hydraulic lime mortars cured under different moisture conditions, *Materiales de construcción* 65(318) (2015).
- [10] J.J. Hughes, S.J. Cuthbert, The petrography and microstructure of medieval lime mortars from the west of Scotland: Implications for the formulation of repair and replacement mortars, *Materials and Structures* 33(9) (2000) 594-600.
- [11] I. Papayianni, V. Pachta, M. Stefanidou, Analysis of ancient mortars and design of compatible repair mortars: The case study of Odeion of the archaeological site of Dion. , *Construction and Building Materials* 40 (2013) 84-92.
- [12] H. Morillas, P. Vazquez, M. Maguregui, I. Marcaida, L.F.O. Silva, Composition and porosity study of original and restoration materials included in a coastal historical construction, *Construction and Building Materials* 178 (2018) 384-392.
- [13] G. Borsoi, A.S. Silva, P. Menezes, A. Candeias, J. Mirão, Analytical characterization of ancient mortars from the archaeological roman site of Pisões (Beja, Portugal), *Construction and Building Materials* 204 (2019) 597-608.
- [14] G. Ponce-Antón, A. Arizzi, M.C. Zuluaga, G. Cultrone, L.A. Ortega, J. Agirre Mauleon, Mineralogical, Textural and Physical Characterisation to Determine Deterioration Susceptibility of Irulegi Castle Lime Mortars (Navarre, Spain), *Materials* 12(4) (2019) 584.
- [15] G. Ponce-Antón, M.C. Zuluaga, L.A. Ortega, J.A. Mauleon, Multi-analytical approach for chemical-mineralogical characterization of reaction rims in the lime mortars from Amaiur Castle (Navarre, Spain), *Microchemical Journal* 152 (2020) 104303.
- [16] I. Sagredo, Navarra. Castillos que defendieron el reino (Tomo I) de Laguardia a Foix, y del Moncayo al Goierri, Pamiela Ed., Pamplona, 2006.
- [17] I. Sagredo, El castillo de Amaiur a través de la historia de Navarra, Pamiela Ed., Pamplona, 2009.
- [18] R.L. Folk, A comparison chart for visual percentage estimation, *Journal of Sedimentary Research* 21(1) (1951) 32-33.
- [19] UNE-EN 13755 Natural stone test methods determination of water absorption at atmospheric pressure, 2008., AENOR, Madrid.
- [20] G. Cultrone, M.J. De La Torre, E. Sebastián, O. Cazalla, Evaluation of bricks durability using destructive and nondestructive methods (DT and NDT), *Materiales de Construcción* 53(269) (2003) 41-59.
- [21] RILEM, Recommended test to measure the deterioration of stone and to assess the differences of treatment methods., *Materials and Structures* 13 (1980) 175-253.
- [22] UNE-EN 1936, Natural stone test methods. Determination of real density and apparent density, and of total and open porosity, 2007., AENOR, Madrid.
- [23] NORMAL 29/88, Misura dell'indice di asciugamento (drying index), 1988., CNR-ICR, Rome.

- [24] UNE-EN 1925, Natural stone test methods. Determination of water absorption coefficient by capillarity, 2000., AENOR, Madrid.
- [25] ASTM D 2845-05, Standard method for laboratory determination of pulse velocities and ultrasonic elastic constants of rock, 2005., ASTM International Standards Worldwide, Pennsylvania.
- [26] J. Guyader, A. Denis, Wave propagation in anisotropic rocks under stress evaluation of the quality of slates, *Bulletin of the International Association of Engineering Geology - Bulletin de l'Association Internationale de Géologie de l'Ingénieur* 33(1) (1986) 49-55.
- [27] UNE-EN 15886, Conservation of cultural property. Test methods. Colour measurement of surfaces, 2011., AENOR, Madrid
- [28] G. Ponce-Antón, L.A. Ortega, M.C. Zuluaga, A. Alonso-Olazabal, J.L. Solaun, Hydrotalcite and Hydrocalumite in Mortar Binders from the Medieval Castle of Portilla (Álava, North Spain): Accurate Mineralogical Control to Achieve More Reliable Chronological Ages, *Minerals* 8(8) (2018) 326.
- [29] A. Arizzi, G. Cultrone, The difference in behaviour between calcitic and dolomitic lime mortars set under dry conditions: The relationship between textural and physical–mechanical properties, *Cement and Concrete Research* 42(6) (2012) 818-826.
- [30] A. Diekamp, J. Konzett, P.W. Mirwald, Magnesian lime mortars–Identification of magnesium phases in medieval mortars and plasters with imaging techniques, 12th Euroseminar on Microscopy Applied to Building Materials, Dortmund, Germany, 2009, pp. 15-19.
- [31] A.R. Santos, M. do Rosario Veiga, A.S. Silva, J. de Brito, J.I. Álvarez, Evolution of the microstructure of lime based mortars and influence on the mechanical behaviour: the role of the aggregates, *Construction and Building Materials* 187 (2018) 907-922.
- [32] J. Lanás, J.I. Alvarez-Galindo, Masonry repair lime-based mortars: factors affecting the mechanical behavior, *Cement and Concrete Research* 33(11) (2003) 1867-1876.
- [33] G. Cultrone, E. Sebastian, M.O. Huertas, Durability of masonry systems: A laboratory study, *Construction and Building Materials* 21(1) (2007) 40-51.
- [34] A. Arizzi, J. Martínez Martínez, G. Cultrone, D. Benavente, Mechanical evolution of lime mortars during the carbonation process, *Key Engineering Materials*, Trans Tech Publications 2011, pp. 483-486.
- [35] A. Arizzi, G. Cultrone, The influence of aggregate texture, morphology and grading on the carbonation of non-hydraulic (aerial) lime-based mortars, *Quarterly Journal of Engineering Geology and Hydrogeology* 46(4) (2013) 507-520.
- [36] M. Stefanidou, I. Papayianni, The role of aggregates on the structure and properties of lime mortars, *Cement and Concrete Composites* 27(9-10) (2005) 914-919.
- [37] M. Back, M. Bauer, H. Stanjek, S. Peiffer, Sequestration of CO₂ after reaction with alkaline earth metal oxides CaO and MgO, *Applied Geochemistry* 26(7) (2011) 1097-1107.
- [38] R.M. Dheilily, A. Bouguerra, B. Beaudoin, J. Tudo, M. Queneudec, Hydromagnesite development in magnesian lime mortars, *Materials Science and Engineering A268* (1999) 127–131.
- [39] A. Forster, Hot-lime mortars: a current perspective, *Journal of Architectural Conservation* 10(3) (2004) 7-27.
- [40] A. Henry, J. Stewart, Practical building conservation: Mortars, renders & plasters, Practical Building Conservation. English Heritage, Surrey 2011.
- [41] N. Copsey, Hot mixed lime and traditional mortars : a practical guide to their use in conservation and repair, The Crowood Press, Ramsbury, Marlborough, 2019.
- [42] M. Zajac, S.K. Bremseth, M. Whitehead, M. Ben Haha, Effect of CaMg(CO₃)₂ on hydrate assemblages and mechanical properties of hydrated cement pastes at 40°C and 60°C, *Cement and Concrete Research* 65 (2014) 21-29.
- [43] A. Machner, M. Zajac, M. Ben Haha, K.O. Kjellsen, M.R. Geiker, K. De Weerd, Limitations of the hydrotalcite formation in Portland composite cement pastes containing dolomite and metakaolin, *Cement and Concrete Research* 105 (2018) 1-17.
- [44] J. Lanás, J.I. Alvarez, Dolomitic limes: evolution of the slaking process under different conditions, *Thermochimica Acta* 423(1-2) (2004) 1-12.
- [45] M. Thomson, J.E. Lindqvist, J. Elsen, C.J.W.P. Groot, 2.5. Porosity of mortars, in: C. Groot, G. Ashall, J. Hughes (Eds.) *Characterisation of Old Mortars with Respect to their Repair-State of the Art*. Report of RILEM Technical Committee 167-COM, 2007, pp. 77-106.

- [46] P. Whiteley, H.D. Russman, T.D. Bishop, Porosity of building materials—a collection of published results, *Journal of the Oil and Colour Chemists Association* 60(4) (1977) 142-150.
- [47] G. Cultrone, A. Luque, E. Sebastián, Petrophysical and durability tests on sedimentary stones to evaluate their quality as building materials, *Quarterly Journal of Engineering Geology and Hydrogeology* 45(4) (2012) 415-422.
- [48] M. Arandigoyen, J.P. Bernal, M.B. López, J.I. Alvarez, Lime-pastes with different kneading water: pore structure and capillary porosity, *Applied Surface Science* 252(5) (2005) 1449-1459.
- [49] R.M. Lawrence, T.J. Mays, S.P. Rigby, P. Walker, D. D'Ayala, Effects of carbonation on the pore structure of non-hydraulic lime mortars, *Cement and Concrete Research* 37(7) (2007) 1059-1069.
- [50] G.W. Scherer, Theory of Drying, *Journal of the American Ceramic Society* 73(1) (1990) 3-14.
- [51] K. Beck, M. Al-Mukhtar, O. Rozenbaum, M. Rautureau, Characterization, water transfer properties and deterioration in tuffeau: building material in the Loire valley-France, *Building and Environment* 38(9) (2003) 1151-1162.
- [52] A. Arizzi, G. Cultrone, The water transfer properties and drying shrinkage of aerial lime-based mortars: An assessment of their quality as repair rendering materials, *Environmental Earth Sciences* 71(4) (2014) 1699-1710.
- [53] V.M. Malhotra, N.J. Carino, *Handbook on nondestructive testing of concrete*, 2004.
- [54] J.H. Schön, *Physical properties of rocks: fundamentals and principles of petrophysics. Handbook of geophysical exploration. Section I, Seismic exploration*, Pergamon, Oxford, 1996.
- [55] D.G. Aggelis, T.P. Philippidis, Ultrasonic wave dispersion and attenuation in fresh mortar, *Ndt & E International* 37(8) (2004) 617-631.
- [56] T.P. Philippidis, D.G. Aggelis, Experimental study of wave dispersion and attenuation in concrete, *Ultrasonics* 43(7) (2005) 584-595.
- [57] A. Arizzi, J. Martínez-Martínez, G. Cultrone, Ultrasonic wave propagation through lime mortars: An alternative and non-destructive tool for textural characterization, *Materials and Structures/Materiaux et Constructions* 46(8) (2013) 1321-1335.
- [58] C. Hall, W.D. Hoff, *Water transport in brick, stone and concrete*, Taylor & Francis, London, 2002.
- [59] D. Benavente, J. Martínez-Martínez, P. Jáuregui, M.A. Rodríguez, M.G. del Cura, Assessment of the strength of building rocks using signal processing procedures, *Construction and Building Materials* 20(8) (2006) 562-568.
- [60] A. López, G.A. Guzmán, A.R. Di Sarli, Color stability in mortars and concretes. Part 1: Study on architectural mortars, *Construction and Building Materials* 120 (2016) 617-622.
- [61] AGN, Royal and General Archive of Navarre, Rena Papers, Box 33080, 1517.
- [62] AGN, Royal and General Archive of Navarre, Rena Papers, Box 27, N.14, 1521.
- [63] M.C. Peel, B.L. Finlayson, T.A. McMahon, Updated world map of the Köppen-Geiger climate classification, *Hydrology and Earth System Sciences* 11(5) (2007) 1633-1644.
- [64] AEMET, *Iberian Climate Atlas*, Agencia Estatal de Meteorología (España) and Instituto de Meteorología (Portugal), Madrid, Spain, 2011.
- [65] Arizkun. Available on line:
<http://meteo.navarra.es/climatologia/selfichaclima.cfm?IDEstacion=66&tipo=MAN> (accessed on 23 January 2020). (Accessed accessed on 23 January 2020).
- [66] Gorramendi. Available online:
http://meteo.navarra.es/climatologia/fichasclimaticasaut_estacion.cfm?IDestacion=25 (accessed on 23 January 2020). (Accessed 23 January 2020).
- [67] D. Langmuir, *Aqueous Environmental Geochemistry*, Prentice Hall, Upper Saddle River, NJ., 1997.
- [68] G.W. Scherer, Crystallization in pores, *Cement and Concrete Research* 29(8) (1999) 1347-1358.
- [69] O. Coussy, Deformation and stress from in-pore drying-induced crystallization of salt, *Journal of the Mechanics and Physics of Solids* 54 (2006) 1517-1547.
- [70] J. Marchand, R. Pleau, R. Gagné, Deterioration of concrete due to freezing and thawing, in: J. Skalny, S. Mindess (Eds.), *Materials Science of Concrete IV*, American Ceramic Society, Westerville, OH, 1995, pp. 283-354.

APPENDIX III

Characterization of Historical Lime Mortars: An approach to Technological Knowledge

APPENDIX III.1

Multi-analytical approach for chemical-mineralogical characterization of reaction rims in the lime mortars from Amaiur Castle (Navarre, Spain)

Graciela Ponce-Antón, Maria Cruz Zuluaga, Luis Angel Ortega, Juantxo Agirre Mauleon

Microchemical Journal 2020; 152:104303

Article Metrics

✓ Journal Citation Reports

Citations: 0

Impact Factor

2018	5 Years
3.206	2.993

JCR® Rank	Classification	Quartile	Percentile
Chemistry Analytical	20 of 84	Q1	76.786

✓ Scopus

Citations: 1

CiteScore 2018	3.14
SJR 2018	0.739
SNIP 2018	1.195

CiteScore Rank	Classification	Percentile
Chemistry (Spectroscopy)	16 of 69	77
Chemistry (Analytical Chemistry)	29 of 109	73

✓ Google Academic

Citations: 2



Contents lists available at ScienceDirect

Microchemical Journal

journal homepage: www.elsevier.com/locate/microc

Multi-analytical approach for chemical-mineralogical characterization of reaction rims in the lime mortars from Amaiur Castle (Navarre, Spain)

Graciela Ponce-Antón^{a,*}, Maria Cruz Zuluaga^a, Luis Angel Ortega^a, Juantxo Agirre Mauleon^b^a Department of Mineralogy and Petrology, Science and Technology Faculty, University of the Basque Country (UPV/EHU), Spain^b Aranzadi Society of Sciences, Spain

ARTICLE INFO

Keywords:

Reaction rim
Dedolomitization
Lime mortar
Hydroxalcite
Hot-mixed mortars

ABSTRACT

This work presents a chemical-mineralogical study of archaeological lime mortars from Amaiur Castle (Navarre, Spain) dated between the 14th and 17th centuries. The study focuses on the analysis of the reaction zone observed around the dolomitic aggregates of lime mortars by means of optical microscopy, scanning electron microscopy with X-ray microanalysis, micro-Raman spectroscopy and X-ray diffraction. Multi-analytical analysis show that the reaction zone is composed of two reaction rims and a halo formed as result of the dedolomitization of dolomitic mortar aggregates in a strongly alkaline medium. The mineralogical results suggest mortars cured at around 60 °C, pointing to a traditional hot-mixing manufacture method.

1. Introduction

Mortars are artificial materials composed by a mixture of inorganic binder, aggregates and some organic or inorganic additives that form a bonding material in the masonry. In basic mortar manufacture the calcium carbonate (CaCO₃) of the limestone used as raw material is heated in the calcination process to produce quicklime (CaO). In the slaking process water is added to calcium oxide to produce portlandite (Ca(OH)₂). The slaked lime and aggregates are mixed with water to make more workable putty. In the carbonation process the calcium hydroxide in the putty reacts with atmospheric carbon dioxide (CO₂) to form calcium carbonate again.

Nevertheless, during mortar manufacture other reactions could take place between the different mortar components [1,2]. Alkali-aggregate reactions (AAR) can take place during manufacture of mortar. AAR is a general term referring to all reactions occurring between binder alkalis and aggregates. AAR occurs when, in the highly alkaline medium, some aggregate mineral phases react with the alkaline hydroxides present in the hydrated lime putty. The nature, size and amount of aggregates, alkali contents, temperature and pH determine the AAR reaction speed [3]. Nevertheless, the scientific community still does not fully understand the mechanisms involved [3]. Intensive research has been carried out on AAR since it was first reported in the 1940s [4–12]. Alkali-silica reaction (ASR) and alkali-carbonate reaction (ACR) have been described within the AAR [13]. ASR involves the reaction of silica present in the siliceous limestone aggregates with the alkalis present in the binder resulting in an expansive gel. However, ACR takes place when

argillaceous dolomitic limestone aggregates react with the binder alkali [3].

Several authors have described ACR in mortars and concretes since it was first recognized in the 1950s [5,14–19]. Within ACR, a dedolomitization reaction could take place. Dedolomitization involves the partial dissolution of dolomite forming a reaction zone around the edge of dolomitic aggregates [20,21]. Formation of reaction zones surrounding mortar aggregates has been described by several authors [18,22–28].

The aim of this work was to study the reaction zone in the dolomitic aggregates of Amaiur Castle (Navarre) lime mortars, and the alkali-aggregate reactions involved. A multi-analytical study was carried out for chemical, mineralogical and textural characterization by means of optical microscopy, Raman spectroscopy, X-ray diffraction and scanning electron microscopy coupled with electron-dispersive spectroscopy. In this way, the study is able to contribute knowledge of the manufacturing process of lime mortars between the 14th and 17th centuries.

2. Materials and methods

2.1. Samples

Archaeological lime mortar samples from Amaiur Castle (Navarre Spain) were analyzed in order to study the reaction zone in dolomitic aggregates. The mortars belong to structures built in different periods: a wall between the 14th and 15th centuries, a 16th century bastion and fillings, and a second bastion dated in the 17th century (Fig. 1).

* Corresponding author.

<https://doi.org/10.1016/j.microc.2019.104303>

Received 13 May 2019; Received in revised form 3 October 2019; Accepted 3 October 2019

Available online 19 October 2019

0026-265X/ © 2019 Elsevier B.V. All rights reserved.

2.2. Digital and optical microscopy

Macroscopic high-resolution analysis was carried out on the polished surface of bulk mortar using a Dino-Lite Premier AM7013MZT digital handheld microscope equipped with a Microtouch II sensor with adjustable polarizer with up to 200× magnification working distance. Measurement and calibration were made with DinoCapture 2.0 software.

Petrographic studies were performed on polished thin-sections by polarizing microscopy using a Nikon Eclipse LV100POL microscope equipped with a DS F-11 digital camera and DS L2 camera control unit. Sample microtextural characteristics were analyzed using both transmitted and reflected polarized light modes.

2.3. Raman microspectroscopy

Micro-Raman analyses were performed by means of Renishaw inVia confocal microRaman spectrometer (Renishaw, Gloucestershire, UK) coupled to a DMLM Leica microscope provided with 5×, 20×, 50× and 100× long working distance lenses using 785 nm (NIR) excitation laser. Laser was set at low power (not more than 1 mW at the sample) in order to avoid thermal photodecomposition. Data acquisition was carried out using Renishaw's WireTM 3.2 software package. The interpretation of Raman results was carried out by comparison of acquired Raman spectra with Raman spectra of pure standard compounds collected in the e-VISNICH dispersive Raman database. In order to obtain Raman mapping, the StreamLine technique was used. Spectra were acquired between 1000 and 1120 cm⁻¹ with a 1 cm⁻¹ resolution with a 50× objective and a good signal-noise ratio. Internal calibrations and daily calibration with a silicon chip ensured measurement quality.

2.4. X-ray powder diffraction

The X-ray diffraction (XRD) analysis was performed on a powder polycrystalline sample by means of Philips X'Pert diffractometer (Malvern PANalytical, Almelo, The Netherlands) equipped with a monochromatic Cu-ka1 X-radiation. The operating conditions were 40 kV and 20 mA. A continuous scan in the range from 5° to 70° 2θ was performed for the data collection, at an acquisition rate of 0.02° per second. Mineral phase identification was made by X'Pert HighScore Plus 3.0 software by PANalytical (Malvern PANalytical, Almelo, The Netherlands) using the experimental patterns of ICDD and ICSD diffraction databases.

2.5. Scanning electron microscopy

Scanning electron microscopy and energy-dispersive X-ray spectroscopic (SEM-EDX) analyses were carried out on polished thin sections by means of a JEOL JSM-7000F Schottky-type field emission scanning electron microscope (JEOL, Tokyo, Japan) equipped with an INCA EDX X-sight Series Si (Li) Oxford pentaFET microanalysis system. The back-scattered electron (BSE) resolution was 3 nm at 15 kV and 10 mm working distance. Energy dispersive X-ray spectroscopic mapping measurements were performed using an EVO 40 scanning electron microscope (Carl Zeiss STS, Germany) coupled to an X-Max energy-dispersive X-ray spectrometer (Oxford Instruments, Abingdon, Oxfordshire, UK). The EDX analyses were carried out using a working distance of 8–10 mm, an I Probe of 400 pA, an acceleration potential of 20 kV and 10 scans. Samples were carbon-coated to eliminate charging effects. SEM-EDS measurements were carried out to determine the elemental distribution images in the cross-section of the reaction zone.

The XRD, SEM-EDX and Raman microspectroscopy analyses were performed in the Materials and Surface Unit and the Raman-LASPEA laboratory at the Advanced Research Facilities (SGIker) of the University of the Basque Country (UPV/EHU).

3. Results

3.1. Digital and optical microscopy

Carbonated aggregates of mortar larger than 2 cm in size showed a pronounced reaction zone visible even at macroscopic scale. Digital microscopy observations of bulk mortar polished surfaces enabled better observation of large-size aggregate reaction zones (Fig. 2a).

Observed macroscopic features were improved by the petrographic study allowing the observation of the mortar microtextural characteristics. Microscopically, mortars showed heterogeneous texture. Embedded in a micritic calcite matrix, the carbonated aggregates consisted of angular fine-grained dolostone fragments with vuggy porosity (Fig. 2b and c). Observed dolostones are secondary dolostones formed by the geological process of dolomitization in which the replacement of CaCO₃ by CaMg(CO₃)₂ take place [29]. Besides, the petrographic study allowed a better observation of the reaction zone of dolomitic aggregates (Fig. 2d).

3.2. Raman microspectroscopy

Lime mortars were analyzed by Raman spectroscopy [30,31] and measurements were performed on a polished surface (Fig. 3a). Fig. 3b shows the recorded Raman spectra with the highest intensities of the main calcite and dolomite bands; 1087 cm⁻¹ and 1098 cm⁻¹, respectively [32,33]. The main bands of calcite and dolomite overlap due to the relative shift of only 11 cm⁻¹, but the 1 cm⁻¹ spectral resolution used has allowed the two intensities to be differentiated and mapped independently. Dolomite was detected in the unaltered aggregate and in some zones within the binder (Fig. 3c) whereas calcite was mainly found in the mortar binder and in the reaction zone, and scarcely within the unaltered aggregate (Fig. 3d).

3.3. X-ray diffraction

XRD analyses identified different mineral phases in the mortar (Fig. 4). Aggregates are mainly composed of dolomite [CaMg(CO₃)₂] and traces of calcite [CaCO₃] which is in accordance with the petrographic studies (Fig. 4a). To characterize binder, a < 2 μm fraction was extracted following the procedure described by Ortega et al. [34] and Ponce Anton et al. [2]. Magnesium calcite [(Ca,Mg)CO₃] was identified as the principal component of mortar binder but hydrotalcite [Mg₆Al₂(CO₃)(OH)₁₆·4(H₂O)] and pyroaurite [Mg₆Fe₂(CO₃)(OH)₁₆·4H₂O] phases were also present in minor amounts (Fig. 4b). Hydrotalcite and pyroaurite belong to layered double hydroxide phases (LDHs) characterized by a brucite-like structure occurring as clay-sized crystals with a general formula [M_(1-x)M³⁺_x(OH)₂]^{x+}(Aⁿ⁻)_{x/n}·yH₂O where M²⁺ and M³⁺ are di- and trivalent cations, and Aⁿ⁻ is a charge-balancing anion [35–39].

The XRD pattern shows asymmetric and broad peaks at ~11° 2θ and ~23° 2θ indicating low crystallinity and also suggesting a probable overlapping of reflection. Hydrotalcite was identified by the characteristic basal reflections d₀₀₃ = 7.61 Å at 11.63° 2θ and d₀₀₆ = 3.81 Å at 23.33° 2θ; whereas pyroaurite was identified according to d₀₀₃ = 7.7 Å at 11.38° 2θ and d₀₀₆ = 3.92 Å at 22.67° 2θ. In addition, the reflections at 23.15° 2θ correspond to the characteristic basal plane d₀₁₂ = 3.84 Å of calcite. XRD results agree with the petrographic and Raman studies.

3.4. Scanning electron microscopy

Scanning electron microscopy results on polished thin sections showed a sequence of different reaction zones (~100 μm width) within coarse aggregate (Figs. 5, 6a, 7a and 8a.). Several sectors can be distinguished in the reaction zone according to textural characteristics. The reaction sectors are distributed as follows: an inner narrow reaction



Fig. 1. Geographic location of Amaiur Castle (Navarre, Spain). Studied samples came from the highlighted structures on the archaeological plan. In blue, 14th–15th centuries wall; in green 16th century bastion; and in reddish 17th century bastion.

rim in contact with the unaltered dolomitic aggregate, a thicker reaction rim in the outer margin of the aggregate and a halo within the binder in contact with the outer part of the aggregate (Fig. 5). A thicker reaction rim is characterized by a pseudomorphic texture composed of dark and bright spots. Expansion cracks were not observed.

EDX analyses were performed in order to characterize reaction sectors. Table 1 summarizes the major element semi-quantitative results. The reaction zone is mainly composed of MgO and CaO but MgO concentration decreases from the inner to outer zones of the aggregate while the CaO concentration increases. MgO content ranges between 33.5 to 1.2% whereas CaO varies from 65.5 to 98% showing a pronounced CaO enrichment in the reaction halo. Na₂O, P₂O₅, TiO₂ and MnO appear in minor amounts (<0.2%). The SiO₂ (15.4%), Al₂O₃ (1.1%), FeO (0.8%) and K₂O (0.3%) contents increase notably in the inner narrow rim. However, the highest FeO contents are in the thicker reaction rim (1.6%).

Elemental maps were produced in order to observe element distribution in the reaction sectors. Elemental mapping shows carbon, oxygen, magnesium, calcium, aluminum and silicon spatial distribution

in the aggregate, aggregate-binder interface (reaction zone) and binder (Figs. 6 and 7). In the aggregate/binder interface C and Ca concentrations increase (Figs. 6b and 7b, c) whereas O and Mg concentration decreases (Figs. 6c, d and 7d, e). The whitish halo clearly stands out owing to the enrichment in Ca whereas the maximum concentration of Mg is present in the aggregates (Fig. 7c and e). Although Al and Si concentrations are very low, the Si is slightly higher in the inner narrow rim (Fig. 7f and g). However, by decreasing the Si resolution on the elemental distribution map, both pixel size and intensity increase, allowing the inner narrow rim to be distinguished more clearly (Fig. 7h). Fig. 8 shows elemental mapping semi-quantitative results expressed as absolute wt%. C and Ca show the highest concentrations (83% and 71%, respectively) while O and Mg display lower concentrations (58% and 21%, respectively). The Si and Al concentration is less than 12%. When semi-quantitative values are expressed as absolute wt% and are less than 25% the element distribution is not clearly observed (Fig. 8b, c, d, e). Therefore, for a better observation of the element distribution, relative wt% values were used for Mg, Al and Si elements (Fig. 8e, f, and g). Al and Mg presence in elemental mapping of binder verifies the

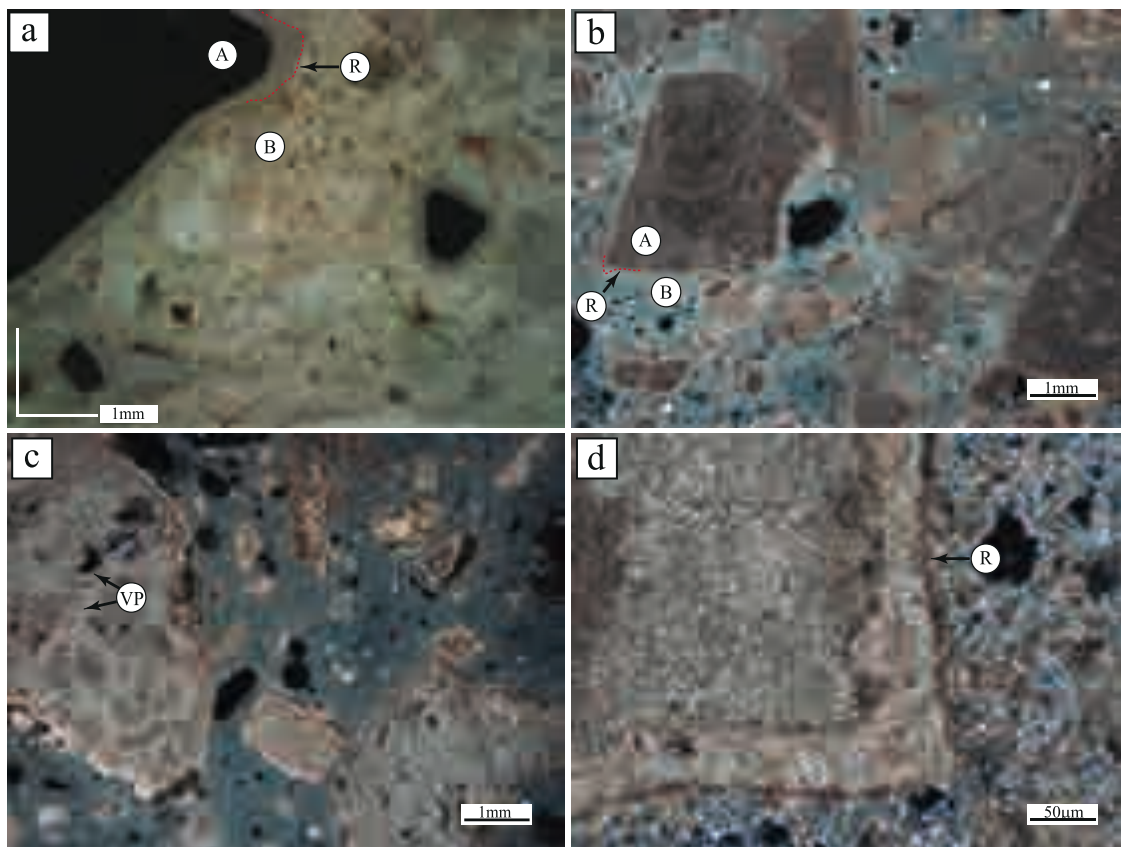


Fig. 2. Archaeological mortar samples showing reaction zones at the edge of the dolomitic aggregate: (a) stereomicroscopic image of the reaction zone; (b) mortar photomicrograph; (c) mortar photomicrograph showing vuggy porosity; (d) detail of the aggregate reaction zone. A = aggregate, B = binder, R = rim, VP = vuggy porosity.

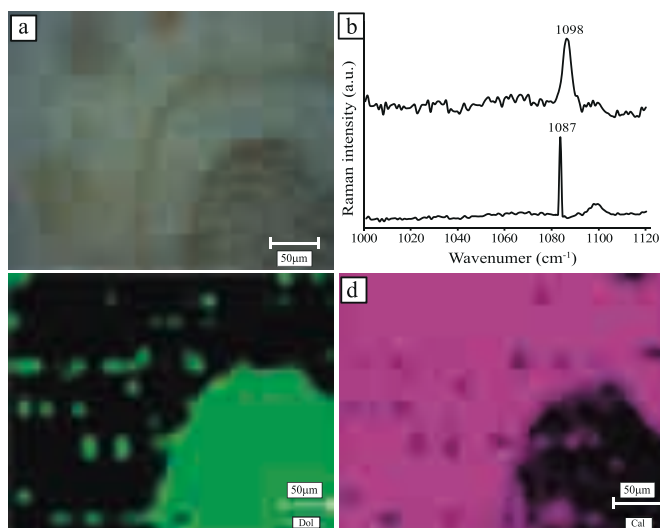


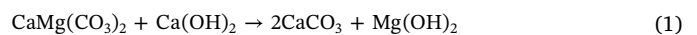
Fig. 3. Optical and chemical results of aggregate edge Raman analysis: (a) optical microscopy image; (b) Raman spectra of the mapped areas with the highest intensities of the 1098 cm^{-1} dolomite band and the 1087 cm^{-1} calcite band; (c) Raman microscopy map showing dolomite distribution; (d) Raman microscopy map showing calcite distribution.

LDHs presence as identified by XRD analysis. Hexagonal crystals greater than $1\text{ }\mu\text{m}$ within the binder fraction also verify the LDHs presence (Fig. 9a and b). Mg, Al and Fe obtained by EDX (Fig. 9c) suggest the presence of hydrocalcite and pyroaurite, as was identified by XRD (Fig. 4). The silica content can be attributed to microcrystalline quartz.

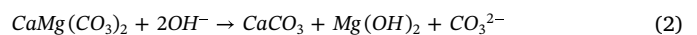
4. Discussion

Chemical-mineralogical results show rims and halo formation with a marked Mg loss and Ca increase pointing to chemical reactions due to dedolomitization of dolomitic aggregates (Figs. 3c, 6d, 7e, 8e and Table 1).

Several authors have studied the dedolomitization reaction mechanism [20,21,40,41] and also the development of reaction zones around dolomite aggregates [18,22–28]. Two elementary reactions occur in the dedolomitization process: the first within the aggregate giving rise to a reaction rim (Eq. (1) and Eq. (2)) and the second within the binder forming a carbonate halo (Eq. (3)). Reaction rim formation takes place as follows:



Dolomite [$\text{CaMg}(\text{CO}_3)_2$] reacts with portlandite [$\text{Ca}(\text{OH})_2$] to generate calcite [CaCO_3] and brucite [$\text{Mg}(\text{OH})_2$]. Once calcite and brucite precipitate, a reaction rim on the edge of the dolomite aggregate is formed (Fig. 5). Dissolution of dolomite is influenced by temperature and alkaline medium [20,21]. Unlike limestone, dolostones are unstable in alkaline environments [13]. Thus, in alkaline environments, dolomite reacts with hydroxyl ions [OH^-] to form calcite, brucite and carbonate ions [CO_3^{2-}] as follows:



Carbonate halos are formed within the binder in contact with the outer part of the dolomitic aggregate by the carbonation of lime putty. A halo is not formed by the putty carbonation bias to the reaction with atmospheric carbon dioxide but due to the reaction between dolomitic aggregate and alkalis leading to *in situ* calcite precipitation [11]. For the halo formation, the CO_3^{2-} liberated by dedolomitization reaction

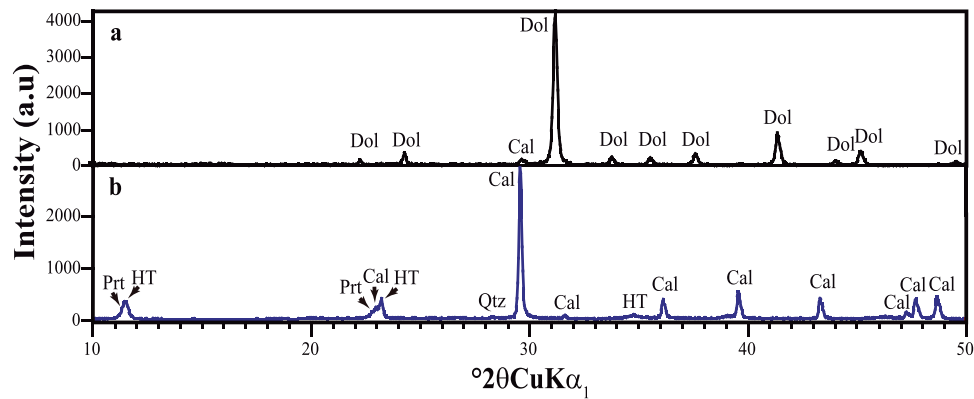


Fig. 4. X-ray diffraction patterns of mortar components: (a) mortar dolomitic aggregate spectrum; (b) mortar binder fraction less than 2 μm spectrum. Dol = dolomite, Cal = calcite, Qtz = quartz, HT = hydrotalcite, Prt = pyroaurite.

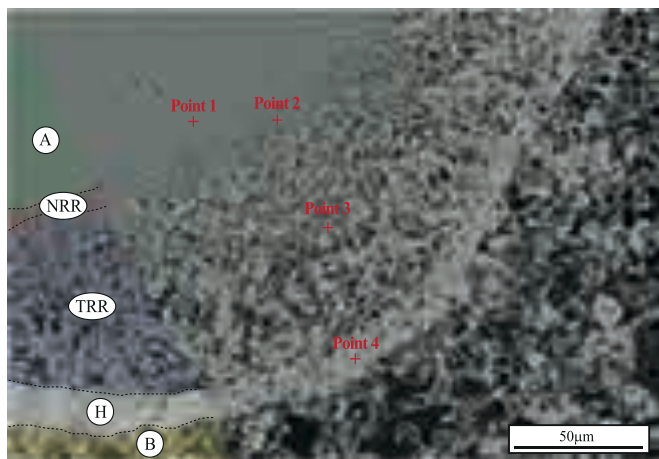


Fig. 5. SEM-BSE image of lime mortar polished thin-section. Different reaction zones are observed. A = aggregate, B = binder, NRR = narrow reaction rim, TRR = thick reaction rim, H = halo. .

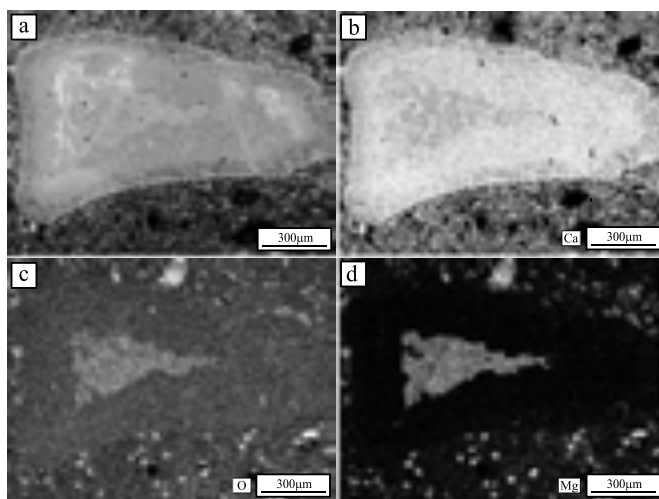
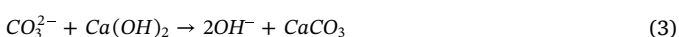


Fig. 6. SEM-BSE image and elemental mapping of reaction zone of dolomitic aggregate: (a) BSE image; (b) SEM-EDS distribution image for calcium; (c) SEM-EDS distribution image for oxygen; (d) SEM-EDS distribution image for magnesium.

migrates into the lime putty and reacts with portlandite to produce calcite and OH^- [42] as follows:



Reaction rims and carbonate halo formation do not produce expansion but favor the high alkaline environment [18,19]. Besides, water dissociates in a reversible reaction in which both hydrogen ions (H^+) and OH^- are generated. With a higher pH, faster dedolomitization reactions take place [26,42].

Although calcite and brucite are formed as dedolomitization products (Eq. (1) and Eq. (2)), brucite could not be identified by XRD since the small size of the reaction rim did not allow the extraction of a representative powder sample without aggregate and matrix contamination. However, dark and bright spots observed in BSE at the thicker reaction rim (Fig. 5) could be identified as brucite and calcite, respectively, forming a pseudomorphic texture [18]. Moreover, the elemental mapping of Ca and Mg concentrations also suggests the presence of brucite since Ca concentration decreases in dark spots while Mg concentration increases (Figs. 7c and 8c, f). EDX analysis shows Ca enrichment in the halo in accordance with Eq. (3) (Table 1 and Fig. 7c).

The siliceous narrow rim can be explained as result of an alkali-silicate reaction (ASSR) (Figs. 5 and 7g, h). The ASSR is a specific type of alkali-silica reaction (ASR) that occurs more slowly [3]. In an ASR, silica in siliceous aggregates reacts with alkali solution forming an unstable silica gel (ASR-gel) which absorbs water and expands causing the formation of cracks [6,19]. However, when the phyllosilicates within aggregates react with the alkaline solution, ASSR occurs resulting in small amount of silicate gel (ASSR-gel) [3,18,43]. Phyllosilicates appear scattered in dolostones as impurities and in contact with an alkaline medium react and break down [13]. Unlike ASR-gel composed of alkalis, calcium, silica and water, the ASSR-gel is composed of alkalis (potassium), silica, aluminum and iron [44].

To form the siliceous narrow rim, the ASSR-gel reacts with brucite to form non-expansive Mg-silicate-gel that in turn reacts with brucite to form “chlorite-like” phases [19,23,25]. Neither phyllosilicates from the dolomitic aggregate nor reaction products in the siliceous narrow rim could be identified by XRD due to the scarce amount of impurities in aggregates and the small size of the rim, respectively. However, the Si, Al, Fe and K contents of the siliceous narrow rim (Table 1) suggest the presence of “chlorite-like” phases in the rim as well as phyllosilicates in the dolomitic aggregate. According to chemical results, chlorite $[(\text{Mg},\text{Fe})_5\text{Al}(\text{Si}_3\text{Al})\text{O}_{10}(\text{OH})_8]$ and illite $[\text{K}(\text{Al},\text{Mg},\text{Fe})_2(\text{Si},\text{Al})_4\text{O}_{10}(\text{OH})_2]$ are the expected phyllosilicates in dolostone aggregates.

Higher Si concentration in the narrow rim can be related to the presence of magnesium silicate hydrate (M-S-H) phases as reaction products. M-S-H phases (short for $(\text{MgO})_x-(\text{SiO}_2)_y-(\text{H}_2\text{O})_z$) show a layered structure similar to phyllosilicates [45–48]. The crystalline structure of M-S-H synthetic phases has been related to the poorly-crystalline trioctahedral (2:1 or 1:1) phyllosilicates crystalline structures [49] and have also been associated with sepiolite $[\text{Mg}_4\text{Si}_6\text{O}_{15}(\text{OH})_2 \cdot 6\text{H}_2\text{O}]$ [45]. Like phyllosilicates, M-S-H phases are stable in an alkaline environment at pH up to 10 [46,49–51].

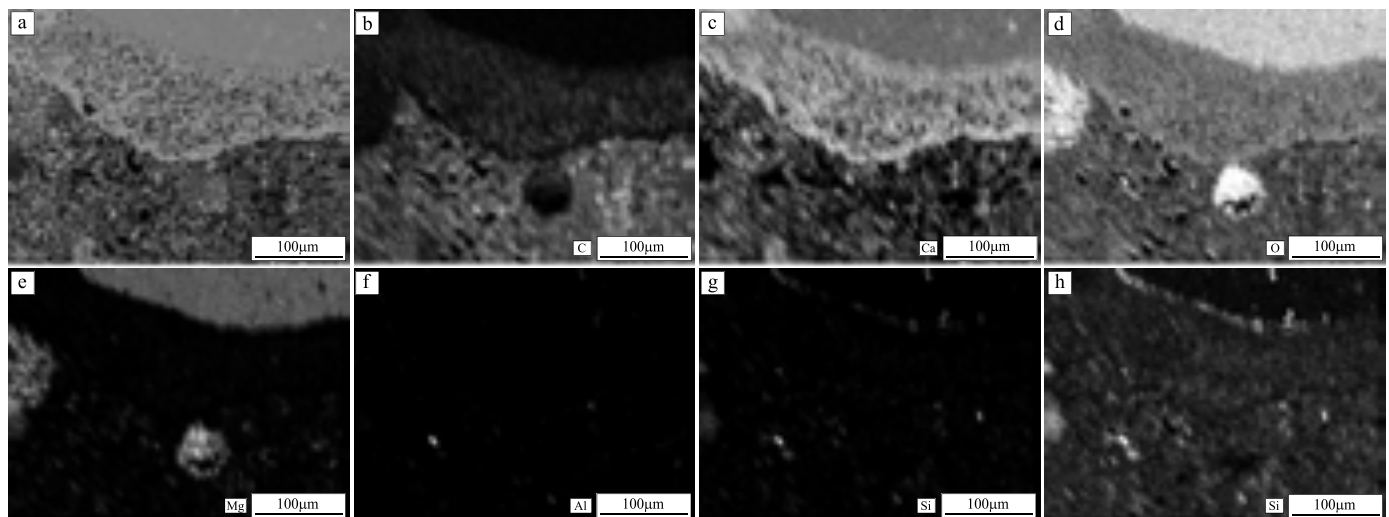


Fig. 7. Detailed SEM-BSE image and elemental mapping of reaction zone: (a) BSE image; (b) SEM-EDS distribution image for carbon; (c) SEM-EDS distribution image for calcium; (d) SEM-EDS distribution image for oxygen; (e) SEM-EDS distribution image for magnesium; (f) SEM-EDS distribution image for aluminium; (g) SEM-EDS distribution image for silicon; (h) SEM-EDS higher magnification image for silicon distribution.

Amorphous M-S-H formation have been also identified during the hydration of binder materials with a high content in MgO [45]. However, it was not possible to confirm the presence of M-S-H phases in the studied mortars.

Hydrotalcite rims have also been described surrounding dolomitic aggregates [19,52,53]. In view of the results of the elemental mapping, the absence of aluminum in the reaction zone does not indicate the presence of hydrotalcite. However, elemental mapping shows Al and Mg concentrations in the binder suggesting a presence of hydrotalcite in the binder (Fig. 8f, g). In fact, hydrotalcite and pyroaurite were also identified in the binder by XRD (Fig. 4). Hexagonal plate-like crystals characteristic of hydrotalcite and pyroaurite LDH phases were observed by SEM, confirming the elemental mapping and XRD results (Fig. 9a and b). Additionally, the silica in the binder (Fig. 7g, h and 9c) can proceed from phyllosilicate breakdown [26] leading to microcrystalline quartz, which was the only silicate phase identified by XRD (Fig. 4b).

Hydrotalcite could be formed in the mortar manufacture during the slaking process [2]. The $\text{Mg}(\text{OH})_2$ and CO_3^{2-} released from

dedolomitization reactions (Eqs. (1) and (2)) and the aluminate ions $[\text{Al}(\text{OH})_4]^-$ released from phyllosilicate breakdown can migrate into the lime putty and react forming hydrotalcite [26,52,54]. Besides, the lime could also contain MgO and Al_2O_3 when impure limestone and/or partially dolomitized limestones have been used in lime production, and when they rehydrate and react they form hydrotalcite [2,55–57]. Furthermore, the LDHs are characterized by a high capacity to capture CO_3^{2-} anions due to their ion-exchange properties [35]. Besides, the high CO_3^{2-} affinity of LDHs makes it possible to incorporate the dead carbon from the CO_3^{2-} of aggregates [35,58]. Therefore, the hydrotalcite LDH phase constitutes a potentially contaminating mineral phase in radiocarbon dating of the mortar binder [2].

Hydrated calcium aluminate phases (AFm) with general formula $[\text{Ca}_2(\text{Al,Fe})(\text{OH})_6] \cdot \text{X} \cdot x\text{H}_2\text{O}$ where X is a monovalent or half of a divalent anion [52,59] were not identified in studied mortars since the hydrotalcite mineral phase is thermodynamically more stable [60]. The formation of hydrotalcite has been described in dolomitic mortars cured at 60 °C [52,53]. The presence of hydrotalcite in the studied mortars

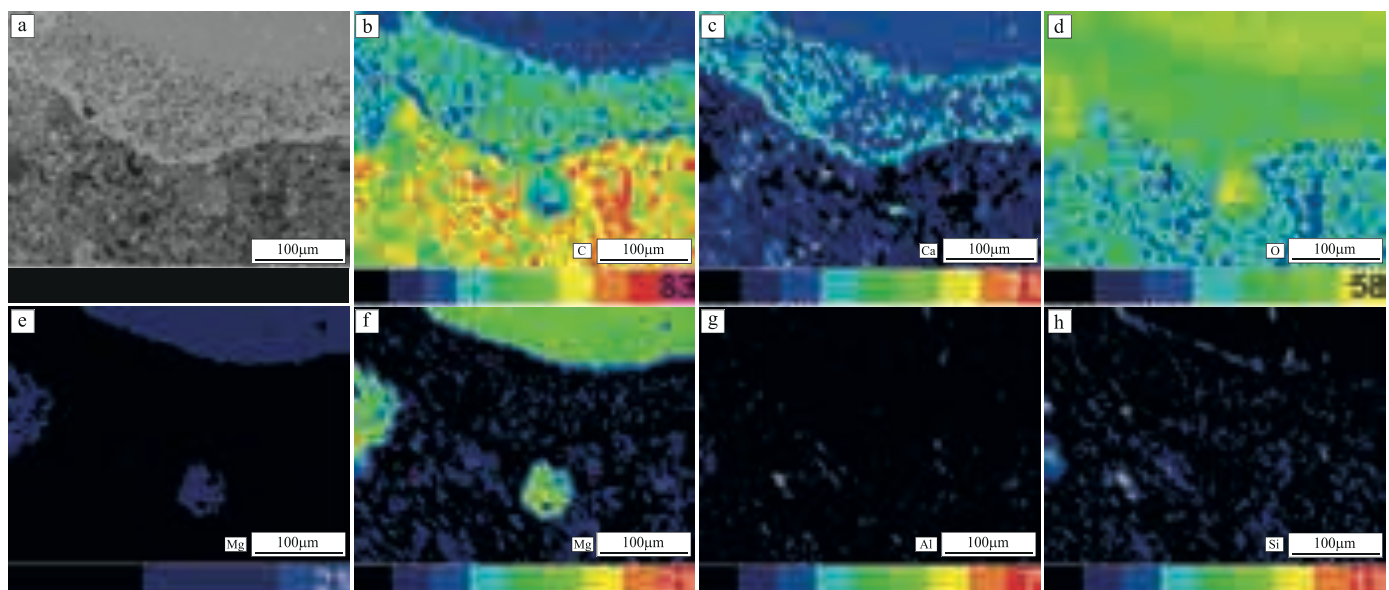
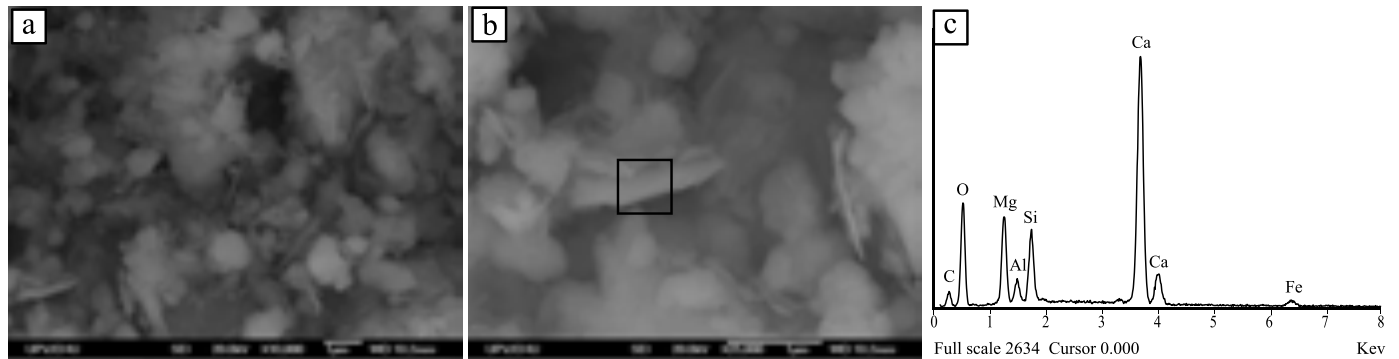


Fig. 8. Detailed SEM-BSE image and semiquantitative elemental mapping of reaction zone with percentages indicated on a colour scale: (a) SEM-BSE image; (b)–(e) absolute wt% for carbon, calcium, oxygen and magnesium, respectively; (f)–(h) relative wt% of magnesium, aluminium and silicon, respectively.

Table 1

Chemical analysis results obtained by EDX of major elements expressed as oxides in wt%.

Analysis Zone	Na ₂ O	MgO	CaO	Al ₂ O ₃	SiO ₂	FeO	K ₂ O	P ₂ O ₅	TiO ₂	MnO
Point 1 - Aggregate	0.10	33.51	65.45		0.20	0.38	0.02	0.06	0.09	0.19
Point 2 - Narrow rim		18.58	63.55	1.11	15.40	0.83	0.29	0.04	0.04	0.17
Point 3 - Thicker rim		4.14	91.44	0.26	2.08	1.57	0.09	0.17	0.17	0.09
Point 4 - Halo	0.12	1.19	98.03	0.03	0.42		0.06	0.01	0.14	

**Fig. 9.** Mortar binder SEM-EDX results: (a) and (b) Secondary electron SEM images showing LDHs hexagonal crystals; (c) EDX spectrum of the marked area.

points to mortars cured at around 60 °C, suggesting the traditional hot-mixing method in mortar manufacture. In the hot-mixing method, quicklime (CaO) is mixed with the aggregates and slaked to use it later when it is still hot [61,62]. Quicklime is highly reactive in contact with water resulting in a strong exothermic reaction [63] leading to temperatures that may reach 200 °C when it is slaked with a little water and drop below 100 °C as more water is added until slaking finishes at around 58 °C [62]. Therefore, the hot-mixing method leads to both portlandite and hydroxyl ion formation during the slaking (Eq. (4) and Eq. (5), respectively) favoring the dedolomitization reactions according to Eq. (1) and Eq. (2), respectively.



Hot-mixed mortar production was relatively cheap and quick to manufacture since quicklime could be used shortly after it was produced, thus also reducing storage problems [63,64]. Hot-mixed mortars had excellent workability and were commonly used for foundation works and core filling principally in cold-weather or winter work [61,63]. These characteristics would be advantageous in the typically cold and wet climate conditions in the region where Amaiur Castle is located [65]. Besides, the cheap and quick hot-mixed mortar manufacture would be appropriate in the construction and modification of Amaiur Castle structures in conflictive periods.

5. Conclusions

A combination of optical microscopy, micro-Raman spectroscopy, X-ray diffraction and scanning electron microscopy with X-ray micro-analysis was able to characterize the reaction zone of dolomitic aggregates in Amaiur Castle historic mortars.

Chemical, mineralogical and textural variations in the dolomitic aggregate reaction zone show the presence of two reaction rims within the aggregate and a halo within the binder.

Rims and halo were formed due to an alkali-aggregate reaction (AAR) leading to dedolomitization of dolomitic mortar aggregates in a strongly alkaline medium, although an alkali silicate reaction (ASSR) was also involved.

Neither AFm nor M-S-H phases were detected in the studied mortar lime binder but hydrotalcite and pyroaurite were identified.

The presence of hydrotalcite and pyroaurite advises against the use of lime binders from Amaiur Castle for radiocarbon dating.

Mortar chemical and mineralogical characteristics point to the use of the traditional hot-mixing method in the mortar manufacture at Amaiur Castle.

Declaration of Competing Interest

Authors declare that they have no conflict of interest.

Acknowledgments

The authors would like to thank the anonymous referee for their comments and suggestions on the manuscript. The study was supported by the IT1193-19 Research Group of the Basque Country Government. G.P.-A. also acknowledges a PhD research grant from the Basque Country Government [PRE-2015-1-0235]. The authors would like to thank Peter Smith for reviewing the use of English in the manuscript.

References

- [1] D.T. Beruto, R. Vecchiattini, M. Giordani, Solid products and rate-limiting step in the thermal half decomposition of natural dolomite in a CO₂ (g) atmosphere, *Thermochim. Acta* 405 (2003) 183–194.
- [2] G. Ponce-Antón, L.A. Ortega, M.C. Zuluaga, A. Alonso Olazabal, J.L. Solaun, Hydrotalcite and hydrocalumite in Mortar Binders from the Medieval Castle of Portilla (Álava, North Spain): accurate mineralogical control to achieve more reliable chronological ages, *Minerals* 8 (2018) 326.
- [3] J.M.M.da Fonseca, V.K.B. de Souza, D.G.C.da Silva, D.L.da Silva, E.C.B. Monteiro, Alkali-aggregate reaction: definition, influence and control, *Eng. Appl. Sci.* 3 (2018) 12.
- [4] T.E. Staton, Expansion of concrete through reaction between cement and aggregate, *Proc. Am. Soc. Civil Eng.* 66 (1940) 1781–1811.
- [5] J.E. Gillott, Alkali-aggregate reactions in concrete, *Eng. Geol.* 9 (1975) 303–326.
- [6] L.D. Glasser, N. Kataoka, The chemistry of 'alkali-aggregate' reaction, *Cem. Concr. Res.* 11 (1981) 1–9.
- [7] S. Diamond, Alkali aggregate reactions in concrete: an annotated bibliography 1939–1991, Document SHRP-C/UPW-92-601, Strategic Highway Research Program, National Research Council, Washington, DC, 1992.
- [8] E.J. Lee, H.M. Clowes, Alkali-Aggregate Reaction 1977-1992, A Definitive Bibliography, BCA Ref: CIS/B8, British Cement Association, Slough (later Crowthorne), U.K, 1992.
- [9] A.B. Poole, The alkali-silica reactions in concrete, in: S. NR (Ed.), *Introduction to Alkali Aggregate Reaction in Concrete*, Blackie & London, UK, 1992, pp. 1–28.
- [10] B. Fournier, M.-A. Bérubé, Alkali-aggregate reaction in concrete: a review of basic concepts and engineering implications, *Can. J. Civ. Eng.* 27 (2000) 167–191.
- [11] I. Sims, A. Poole, Alkali-aggregate reactivity, in: J. Newman, C. Ban Seng (Eds.),

- Advanced Concrete Technology – Concrete Properties, Elsevier, Oxford, U.K., 2003, pp. 1–37.
- [12] G.E. Blight, M.G. Alexander, Alkali-Aggregate Reaction and Structural Damage to Concrete: Engineering Assessment, Repair and Management, CRC Press, 2011.
- [13] F.H. Shrimmer, Progress in the Evaluation of Alkali-Aggregate Reaction in Concrete Construction in the Pacific Northwest 2209-K Geological Survey Bulletin, United States and Canada. U. S., 2005, p. 11.
- [14] E.G. Swenson, A reactive aggregate undetected by ASTM tests, ASTM Bull. 226 (1957) 48–51.
- [15] E.G. Swenson, J.E. Gillott, Characteristics of Kingston carbonate rock reaction, Highway Res. Board Bull. 275 (1960).
- [16] D.W. Hadley, Alkali reactivity of carbonate rocks-expansion and dedolomitization, Highway Research Board Proceedings, 40 1961.
- [17] M.-S. Tang, Z. Liu, Y.-N. Lu, S.-F. Han, Alkali-carbonate reaction and pH value, II Cemento 88 (1991) 141–150.
- [18] T. Katayama, How to identify carbonate rock reactions in concrete, Mater. Charact. 53 (2004) 85–104.
- [19] T. Katayama, The so-called alkali-carbonate reaction (ACR) — its mineralogical and geochemical details, with special reference to ASR, Cem. Concr. Res. 40 (2010) 643–675.
- [20] S. Galí, C. Ayora, P. Alfonso, E. Tauler, M. Labrador, Kinetics of dolomite–portlandite reaction: application to portland cement concrete, Cem. Concr. Res. 31 (2001) 933–939.
- [21] E. García, P. Alfonso, E. Tauler, S. Galí, Surface alteration of dolomite in dedolomitization reaction in alkaline media, Cem. Concr. Res. 33 (2003) 1449–1456.
- [22] R.E. Bisque, J. Lemish, Chemical characteristics of some carbonate aggregate as related to durability of concrete, Highway Research Board Bulletin (1958).
- [23] D.W. Hadley, Alkali reactivity of dolomitic carbonate rocks, Highway Research Record 45 (1964).
- [24] H.N. Walker, Reaction products in expansion test specimens of carbonate aggregate, Transp. Res. Rec. 525 (1974) 28–37.
- [25] A.B. Poole, P. Sotiropoulos, Reactions between dolomitic aggregate and alkali pore fluids in concrete, Q. J. Eng. Geol. Hydrogeol. 13 (1980) 281–287.
- [26] G.-L. Gan, P.G. Spry, A.M. Cody, Rim formation on iowa highway concrete dolomite aggregate: the effects of dedolomitization reactions, Environ. Eng. Geosci. (1996) 59–72 II.
- [27] T. Katayama, T. Drimalas, J.H. Ideker, B. Fournier, Rim-forming dolomitic aggregate in concrete structures in Saudi Arabia - is dedolomitization equal to the so-called alkali-carbonate reaction? 14th International Conference on Alkali Aggregate Reactions (ICAAR), Austin, Texas, 2012.
- [28] S. Kramar, V. Zalar, M. Urosevic, W. Körner, A. Mauko, B. Mirtič, J. Lux, A. Mladenović, Mineralogical and microstructural studies of mortars from the bath complex of the Roman villa rustica near Mošnje (Slovenia), Mater. Charact. 62 (2011) 1042–1057.
- [29] J.S. Boggs, Petrology of Sedimentary Rocks, second ed., Cambridge University Press, Cambridge, 2009.
- [30] S. Martínez-Ramírez, S. Sanchez-Cortes, J.V. Garcia-Ramos, C. Domingo, C. Fortes, M.T. Blanco-Varela, Micro-Raman spectroscopy applied to depth profiles of carbonates formed in lime mortar, Cem. Concr. Res. 33 (2003) 2063–2068.
- [31] T. Schmid, P. Dariz, Chemical imaging of historical mortars by Raman microscopy, Constr. Build. Mater. 114 (2016) 506–516.
- [32] J. Sun, Z. Wu, H. Cheng, Z. Zhang, R.L. Frost, A Raman spectroscopic comparison of calcite and dolomite, Spectrochim. Acta Part A 117 (2014) 158–162.
- [33] S. Gunasekaran, G. Anbalagan, S. Pandi, Raman and infrared spectra of carbonates of calcite structure, J. Raman Spectrosc. 37 (2006) 892–899.
- [34] L.A. Ortega, M.C. Zuluaga, A. Alonso-Olazabal, X. Murelaga, M. Insausti, A. Ibañez-Etxebarria, Historic lime-mortar 14C dating of Santa María la Real (Zarautz, northern Spain): extraction of suitable grain size for reliable 14C dating, Radiocarbon 54 (2012) 23–36.
- [35] S. Miyata, Anion-exchange properties of hydrotalcite-like compounds, Clays Clay Miner. 31 (1983) 305–311.
- [36] M. Meyn, K. Beneke, G. Lagaly, Anion-exchange reactions of layered double hydroxides, Inorg. Chem. 29 (1990) 5201–5207.
- [37] K. Rozov, U. Berner, C. Taviot-Gueho, F. Leroux, G. Renaudin, D. Kulik, L.W. Diamond, Synthesis and characterization of the LDH hydrotalcite-pyroxaurite solid-solution series, Cem. Concr. Res. 40 (2010) 1248–1254.
- [38] S.J. Mills, A.G. Christy, J.-M.R. Génin, T. Kameda, F. Colombo, Nomenclature of the hydrotalcite supergroup: natural layered double hydroxides, Mineral. Mag. 76 (2012) 1289–1336.
- [39] D.G. Evans, R.C.T. Slade, Structural aspects of layered double hydroxides, in: X. Duan, D.G. Evans (Eds.), Layered Double Hydroxides, Springer Berlin Heidelberg, Berlin, Heidelberg, 2006, pp. 1–87.
- [40] E. Busenberg, L.N. Plummer, The kinetics of dissolution of dolomite in CO₂-H₂O systems at 1.5 to 60°C and 0 to 1atm PCO₂, Geochim. Cosmochim. Acta 282 (1982) 45–78.
- [41] X. Zhang, F.P. Glasser, K.L. Scrivener, Reaction kinetics of dolomite and portlandite, Cem. Concr. Res. 66 (2014) 11–18.
- [42] T. Prinčič, P. Štukovnik, S. Pejovnik, G. De Schutter, V. Bokan Bosiljkov, Observations on dedolomitization of carbonate concrete aggregates, implications for ACR and expansion, Cem. Concr. Res. 54 (2013) 151–160.
- [43] D.W. Hobbs, Alkali-Silica Reaction in Concrete, Thomas Telford, London, 1988.
- [44] J. Smeltz, J. Farver, Dedolomitization and Alkali Reactions in Ohio-sourced Dolstone Aggregates (No. FHWA/OH-2017-9), Department of Transportation, Ohio, 2017.
- [45] D.R.M. Brew, F.P. Glasser, Synthesis and characterisation of magnesium silicate hydrate gels, Cem. Concr. Res. 35 (2005) 85–98.
- [46] D. Nied, K. Enemark-Rasmussen, E. L'Hopital, J. Skibsted, B. Lothenbach, Properties of magnesium silicate hydrates (M-S-H), Cem. Concr. Res. 79 (2016) 323–332.
- [47] C. Roosz, S. Grangeon, P. Blanc, V. Montouillout, B. Lothenbach, P. Henocq, E. Giffaut, P. Vieillard, S. Gaboreau, Crystal structure of magnesium silicate hydrates (M-S-H): the relation with 2:1 Mg-Si phyllosilicates, Cem. Concr. Res. 73 (2015) 228–237.
- [48] S.A. Walling, H. Kinoshita, S.A. Bernal, N.C. Collier, J.L. Provis, Structure and properties of binder gels formed in the system Mg(OH)₂-SiO₂-H₂O for immobilisation of Magnox sludge, Dalton Trans. 44 (2015) 8126–8137.
- [49] E. Bernard, B. Lothenbach, C. Cau-Dit-Coumes, C. Chlique, A. Dauzères, I. Pochard, Magnesium and calcium silicate hydrates, part I: investigation of the possible magnesium incorporation in calcium silicate hydrate (C-S-H) and of the calcium in magnesium silicate hydrate (M-S-H), Appl. Geochem. 89 (2018) 229–242.
- [50] E. Bernard, B. Lothenbach, F. Le Goff, I. Pochard, A. Dauzères, Effect of magnesium on calcium silicate hydrate (C-S-H), Cem. Concr. Res. 97 (2017) 61–72.
- [51] E. Bernard, B. Lothenbach, D. Rentsch, I. Pochard, A. Dauzères, Formation of magnesium silicate hydrates (M-S-H), Phys. Chem. Earth, Parts A/B/C 99 (2017) 142–157.
- [52] M. Zajac, S.K. Bremseth, M. Whitehead, M. Ben Haha, Effect of CaMg(CO₃)₂ on hydrate assemblages and mechanical properties of hydrated cement pastes at 40°C and 60°C, Cem. Concr. Res. 65 (2014) 21–29.
- [53] A. Machner, M. Zajac, M. Ben Haha, K.O. Kjellens, M.R. Geiker, K. De Weerd, Limitations of the hydrotalcite formation in Portland composite cement pastes containing dolomite and metakaolin, Cem. Concr. Res. 105 (2018) 1–17.
- [54] P. Sipos, The structure of Al(III) in strongly alkaline aluminate solutions — a review, J. Mol. Liq. 146 (2009) 1–14.
- [55] S. Miyata, A. Okada, Synthesis of hydrotalcite-like compounds and their physico-chemical properties-the systems Mg²⁺-Al³⁺-SO₄²⁻ and Mg²⁺-Al³⁺-CrO₄²⁻, Clays Clay Miner. 25 (1977) 14–18.
- [56] S. Miyata, Physico-chemical properties of synthetic hydrotalcites in relation to composition, Clays Clay Miner. 28 (1980) 50–56.
- [57] J. Schork, Dolomitic lime in the US, J. Arch. Conserva. 18 (2012) 7–25.
- [58] K. Grover, S. Komarneni, H. Katsuki, Synthetic hydrotalcite-type and hydrocalumite-type layered double hydroxides for arsenate uptake, Appl. Clay Sci. 48 (2010) 631–637.
- [59] H.F.W. Taylor, Cement Chemistry, Thomas Telford, London, 1997.
- [60] Z. Maciej, M. Ben Haha, Hydration of limestone and dolomite cement, 14th International Congress on the Chemistry of Cement, Beijing, China, 2015.
- [61] E. Heritage, Practical Building Conservation: Mortars, Renders & Plasters, Ashgate, Surrey, 2011.
- [62] N. Copsey, Hot Mixed Lime and Traditional Mortars: A Practical Guide to Their Use in Conservation and Repair, The Crowood Press, Ramsbury, Marlborough, 2019.
- [63] A. Forster, Hot-lime mortars: a current perspective, J. Arch. Conserv. 10 (2004) 7–27.
- [64] J. Válek, T. Matas, Experimental study of hot mixed mortars in comparison with lime putty and hydrate mortars, Historic Mortars, Springer Netherlands, Dordrecht, 2012, pp. 269–281.
- [65] Arizkun. Available online:<http://meteo.navarra.es/climatologia/selfichaclima.cfm?IDEstacion=66&tipo=MAN>(accessed on 3 May 2019).

APPENDIX III.2

Petrographic and chemical-mineralogical characterization of mortars from the cistern at Amaiur Castle (Navarre, Spain)

Graciela Ponce-Antón, Maria Cruz Zuluaga, Luis Angel Ortega, Juantxo Agirre Mauleon

Minerals 2020; 10(4):311

Article Metrics

✓ Journal Citation Reports

Citations: 0

Impact Factor

2018	5 Years
2.25	2.453

JCR® Rank	Classification	Quartile	Percentile
Mineralogy	12 of 29	Q2	60.345
Mining & Mineral Processing	6 of 19	Q2	70.053

✓ Scopus

Citations: 0

CiteScore 2018	2.46
SJR 2018	0.427
SNIP 2018	0.966


CiteScore Rank	Classification	Percentile
Earth and Planetary Sciences (Geotechnical Engineering and Engineering Geology)	39 of 176	78
Earth and Planetary Sciences (Geology)	47 of 217	78

✓ Google Academic

Citations: 0

Article

Petrographic and Chemical–Mineralogical Characterization of Mortars from the Cistern at Amaiur Castle (Navarre, Spain)

Graciela Ponce-Antón ^{1,*}, Maria Cruz Zuluaga ¹, Luis Angel Ortega ¹ and Juantxo Agirre Mauleon ²

¹ Department of Mineralogy and Petrology, Faculty of Science and Technology, University of the Basque Country (UPV/EHU), Sarriena s/n, 48940 Leioa, Bizkaia, Spain; mcruz.zuluaga@ehu.eus (M.C.Z.); luis.ortega@ehu.eus (L.A.O.)

² Aranzadi Society of Sciences, Zorroagaina 11, 20014 Donostia-San Sebastián, Gipuzkoa, Spain; zuzendaritza@aranzadi.eus

* Correspondence: graciela.ponce@ehu.eus; Tel.: +34-946-015-456

Received: 11 March 2020; Accepted: 30 March 2020; Published: 31 March 2020



Abstract: Mortars from the cistern in Amaiur Castle (Navarre, Spain) were analysed to assess the mortar manufacturing process and application techniques. To this end, optical microscopy, scanning electron microscopy (SEM), thermogravimetric analysis, X-ray fluorescence (XRF), X-ray diffraction (XRD), Raman microspectroscopy, and Fourier transform infrared spectroscopy (FTIR) were performed. The study of both structural and plaster mortars from Amaiur Castle cistern show patterns/rules in the mortar manufacture according to the specific construction requirements. A multilayer application technique was used for the construction of the cistern tank. Deliberate selection of the aggregate nature and grading contributed to mortar impermeability. Ceramic and silico-aluminous rock fragments were used as aggregates in the cistern tank to confer hydraulicity to the mortars, instead of carbonated aggregates as used in the vault. Aluminosilicated phases present in the aggregates led to the formation of amesite, which is a magnesium aluminosilicate hydrate (M-A-S-H) phase conferring hydraulicity to the mortar. Two types of additives were identified in the outer pigmented layer of plaster. Beeswax was the identified organic additive used to improve the impermeability of mortar, while hematite was the identified inorganic additive giving rise to the reddish colour of the layer.

Keywords: lime mortar; plaster; hydraulicity; reaction rim; hydrotalcite; amesite; hematite; beeswax

1. Introduction

Cisterns have been essential structures for water storage since the Neolithic period not only to guarantee a regular and independent water supply in regions with water shortages but also to ensure the supply during drought or siege periods, particularly in castles or fortified sites [1–4]. The need to store and supply water required improvements in the hygienic conditions of the cisterns and led to structural and technological advances in the structures [5].

The great deteriorating capacity of water constitutes one of the main causes of construction material deterioration [6]. Cistern mortars are continuously in contact with water. Therefore, to ensure the impermeability and durability of mortars in the cistern tank, specific requirements are necessary compared with other building structures, in both the mortar manufacture and application technology practices [7].

Mortar impermeability is strictly related to mortar hydraulicity [8]. In hydraulic mortars, the hardening occurs mainly by the chemical reaction with water rather than by exposure to carbon dioxide as happens in non-hydraulic mortars. The amount of reactive silicates and aluminates present

in the mixture will determine the hydraulicity degree of mortar [9]. To obtain the waterproofing of mortars, a reactive additive, mainly pozzolanic components such as crushed bricks or calcined clays, have been added to the mixture to provide hydraulic properties to non-hydraulic mortars, improving their resistance to moisture [10–14]. Pozzolans are highly reactive materials mainly composed of aluminosilicate phases that in the presence of water react with the calcium hydroxide $[\text{Ca}(\text{OH})_2]$ and form stable aluminosilicate hydrated products that confer hydraulic properties to mortars [8,15]. Due to this reaction, a reaction rim can be formed surrounding the aggregates [16]. Moreover, natural organic compounds have also been added to the mixture to achieve specific behaviours in mortars [17].

The present study aims to perform petrographic and chemical–mineralogical characterisation of the structural and plaster mortars of the cistern from Amaiur Castle to assess the mortar manufacturing process and application technology used according to the specific requirements for the construction of this structure.

2. Geological and Archaeological Setting

Amaiur Castle (Navarre, Spain) is located geologically on Triassic limestones and dolostones, although Paleozoic and Mesozoic materials outcrop in the regional geology. The Paleozoic is characterized by Ordovician to Carboniferous metamorphic materials, consisting mainly of schist and quartzites and scarce limestones and dolomites, and by Permian carbonated and slaty breccias, limestones, and sandstones. Regionally, Triassic materials are characterised by conglomerates and sands in the Buntsandstein Facies, dolomitic limestones and dolostones in the Muschelkalk Facies, mottled clays with gypsum in the Keuper Facies, and subvolcanic basic rocks associated with the Keuper Facies [18,19].

The strategic emplacement of Amaiur Castle in the western Pyrenees allowed it to control the pass across this mountain range during the Middle Ages. Although the castle was first mentioned by written sources in the 12th century, the archaeological evidence showed an occupation period from the 13th century to the 17th century (Figure 1). Amaiur Castle defences were reinforced during the 14th century due to artillery development in that same century. Also in the 14th–15th century, a second wall reinforced the 13th–14th century medieval wall. During the 16th and 17th centuries, the castle was largely remodelled, owing to the conflicts occurring in the region at that time. In the 16th century, a circular bastion was added to the 14th–15th century medieval wall. The studied cistern was built at this time between the two medieval walls, giving rise to a rectangular-based tank cistern (Figure 2), and much of the space between the two medieval walls was filled with lime mortar. Later, in the 17th century, the fortification was transformed into a trace italienne bastion with the addition of diamond-shaped structures [20–22].



Figure 1. Geographic location of Amaiur Castle (Navarre, Spain). Studied samples are marked by red circles. Modified from Ponce-Antón et al. [23].



Figure 2. Location of the studied samples within the cistern. Cistern tank in green, vault lunette in blue, barrel vault in yellow, and 14th–15th centuries wall in black.

3. Materials and Methods

3.1. Materials

Seven representative lime mortar samples were collected from the preserved remains of the cistern (Table 1, Figures 1 and 2). A total of six samples of structural mortar were collected, three from the walls of the tank (Samples CA-AL-7 and CA-AL-8 from the SE wall and Sample CA-AL-9 from the SW wall), two from the base of the barrel vault (Samples CA-AL-5 and CA-AL-6), and one from the vault lunette (CA-AL-2). Sample CA-AL-8 has been subdivided into two different samples (CA-AL-8a and CA-AL-8b) due to the granulometric differences observed on a macroscopic scale. Since both the tank walls and lunette are covered with the same plaster, an additional sample of plaster was collected from the lunette (CA-AL-1) in the area where the plastering is best preserved.

Table 1. Lime mortar samples from the different locations in Amaiur Castle cistern.

Mortar Type	Structure	Location	Sample	
Structural	Barrel vault	Lunette	CA-AL-2	
		Base	CA-AL-5	
			CA-AL-6	
	Tank	Inner layer	CA-AL-7	
		Outer layer	CA-AL-8	CA-AL-8b
			CA-AL-9	CA-AL-8a
Plaster	Inner layer Pigmented layer	CA-AL-1		

3.2. Methods

Petrographic characteristics of mortars were studied by polarized light microscopy (PLM) (JEOL, Tokyo, Japan) on polished thin sections and in both transmitted and reflected polarized light modes using a Nikon Eclipse LV100POL polarizing microscope equipped with a DS F-11 digital camera and DS L2 camera control unit.

Scanning electron microscopy (SEM) analysis was carried out on carbon-coated polished thin sections using a JEOL JSM-7000F Schottky-type field emission scanning electron microscope (JEOL, Tokyo, Japan) equipped with an INCA EDX detector X-sight Series Si (Li) Oxford pentaFET microanalysis system.

Thermogravimetric analysis (TGA) was performed using a TA SDT 2960 TG-DSC simultaneous instrument (TA Instruments, New Castle, DE, USA). A 5 to 7 mg of sample were heated in Pt crucibles at 2 °C min⁻¹ from room temperature to 900 °C under a dry oxidizing atmosphere.

The semiquantitative chemical composition of major elements of the mortar binder fraction <2 µm was determined by means of X-ray fluorescence (XRF). A Wavelength Dispersive X-ray Fluorescence (WDXRF) PANalytical Axios Advanced PW4400 XRF spectrometer (with 4 kW Rh anode SST-mAX X-ray tubes) (Malvern PANalytical, Almelo, The Netherlands) was used to perform the analyses on a powder sample. The detection limit was of 0.01 wt%. The loss on ignition (LOI) was calculated after heating the powder sample at 900 °C.

The X-ray diffraction (XRD) analysis was performed to determine the mineralogy of powder polycrystalline samples using a Philips X'Pert diffractometer (Malvern PANalytical, Almelo, The Netherlands) equipped with a monochromatic Cu-ka1 X-radiation in a continuous scan from 5° to 70° 2θ operating at 40 kV and 20 mA conditions with an acquisition rate of 0.02° per second. X'Pert HighScore Plus 3.0 software by PANalytical (Malvern PANalytical, Almelo, The Netherlands) and the experimental patterns of the International Centre for Diffraction Data (ICDD) and the Inorganic Crystal Structure Database (ICSD) diffraction databases were used for the mineral phase identification.

Micro-Raman analyses were performed using a Renishaw inVia confocal microRaman spectrometer (Renishaw inVia, Gloucestershire, UK). Spectra were acquired between 1000 and 1120 cm^{-1} with a 1 cm resolution and the data acquisition was carried out using Renishaw's WireTM 3.2 software package (Renishaw, Gloucestershire, UK). Raman spectra of pure standard compounds collected in the e-VISNICH dispersive Raman database were used to interpret the results.

Fourier transform infrared spectroscopy (FTIR) by the potassium bromide pellet technique was carried out to determine the nature of the organic compounds using a JASCO 4200 FTIR spectrometer (JASCO INTERNATIONAL CO., Hachioji, Tokyo, Japan) and acquiring spectra between 400 and 4000 cm^{-1} .

To improve the FTIR signal of the organic components, an extraction was conducted using 200 μL of dichloromethane organic solvent.

Hydraulicity Index (HI) (Equation (1)) and Cementation Index (CI) (Equation (2)) values were calculated to assess the hydraulicity of the binder according to Boynton formula [24,25]. Indices were calculated as below:

$$\text{HI} = \frac{\text{SiO}_2 + \text{Al}_2\text{O}_3}{\text{CaO} + \text{MgO}}, \quad (1)$$

$$\text{CI} = \frac{2.8\text{SiO}_2 + 1.1\text{Al}_2\text{O}_3 + 0.7\text{Fe}_2\text{O}_3}{\text{CaO} + 1.4\text{MgO}}. \quad (2)$$

4. Results

4.1. Petrographic and Chemical–Mineralogical Characterization

Macroscopically, a difference in the nature of aggregates was observed between the plaster (Figure 3a), mortars from the tank (Figure 3b–d), and the mortars from the vault (Figure 3e,f). Sample CA-AL-2 from the lunette of the vault and Samples CA-AL-5 and CA-AL-6 from the base of the barrel vault (structural mortars) show carbonated aggregates, whereas Samples CA-AL-7, CA-AL-8 and CA-AL-9 (structural mortars), and Sample CA-AL-1 (plaster) show siliceous aggregates. Mortars from the tank also show increasing aggregate grading, from structural mortars (inner part; Samples CA-AL-7, CA-AL-8, and CA-AL-9) to the plaster (outer part; Sample CA-AL-1) (Figure 3).



Figure 3. Macroscopic texture of the lime mortars from the Amaiur Castle cistern. (a) CA-AL-2, plaster sample. (b) CA-AL-8a, (c) CA-AL-8b, and (d) CA-AL-7, samples from the tank mortars. (e) CA-AL-2 and (f) CA-AL-5, mortars from the vault. Mortars from the tank show an increase in aggregate grading from the inner part (d) to the outer part (a).

Microscopically, all samples show a heterogeneous binder matrix-supported texture with aggregates embedded in a micritic calcite matrix. Petrographic observations of mortar identified the carbonated aggregates of samples from the vault as poorly sorted fine-grained dolostone fragments with angular to subangular shape (Figure 4a). The grain sizes of aggregates from the vault base (Samples CA-AL-5 and CA-AL-6) range from 0.2 mm up to 3 mm, whereas aggregates from the lunette

(CA-AL-2) reach 8 mm in size. Dolostone aggregates show a pronounced reaction zone (Figure 4a). Scarce ceramic fragments can also be observed dispersed in the binder matrix.

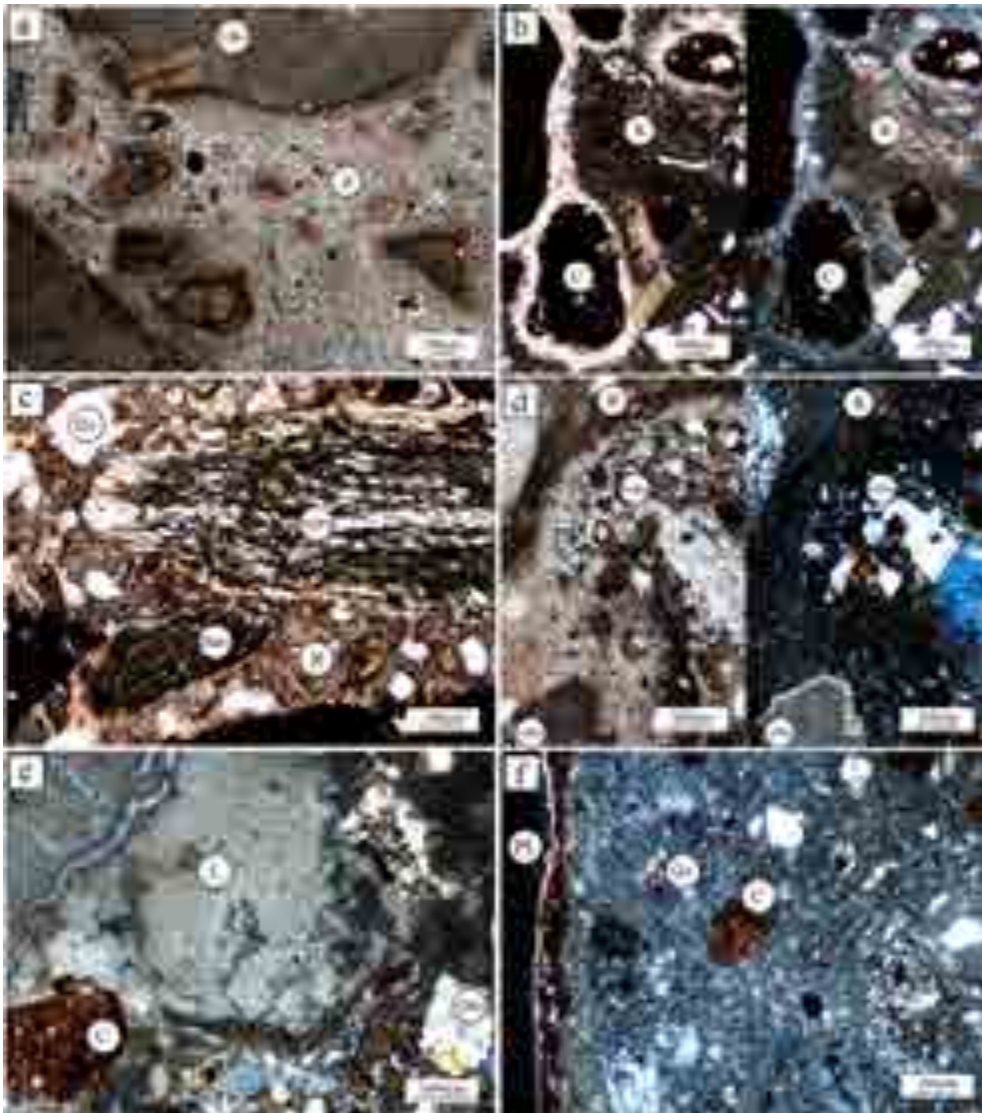


Figure 4. Photomicrographs showing the most representative microtextures of the lime mortars from Amaiur Castle cistern. (a), (b)-left, (c) and (d)-left: plane polarized light mode (PPL). (b)-right, (d)-right, (e,f): crossed-polarized light mode (XPL). C: ceramic; DRx: dolostone; L: lime lump; PhRx: phyllite; PL: pigmented layer; QRx: quartzite; Qz: quartz; R: reaction zone; ScRx: Schist; SvRx: subvolcanic rock.

The nature of the aggregates from the cistern tank mortars is the same in both structural mortars (Samples CA-AL-7, CA-AL-8, and CA-AL-9) and plaster (Samples CA-AL-1). Mortars are mainly composed of subangular to rounded ceramic fragments (s.l.), and the siliceous aggregates observed macroscopically have been identified as well-rounded quartz grains and phyllite, schist, quartzite, sandstone, and subvolcanic rocks (Figure 4b–e). Dolostone fragments were also observed in minor amounts, and also some charcoal fragments were dispersed in the binder matrix. Heterometric lime lumps up to 4 mm were also observed (Figure 4e).

The grain size of aggregates decreases and aggregate sorting increases from the inner layer of the structural mortar (Sample CA-AL-7) to the outer part (CA-AL-8 and CA-AL-9). Sample CA-AL-7 shows very poorly sorted aggregates from 0.7 mm to 2 cm in size. The outer part of Sample CA-AL-8 (CA-AL-8a) is very similar to Sample CA-AL-9, with smaller and more sorted aggregates than the

inner part of Sample CA-AL-8 (CA-AL-8b). Both Subsample CA-AL-8b and Sample CA-AL-9 show moderately sorted aggregates ranging from 0.2 mm up to 3 mm in grain size, whereas Subsample CA-AL-8a shows better sorted aggregates from 0.1 to 1.3 mm in size.

Sample CA-AL-1 corresponding to the plaster mortar consists of two different layers (Figure 4f). The inner layer of the plaster is also composed by the well-rounded and sorted ceramic and polygenic rock aggregates, as observed in the structural mortars of the cistern, which are up to 0.3 mm in size. The outer layer of the plaster is a reddish pigmented layer around 0.15 mm thick showing a scarce amount of mica-like phyllosilicates and quartz grains.

Binder/aggregate ratios were defined by the comparison of the chart for volume percentage estimation [26]. Samples show a binder/aggregate ratio between 1:2 and 1:1, except for Sample CA-AL-7, which shows a binder/aggregate ratio of 1:1 and the inner layer of plaster, which shows a binder/aggregates ratio of 2:1.

To determine the composition of the mortar binders, Sample CA-AL-2 from the vault lunette, Sample CA-AL-9 from the structural mortars of the tank, and both inner and pigmented layers of plaster (Sample CA-AL-1) were selected for X-ray diffraction (XRD) analysis.

A binder fraction $<2 \mu\text{m}$ of Samples CA-AL-2 and CA-AL-9 was extracted in order to avoid the interference of the aggregate composition following the procedures described by Ortega et al. [27] and Ponce-Anton et al. [28]. The small amount of Sample CA-AL-1 from the plaster made it impossible to extract the binder fraction $<2 \mu\text{m}$, and thus the bulk fraction of both inner and pigmented layers was analysed. For the analysis of the inner layer, the aggregates observable with the naked eye were removed.

The XRD results are shown in Figure 5. All samples are mainly composed of magnesium calcite $[(\text{Ca}, \text{Mg})\text{CO}_3]$, and in minor amounts, hydrotalcite $[\text{Mg}_6\text{Al}_2(\text{CO}_3)(\text{OH})_{16}\cdot 4(\text{H}_2\text{O})]$ was also detected in all samples, except in the pigmented layer where only traces were detected. Quartz $[\text{SiO}_2]$ and illite-like phyllosilicates were detected in samples from the cistern tank in both structural and plaster mortars. Reflection peaks at 7.03 \AA and 3.51 \AA allowed to detect small amounts of the amesite mineral phase $[\text{Mg}_2\text{Al}_2\text{SiO}_5(\text{OH})_4]$ in Sample CA-AL-9 and in the inner layer of the plaster. Hematite $[\text{Fe}_2\text{O}_3]$ was also identified in the pigmented outermost layer of the plaster.

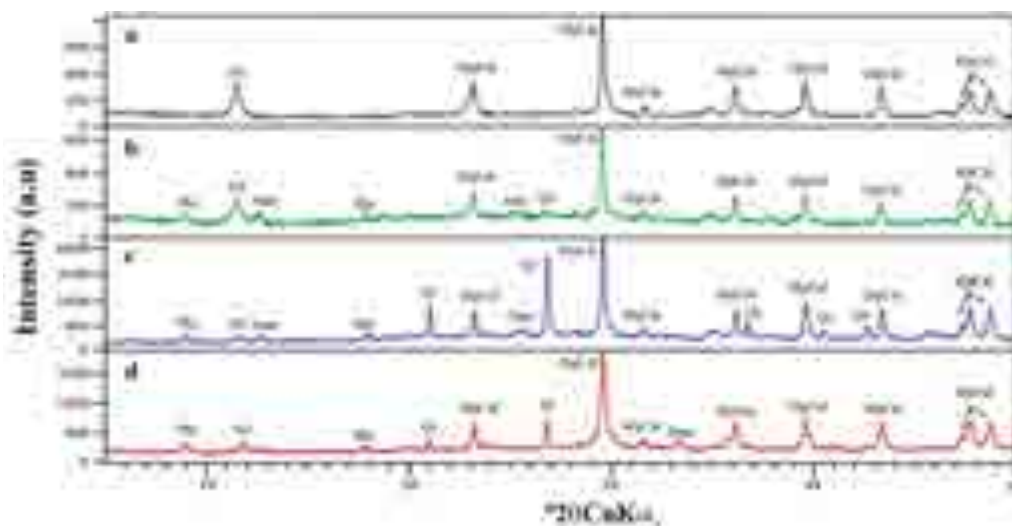


Figure 5. X-ray diffraction patterns of the lime mortars from Amaiur Castle cistern. (a) Binder fraction $<2 \mu\text{m}$ from the lunette. (b) Binder fraction $<2 \mu\text{m}$ from the structural mortar of the tank. (c) Bulk fraction from the inner layer of the plaster mortar. (d) Bulk fraction from the pigmented layer of the plaster mortar. Ame: amesite, Hem: hematite, HT: hydrotalcite; Mg-cal: magnesium calcite, Phy: phyllosilicates s.l., Qz: quartz.

Both hydrotalcite and amesite have been the Mg-hydrated phases detected by XRD. Hydrotalcite is a layered double hydroxide phase (LDHs) [29], whereas amesite is a magnesium aluminosilicate hydrate phase (M-A-S-H).

To confirm the presence of the Mg-hydrated phases detected by XRD, the binder fraction $<2\ \mu\text{m}$ of Samples CA-AL-2 (vault mortar) and CA-AL-9 (tank mortar) were analysed by thermogravimetric analysis (TGA). The TGA results are shown in Figure 6.

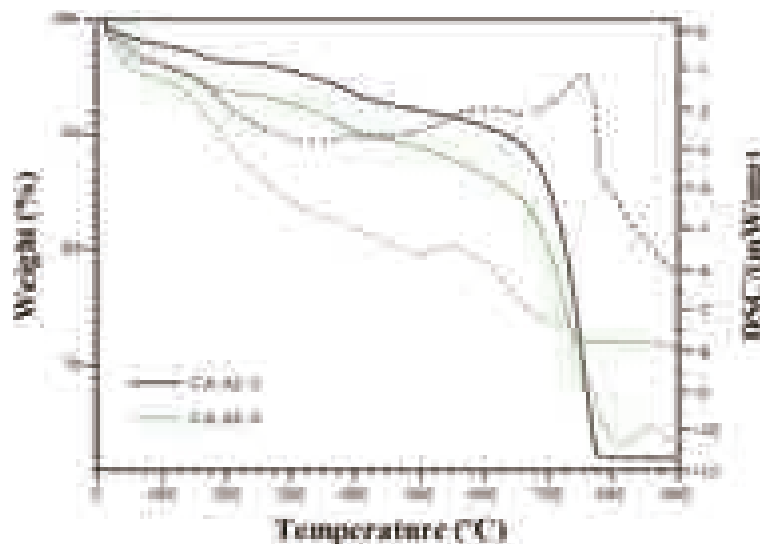


Figure 6. Thermogravimetric analyses of the binder fraction $<2\ \mu\text{m}$ from the vault mortar (Sample CA-AL-2 in black) and tank mortar (Sample CA-AL-9 in green).

Sample CA-AL-2 shows a total weight loss of 38.14%, whereas Sample CA-AL-9 shows a total weight loss of 28.17%. Since the total weight loss of pure calcium carbonate is 44%, these lower weight losses indicate the presence of other mineral phases in the binder as indicated by the XRD results (Figure 5).

The TGA curves show four main weight loss regions. The first weight loss ($<120\ ^\circ\text{C}$) and the second weight loss (120 to $200\ ^\circ\text{C}$) are attributed to the adsorption water and poorly bonded interlayer water, respectively. The third weight loss (200 to $600\ ^\circ\text{C}$) is attributed to dehydration caused by the loss of hydroxyl groups (OH^-). The last fourth weight loss (600 to $800\ ^\circ\text{C}$) is related to the decomposition of the carbonates [30–32]. No weight loss is observed over $800\ ^\circ\text{C}$. Considering the DSC curve, between 200 and $600\ ^\circ\text{C}$, two endothermic peaks are observed in both Sample CA-AL-2 and Sample CA-AL-9. These two endothermic peaks correspond to the hydrotalcite (LDHs), which decomposes in two steps in this range of temperatures [33,34]. Nevertheless, the second endothermic peak between 450 and $600\ ^\circ\text{C}$ can also be related to the decomposition of the amesite (M-A-S-H) and illite-like phyllosilicates [35–38] present in Sample CA-AL-9, and therefore, they appear to overlap. Between 800 and $900\ ^\circ\text{C}$, an endothermic peak is only detected in Sample CA-AL-9, confirming the presence of amesite and illite in the tank mortar sample, since the breakdown of both phases takes place in this temperature range [35–37].

X-ray fluorescence was performed to determine the chemical composition of the binder fraction $<2\ \mu\text{m}$ of Samples CA-AL-2 and CA-AL-9. Chemical results of both vault and tank mortars (Samples CA-AL-2 and CA-AL-9, respectively) were used to calculate the Hydraulicity Index (HI) and Cementation Index (CI) in order to assess and compare the hydraulicity degree of binders from the vault and tank (Table 2). Hydraulicity is classified as weak ($\text{HI} = 0.1\text{--}0.2$, $\text{CI} = 0.3\text{--}0.5$), moderate ($\text{HI} = 0.2\text{--}0.4$, $\text{CI} = 0.5\text{--}0.7$), and eminent ($\text{HI} < 0.4$, $\text{CI} = 0.7\text{--}1.1$) [24,25]. According to the HI and CI values, the mortar binder from the cistern tank is eminently hydraulic, whereas the mortar binder from the vault is weakly hydraulic.

Table 2. Semiquantitative results of the major elements of the binder fraction <2 μm in powder samples from the lunette of the barrel vault and tank samples determined by X-ray fluorescence, the hydraulicity index (HI), and the cementation index (CI). Chemical results are expressed as oxides in wt%. Iron content is expressed as total $\text{Fe}_2\text{O}_3\text{t}$. LOI: loss on ignition (%).

Sample	Structure	MgO	Al_2O_3	SiO_2	K_2O	CaO	TiO_2	MnO	$\text{Fe}_2\text{O}_3\text{t}$	LOI	HI	CI
CA-AL-2	Lunette	6.16	2.43	5.55	0.23	44.73	0.20	0.05	2.40	38.14	0.20	0.37
CA-AL-9	Tank	6.70	8.15	21.12	1.08	29.20	0.35	0.15	4.88	28.17	0.95	1.85

4.2. Study of the Pigmented Layer of Plaster

Scanning electron microscopy (SEM) was performed on Sample CA-AL-1 for better characterization of the plaster. SEM observations show that the pigmented layer of plaster is less porous than the inner layer and that the contact surface between both layers is rough (Figure 7).

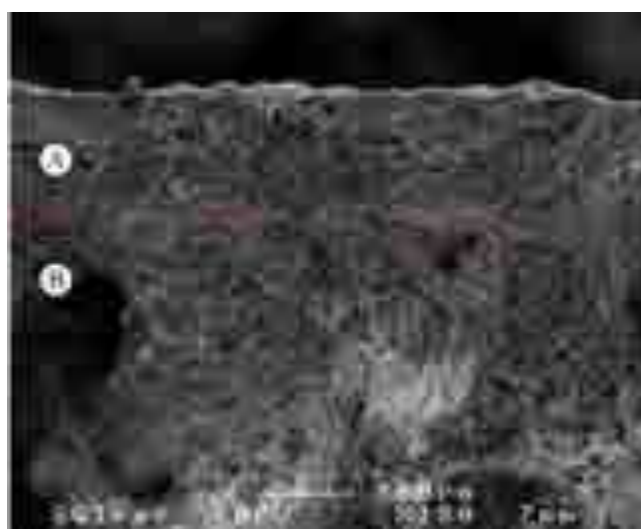


Figure 7. SEM image of the cistern plaster. A: pigmented layer; B: inner layer. Rough contact surface in red.

The outermost pigmented layer of the plaster was also analysed by Raman spectroscopy and Fourier transform infrared spectroscopy (FTIR) in order to determine whether any other type of additive was used in the manufacture. Raman spectroscopy confirmed that the pigmented layer of plaster is mainly composed of a mixture of calcite and hematite (Figure 8a).

Raman spectra show intense bands at 282 cm^{-1} , 712 cm^{-1} , and 1087 cm^{-1} attributed to calcite and less intense bands at 226 cm^{-1} , 294 cm^{-1} , and 410 cm^{-1} attributed to hematite [39,40]. Broad bands at 355 and 464 cm^{-1} related to quartz are also observed. The broad band identified in the region of $1150\text{--}1450\text{ cm}^{-1}$ is attributed to an organic compound, but due to the low quality of the spectrum, it was difficult to identify (Figure 8b).

Infrared spectroscopy (FTIR) analysis was performed in order to identify the organic compound detected by Raman spectroscopy. FTIR spectra show bands at 2864 cm^{-1} , 2514 cm^{-1} , 1794 cm^{-1} , 1428 cm^{-1} , 871 cm^{-1} , and 711 cm^{-1} attributed to calcite and bands at 1027 cm^{-1} , 642 cm^{-1} and 528 cm^{-1} attributed to the hematite (red earth pigment) (Figure 9a) [41–43]. Nevertheless, the strong absorption of the inorganic phases hides the signal of the organic compound, hindering its identification. To improve the FTIR signal of the organic component, an extraction was conducted using $200\text{ }\mu\text{L}$ of dichloromethane. The resulted supernatant was evaporated on a potassium bromide disk to be then analysed. The intense bands detected at 2955 cm^{-1} , 2916 cm^{-1} , 2848 cm^{-1} , 1736 cm^{-1} , and 1472 cm^{-1} were attributed to beeswax organic compound (Figure 9b) [43].

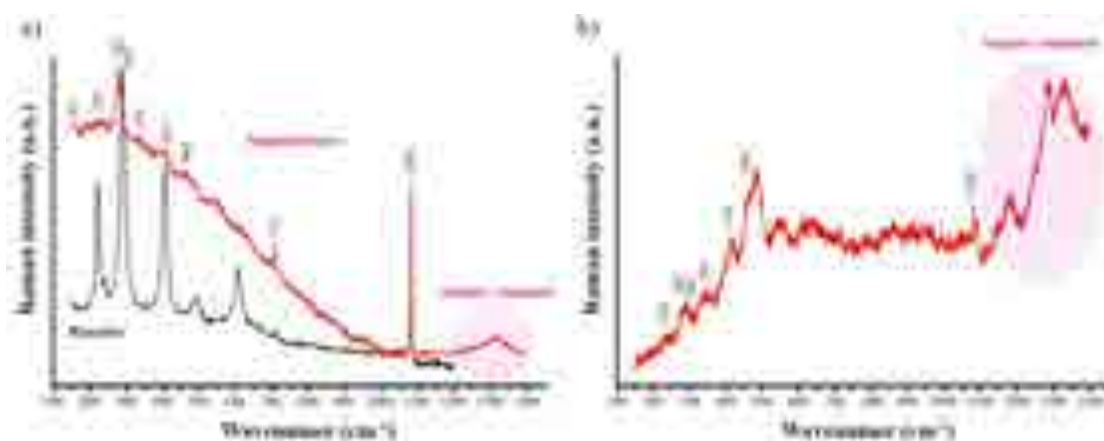


Figure 8. Raman spectroscopy of the bulk fraction of the pigmented layer of the cistern plaster. (a) Raman spectra showing the highest intensities bands of calcite, hematite, and quartz. (b) Raman spectra showing an organic compound in the region of 1150–1450 cm^{-1} . Calcite bands at 282 cm^{-1} , 712 cm^{-1} , and 1087 cm^{-1} ; hematite bands at 226 cm^{-1} , 294 cm^{-1} , and 410 cm^{-1} ; quartz bands at 355 cm^{-1} and 464 cm^{-1} .

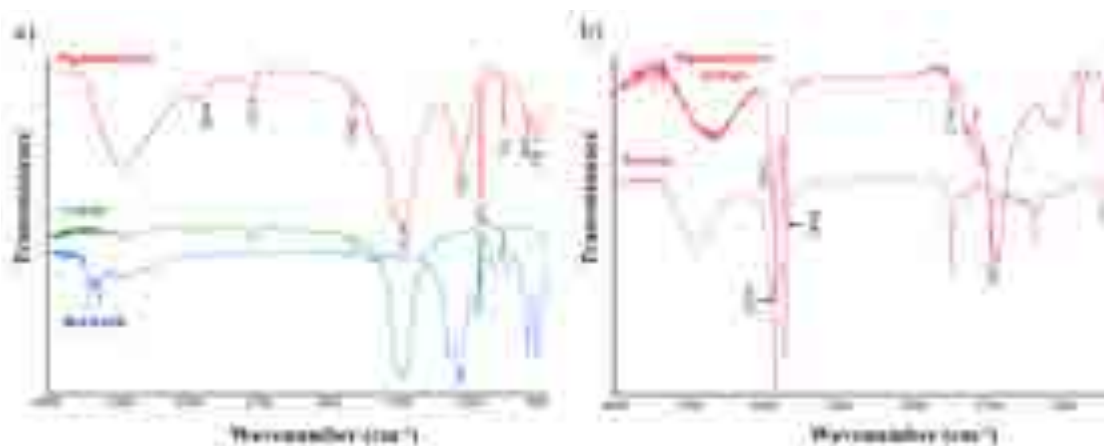


Figure 9. Fourier transform infrared spectroscopy (FTIR) analysis of the pigmented layer of the cistern plaster. (a) FTIR spectra showing the highest intensities bands of calcite and hematite (red earth). (b) FTIR spectra showing the highest intensities bands of the organic compound identified as beeswax. Calcite bands at 2864 cm^{-1} , 2514 cm^{-1} , 1794 cm^{-1} , 1428 cm^{-1} , 871 cm^{-1} , and 711 cm^{-1} ; hematite (red earth) bands at 1027 cm^{-1} , 642 cm^{-1} , and 528 cm^{-1} . Beeswax bands at 2955 cm^{-1} , 2916 cm^{-1} , 2848 cm^{-1} , 1736 cm^{-1} , and 1472 cm^{-1} .

5. Discussion

Petrological study suggests a careful process in both the mortar manufacture and mortar application technique for the cistern construction according to the specific characteristics needed for this structure. The impermeability of the cistern tank is an essential requirement for appropriate water storage. Mortar impermeability is strictly related to mortar hydraulicity, which is favoured by the use of silico-aluminous aggregates working as reactive materials in the mixture [8,10–13]. The use of silico-aluminous rocks and ceramic fragments as aggregates in the tank mortar manufacture, instead of the carbonated aggregates used for the vault mortars, indicates a deliberate selection of aggregates in order to confer hydraulicity to the mortar to obtain waterproof mortars. Furthermore, the use of silico-aluminous aggregates adds greater cohesion and mechanical strength to the mortar [44,45].

The raw materials that were used as aggregates to manufacture both the lime mortars from the vault and cistern tank correspond to the surrounding geological materials. Not only the selection of aggregates was important but also the aggregate sorting. The grain size of aggregates in the

tank mortars becomes smaller and better sorted from the first layer of the structural mortar toward the outermost pigmented layer of the plaster. Besides, aggregate size also contributes to material reactivity, since the smaller the size, the higher the specific surface area and thus the higher the reaction rate [8,46–48]. Furthermore, mortar porosity is lower in mortars with better-sorted aggregates since they produce a better-packed system [49–52].

The mineralogical analyses allowed identifying additives in the pigmented layer. The XRD, Raman, and FTIR analyses indicate that hematite was used as an inorganic additive, which led to the reddish colour of the pigmented layer (Figures 5, 8 and 9). Hematite would not be related to ceramic fragments, since they were not observed either in the petrographic study or by XRD (Figures 4f and 5d). Therefore, the hematite may have been deliberately added. FTIR analyses allowed identifying the beeswax as the organic additive in the pigmented layer (Figure 9). Beeswax was the most common natural wax used as an organic additive to provide impermeability and sealing property to the materials [53]. Since organic compounds are more susceptible to degradation than inorganic compounds, knowledge of the composition of ancient additives is essential for appropriate interventions on archaeological structures [53,54].

Therefore, to ensure the impermeability of the cistern tank, a multilayer application of different mortars was performed using silico-aluminous aggregates and decreasing their grain size from the first layer of the structural mortar toward the inner layer and applying a final plaster with a beeswax-bearing pigmented layer (Figure 10).

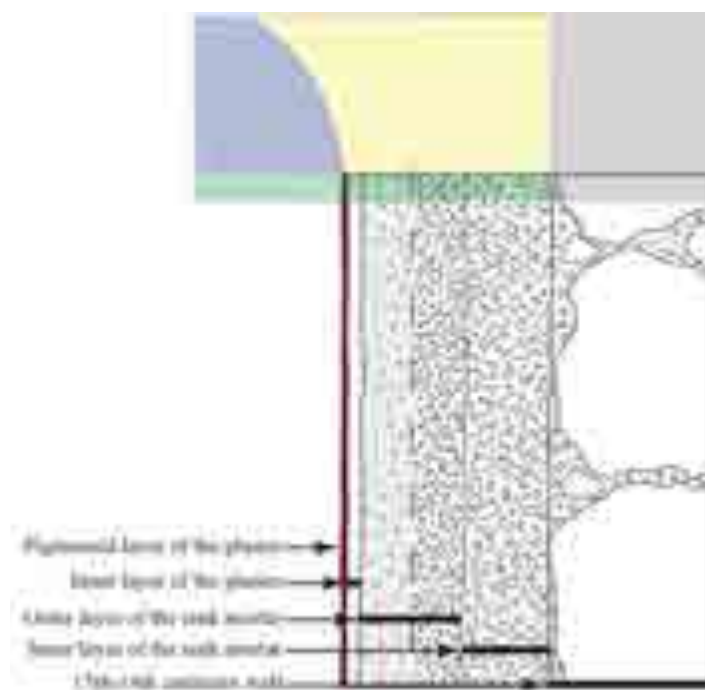


Figure 10. Schematic image of the multilayer application technique for mortars in Amaiur Castle cistern. The cistern tank is shown in green, the vault lunette is shown in blue, the barrel vault is shown in yellow, and the 14th–15th centuries wall is shown in black.

Furthermore, the reaction zones observed in dolomitic aggregates resulted from the dedolomitization of dolomitic aggregates, and the presence of hydrotalcite in the binder has been related to the use of the traditional hot-mixing method in mortar manufacture [23]. In the manufacture of cistern tank mortars, the use of this traditional hot-mixing method would also be expected since reaction zones were not only observed at the edge of the dolomitic aggregates, but they also stand out in the ceramic fragments and some silico-aluminous aggregates (Figure 4a–d).

Quartz and phyllosilicates are attributed to the ceramic fragments and silico-aluminous rocks used as aggregates, whereas magnesium calcite, hydrotalcite, and amesite are mineral phases formed during mortar manufacture (Figure 5). Magnesium calcite is formed in the setting of mortar as a result of the lime cycle [24,55], and hydrotalcite is a carbonated mineral formed during the slaking process in the presence of available magnesium content [28].

Hydrotalcite has been identified in all analysed mortar binders (Figure 5). Magnesium released from the dedolomitization process, leading to the formation of the reaction zone in the edge of dolomitic aggregates, and the aluminium released from the breakdown of phyllosilicates favours the formation of hydrotalcite [23,56–58]. Nevertheless, some amount of magnesium and aluminium can also come from the lime used for the mortar manufacture when impure limestones or partially dolomitized limestones have been used as the raw material for lime production [28,59]. Therefore, the presence of hydrotalcite and the absence of dolomitic aggregates in the pigmented layer of plaster (Figures 4 and 5) would indicate the use of impure limestones or partially dolomitized limestones for the production of lime for the cistern construction.

The aluminosilicate phases present in the silico-aluminous aggregates of the tank mortars are highly reactive materials that in the presence of alkalis react with water, forming a wide family of hydration products that induce hydraulic properties to the mortars [8,15,46]. Reaction zones observed in the edge of the silico-aluminous aggregates suggest the development of this reaction (Figure 4b–d). The reaction between aluminosilicate phases and an alkaline solution is known as an alkali-silicate reaction (ASSR), which is a specific type of alkali-silica reaction (ASR) [60–62].

Amesite has been the only aluminosilicate hydrated phase detected in the tank mortars. This mineral phase has also been described in some mortars with pozzolanic aggregates [48,63]. Amesite is a magnesium aluminosilicate hydrate (M-A-S-H) phase, and although it is chemically related to chlorites, it displays a similar structure to serpentine with alternating tetrahedral and trioctahedral layers [37]. The amesite has only been detected in samples containing silico-aluminous aggregates, indicating that it would have formed as a result of the reaction between the aluminosilicate phases and the putty alkalis.

Magnesium silicate hydrate (M-S-H) phases have been described during the hydration of MgO-bearing lime materials and formed by the reaction between magnesium and silicate ions [64–66]. The M-S-H phases show a layered structure and have been related to poorly crystalline phyllosilicates [64, 66–69]. The reaction zone of the dolomitic aggregates of the structural mortars from Amaiur Castle showed the presence of M-S-H phases, which are suggested as a result of an ASSR, although the presence of the M-S-H phases could not be confirmed [23]. According to Mackenzie and Bowden [37], amesite is formed by the substitution of the Si^{4+} in the tetrahedral layers and the Mg^{2+} in the octahedral layers by the Al^{3+} . Therefore, the amesite detected in the mortars from the cistern tank could also have been formed as a result of the ASSR, since the kinetic formation of M-A-S-H phases has been described as similar to M-S-H phases, incorporating aluminium into the structure [63,70].

Besides, the phases formed as a result of the reaction between the aluminosilicate phases of the silico-aluminous aggregates and the putty alkalis contribute to decreasing the porosity and therefore favour the waterproofing of the cistern tank [45,71–73].

The study of both structural and plaster mortars from Amaiur Castle cistern show patterns/rules in the mortar manufacture according to the specific construction requirements, distinguishing two kinds of mortars with aggregates of different nature. Mortars from the cistern tank acquired hydraulicity by the addition of silico-aluminous rocks and ceramic fragments as aggregates.

6. Conclusions

The study of the mortars from the Amaiur Castle cistern has allowed assessing the knowledge of the mortar manufacturing process and the mortar application techniques to ensure the structure waterproofing necessary for the correct storage of water.

The cistern shows three types of lime mortars with different compositional characteristics related to the specific function within the structure: structural mortars from the barrel vault, structural mortars from the tank, and plaster.

The nature of the aggregates used in the manufacture of cistern mortars was different, according to specific construction requirements. Carbonated aggregates were used in the vault mortar and silicious and silico-aluminous aggregates in the tank mortars and plaster, suggesting the specific selection of raw materials.

The raw materials of the surrounding geological materials were used for the manufacture of the lime mortars of the cistern of the Amaïur Castle.

To confer hydraulicity to the mortars of the cistern tank and achieve the waterproofing of the structure, ceramic fragments and silico-aluminous rocks were used as aggregates in the manufacture.

Besides, the reaction zones on the edge of silico-aluminous rocks and ceramic aggregates resulted from an alkali silicate reaction (ASSR) that favoured the formation of amesite, the magnesium aluminosilicate hydrated (M-A-S-H) phase detected in the binder of the tank mortars.

A multilayering application technique was performed in the construction of the cistern tank. Two/three layers have been differentiated in the structural mortar from the tank, with a decrease in grain size and an improvement in sorting of aggregates from the inner part to the outer part. The plaster is formed by two layers: an inner layer and an outer pigmented layer.

The pigmented layer of plaster is composed by two types of additives. Hematite was identified as an inorganic additive giving rise to the reddish colour of the layer. Additionally, beeswax was identified as an organic additive used to confer impermeability to the pigmented layer.

The presence of hydrotalcite and the absence of dolomitic aggregates in the pigmented layer point to the use of impure limestones or partially dolomitized limestones as the raw material for the production of lime at Amaïur Castle.

Author Contributions: Conceptualization, G.P.-A., M.C.Z. and L.A.O.; Data Curation, G.P.-A. and M.C.Z.; Writing—Original Draft Preparation, G.P.-A.; Writing—Review and Editing, G.P.-A., M.C.Z.; Funding Acquisition, L.A.O. and J.A.M. All authors have read and agreed to the published version of the manuscript.

Funding: This research was funded by the IT1193-13 project of the Basque Government.

Acknowledgments: G.P.-A. acknowledges the PhD research grant of the Basque Government 2015-1-02-35. The authors would like to thank Peter Smith for reviewing the use of English in the manuscript.

Conflicts of Interest: The authors declare no conflict of interest.

References

1. Cadogan, G. Water management in Minoan Crete, Greece: The two cisterns of one Middle Bronze Age settlement. *Water Sci. Technol. Water Supply* **2007**, *7*, 103–112. [[CrossRef](#)]
2. Angelakis, A.N.; Spyridakis, D.S. Water supply and wastewater management aspects in Ancient Greece. *Water Sci. Technol. Water Supply* **2010**, *10*, 618–628. [[CrossRef](#)]
3. Angelakis, A.N.; Mays, L.W.; Koutsoyiannis, D.; Mamassis, N. *Evolution of Water Supply through the Millennia*; IWA Publishing: London, UK, 2012.
4. Carrion, A.; Formnes, A. Underground medieval water distribution network in a Spanish town. *Tunn. Undergr. Space Technol.* **2016**, *51*, 90–97. [[CrossRef](#)]
5. Mays, L.; Antoniou, G.P.; Angelakis, A.N. History of Water Cisterns: Legacies and Lessons. *Water* **2013**, *5*, 1916–1940. [[CrossRef](#)]
6. Van Hees, R.P.J.; Binda, L.; Papayianni, I.; Toumbakari, E. Characterisation and damage analysis of old mortars. *Mater. Struct.* **2004**, *37*, 644–648. [[CrossRef](#)]
7. Stefanidou, M.; Pachta, V.; Konopissi, S.; Karkadelidou, F.; Papayianni, I. Analysis and characterization of hydraulic mortars from ancient cisterns and baths in Greece. *Mater. Struct.* **2014**, *47*, 571–580. [[CrossRef](#)]
8. Rizzo, G.; Ercoli, L.; Megna, B.; Parlapiano, M. Characterization of mortars from ancient and traditional water supply systems in Sicily. *J. Therm. Anal. Calorim.* **2008**, *92*, 323–330. [[CrossRef](#)]

9. Henry, A.; Stewart, J. *Practical Building Conservation: Mortars, Renders & Plasters*; Practical Building Conservation Series; English Heritage: Surrey, UK, 2011.
10. Baronio, G.; Binda, L. Study of the pozzolanicity of some bricks and clays. *Constr. Build. Mater.* **1997**, *11*, 41–46. [[CrossRef](#)]
11. Baronio, G.; Binda, L.; Lombardini, N. The role of brick pebbles and dust in conglomerates based on hydrated lime and crushed bricks. *Constr. Build. Mater.* **1997**, *11*, 33–40. [[CrossRef](#)]
12. Stefanidou, M.; Papayianni, I. The role of aggregates on the structure and properties of lime mortars. *Cem. Concr. Compos.* **2005**, *27*, 914–919. [[CrossRef](#)]
13. Arizzi, A.; Cultrone, G. Aerial lime-based mortars blended with a pozzolanic additive and different admixtures: A mineralogical, textural and physical-mechanical study. *Constr. Build. Mater.* **2012**, *31*, 135–143. [[CrossRef](#)]
14. Miriello, D.; Bloise, A.; Crisci, G.M.; De Luca, R.; De Nigris, B.; Martellone, A.; Osannac, M.; Paced, R.; Peccia, A.; Ruggieri, N. New compositional data on ancient mortars and plasters from Pompeii (Campania-Southern Italy): Archaeometric results and considerations about their time evolution. *Mater. Charact.* **2018**, *146*, 189–203. [[CrossRef](#)]
15. Walker, R.; Pavía, S. Physical properties and reactivity of pozzolans, and their influence on the properties of lime–pozzolan pastes. *Mater. Struct.* **2011**, *44*, 1139–1150. [[CrossRef](#)]
16. Bonazza, A.; Ciantelli, C.; Sardella, A.; Pecchioni, E.; Favoni, O.; Natali, I.; Sabbioni, C. Characterization of hydraulic mortars from archaeological complexes in Petra. *Period. Mineral.* **2014**, *82*, 459.
17. Rampazzi, L.; Colombini, M.P.; Conti, C.; Corti, C.; Lluveras-Tenorio, A.; Sansonetti, A.; Zanaboni, M. Technology of medieval mortars: An investigation into the use of organic additives. *Archaeometry* **2016**, *58*, 115–130. [[CrossRef](#)]
18. Galán Pérez, E.; García de Domingo, A.; Cabra Gil, A.; Ganzález Lastra, J.; Matinez Torres, L.M.; Pesquera Pérez, A. Memoria Hoja 66-III (Maya de Baztán). In *Mapa Geológico de Navarra. E. 1:25000*; Diputación Foral de Navarra: Navarra, Spain, 2002.
19. Juch, D.; Krausse, H.F.; Müller, D.; Requadt, H.; Schafer, D.; Sole, J.; Villalobos, L. Memoria Hoja 66 (Maya del Baztan). In *Mapa Geológico de España, E. 1:50.000*, 1st ed.; Segunda Serie; MAGNA: Magna Drive Aurora, ON, Canada, 1974.
20. AGN. Royal and General Archive of Navarre. In *Rena Papers*; 15/3, 52, Box 33055: 1516; Government of Navarre: Pamplona, Spain, 1995.
21. Sagredo, I. *El castillo de Amaiur a Través de la Historia de Navarra*; Editorial Pamiela Argitaletxea: Pamplona, Spain, 2009.
22. Sagredo, I. Navarra. In *Castillos que Defendieron el Reino (Tomo I) de Laguardia a Foix, y del Moncayo al Goierri*; Editorial Pamiela Argitaletxea: Pamplona, Spain, 2006.
23. Ponce-Antón, G.; Zuluaga, M.C.; Ortega, L.A.; Mauleon, J.A. Multi-analytical approach for chemical-mineralogical characterization of reaction rims in the lime mortars from Amaiur Castle (Navarre, Spain). *Microchem. J.* **2020**, *152*, 104303. [[CrossRef](#)]
24. Boynton, R.S. *Chemistry and Technology of Lime and Limestone*; John Wiley & Sons, Inc.: New York, NY, USA, 1980.
25. Vicat, L.J. *Mortars and Cements*; Donhead Publishing: Shaftesbury, UK, 1997.
26. Folk, R.L. A comparison chart for visual percentage estimation. *J. Sediment. Res.* **1951**, *21*, 32–33.
27. Ortega, L.A.; Zuluaga, M.C.; Alonso-Olazabal, A.; Murelaga, X.; Insausti, M.; Ibañez-Etxeberria, A. Historic lime-mortar ¹⁴C dating of Santa María la Real (Zarautz, northern Spain): Extraction of suitable grain size for reliable ¹⁴C dating. *Radiocarbon* **2012**, *54*, 23–36. [[CrossRef](#)]
28. Ponce-Antón, G.; Ortega, L.A.; Zuluaga, M.C.; Alonso-Olazabal, A.; Solaun, J.L. Hydrotalcite and Hydrocalumite in Mortar Binders from the Medieval Castle of Portilla (Álava, North Spain): Accurate Mineralogical Control to Achieve More Reliable Chronological Ages. *Minerals* **2018**, *8*, 326. [[CrossRef](#)]
29. Mills, S.J.; Christy, A.G.; Génin, J.-M.R.; Kameda, T.; Colombo, F. Nomenclature of the hydrotalcite supergroup: Natural layered double hydroxides. *Mineral. Mag.* **2012**, *76*, 1289–1336. [[CrossRef](#)]
30. Bakolas, A.; Biscontin, G.; Moropoulou, A.; Zendri, E. Characterization of structural byzantine mortars by thermogravimetric analysis. *Thermochim. Acta* **1998**, *321*, 151–160. [[CrossRef](#)]
31. Paama, L.; Pitkänen, I.; Rönkkömäki, H.; Perämäki, P. Thermal and infrared spectroscopic characterization of historical mortars. *Thermochim. Acta* **1998**, *320*, 127–133. [[CrossRef](#)]

32. Moropoulou, A.; Bakolas, A.; Anagnostopoulou, S. Composite materials in ancient structures. *Cem. Concr. Compos.* **2005**, *27*, 295–300. [[CrossRef](#)]
33. Yang, W.; Kim, Y.; Liu, P.K.T.; Sahimi, M.; Tsotsis, T.T. A study by in situ techniques of the thermal evolution of the structure of a Mg-Al-CO₃ layered double hydroxide. *Chem. Eng. Sci.* **2002**, *57*, 2945–2953. [[CrossRef](#)]
34. León, M.; Díaz, E.; Bennici, S.; Vega, A.; Ordóñez, S.; Auroux, A. Adsorption of CO₂ on Hydrotalcite-Derived Mixed Oxides: Sorption Mechanisms and Consequences for Adsorption Irreversibility. *Ind. Eng. Chem. Res.* **2010**, *49*, 3663–3671. [[CrossRef](#)]
35. Brindley, G.W.; Oughton, B.M.; Youell, R.F. The crystal structure of amesite and its thermal decomposition. *Acta Crystallogr.* **1951**, *4*, 552–557. [[CrossRef](#)]
36. Grim, R.E. *Applied Clay Mineralogy*; Mc Graw-Hill: New York, NY, USA, 1962.
37. MacKenzie, K.J.D.; Bowden, M.E. Thermal and Mössbauer studies of iron-containing hydrous silicates. IV. Amesite. *Thermochim. Acta* **1983**, *64*, 83–106. [[CrossRef](#)]
38. Drits, V.A.; McCarty, D.K. The nature of structure-bonded H₂O in illite and leucophyllite from dehydration and dehydroxylation experiments. *Clays Clay Miner.* **2007**, *55*, 45–58. [[CrossRef](#)]
39. Duran, A.; Jimenez De Haro, M.C.; Perez-Rodriguez, J.L.; Franquelo, M.L.; Herrera, L.K.; Justo, A. Determination of pigments and binders in Pompeian wall paintings using synchrotron radiation–high-resolution X-ray powder diffraction and conventional spectroscopy–chromatography. *Archaeometry* **2010**, *52*, 286–307. [[CrossRef](#)]
40. Franquelo, M.L.; Robador, M.D.; Ranirez-Valle, V.; Duran, A.; Jimenez de Haro, M.C.; Pérez-Rodríguez, J.L. Roman ceramics of hydraulic mortars used to build the Mithraeum house of Mérida (Spain). *J. Therm. Anal. Calorim.* **2008**, *92*, 331–335. [[CrossRef](#)]
41. Farmer, V.C. *The Infrared Spectra of Minerals*; Mineralogical Society of Great Britain and Ireland: London, UK, 1974; Volume 4.
42. Smith, B. *Infrared Spectra Interpretation: A Systematic Approach*; CRC Press: Florida, FL, USA, 1999.
43. Vahur, S.; Teearu, A.; Peets, P.; Joosu, L.; Leito, I. ATR-FT-IR spectral collection of conservation materials in the extended region of 4000–80 cm⁻¹. *Anal. Bioanal. Chem.* **2016**, *408*, 3373–3379. [[CrossRef](#)] [[PubMed](#)]
44. Odler, I. Hydration, Setting and Hardening of Portland Cement. In *Lea's Chemistry of Cement and Concrete*; Hewlett, P.C., Ed.; Elsevier: London, UK, 2003; pp. 241–289.
45. Papayianni, I.; Stefanidou, M. Strength–porosity relationships in lime–pozzolan mortars. *Constr. Build. Mater.* **2006**, *20*, 700–705. [[CrossRef](#)]
46. Sabir, B.B.; Wild, S.; Bai, J. Metakaolin and calcined clays as pozzolans for concrete: A review. *Cem. Concr. Compos.* **2001**, *23*, 441–454. [[CrossRef](#)]
47. Cunha, A.L.C.; Gonçalves, J.P.; Dweck, J. Evaluating the pozzolanic activity of spent catalyst partially substituting type II Portland cement. In *Key Engineering Materials*; Trans Tech Publications Ltd.: Stafa-Zurich, Switzerland, 2014; Volume 634, pp. 131–138.
48. Arizzi, A.; Cultrone, G. Comparing the pozzolanic activity of aerial lime mortars made with metakaolin and fluid catalytic cracking catalytic residue: A petrographic and physical-mechanical study. *Constr. Build. Mater.* **2018**, *184*, 382–390. [[CrossRef](#)]
49. Romagnoli, M.; Rivasi, M.R. Optimal size distribution to obtain the densest packing: A different approach. *J. Eur. Ceram. Soc.* **2007**, *27*, 1883–1887. [[CrossRef](#)]
50. Fung, W.W.S.; Kwan, A.K.H.; Wong, H.H.C. Wet packing of crushed rock fine aggregate. *Mater. Struct.* **2008**, *42*, 631–643. [[CrossRef](#)]
51. Kwan, A.K.H.; Fung, W.W.S. Packing density measurement and modelling of fine aggregate and mortar. *Cem. Concr. Compos.* **2009**, *31*, 349–357. [[CrossRef](#)]
52. Arizzi, A.; Cultrone, G. The influence of aggregate texture, morphology and grading on the carbonation of non-hydraulic (aerial) lime-based mortars. *Q. J. Eng. Geol. Hydrogeol.* **2013**, *46*, 507–520. [[CrossRef](#)]
53. Colombini, M.P.; Modugno, F. *Organic Mass Spectrometry in Art and Archaeology*; John Wiley & Sons, Ltd.: Hoboken, NJ, USA, 2009.
54. Luxán, M.P.; Dorrego, F.; Laborde, A. Ancient gypsum mortars from St. Engracia (Zaragoza, Spain): Characterization. Identification of additives and treatments. *Cem. Concr. Res.* **1995**, *25*, 1755–1765. [[CrossRef](#)]
55. Beruto, D.T.; Vecchiattini, R.; Giordani, M. Solid products and rate-limiting step in the thermal half decomposition of natural dolomite in a CO₂ (g) atmosphere. *Thermochim. Acta* **2003**, *405*, 183–194. [[CrossRef](#)]

56. Gan, G.-L.; Spry, P.G.; Cody, A.M. Rim Formation on Iowa Highway Concrete Dolomite Aggregate: The Effects of Dedolomitization Reactions. *Environ. Eng. Geosci.* **1996**, *2*, 59–72. [[CrossRef](#)]
57. Sipos, P. The structure of Al(III) in strongly alkaline aluminate solutions—A review. *J. Mol. Liq.* **2009**, *146*, 1–14. [[CrossRef](#)]
58. Zajac, M.; Bremseth, S.K.; Whitehead, M.; Ben Haha, M. Effect of $\text{CaMg}(\text{CO}_3)_2$ on hydrate assemblages and mechanical properties of hydrated cement pastes at 40 °C and 60 °C. *Cem. Concr. Res.* **2014**, *65*, 21–29. [[CrossRef](#)]
59. Schork, J. Dolomitic Lime in the US. *J. Archit. Conserv.* **2012**, *18*, 7–25. [[CrossRef](#)]
60. Hobbs, D.W. *Alkali-Silica Reaction in Concrete*; Thomas Telford: London, UK, 1988.
61. Katayama, T. How to identify carbonate rock reactions in concrete. *Mater. Charact.* **2004**, *53*, 85–104. [[CrossRef](#)]
62. da Fonseca, J.M.M.; de Souza, V.K.B.; da Silva, D.G.C.; da Silva, D.L.; Monteiro, E.C.B. Alkali-Aggregate Reaction: Definition, Influence and Control. *Eng. Appl. Sci.* **2018**, *3*, 12.
63. Braz, I.G.; Shinzato, M.C.; Montanheiro, T.J.; de Almeida, T.M.; de Souza Carvalho, F.M. Effect of the addition of aluminum recycling waste on the pozzolanic activity of sugarcane bagasse ash and zeolite. *Waste Biomass Valorization* **2019**, *10*, 3493–3513. [[CrossRef](#)]
64. Brew, D.R.M.; Glasser, F.P. Synthesis and characterisation of magnesium silicate hydrate gels. *Cem. Concr. Res.* **2005**, *35*, 85–98. [[CrossRef](#)]
65. Zhang, T.; Vandeperre, L.J.; Cheeseman, C.R. Formation of magnesium silicate hydrate (MSH) cement pastes using sodium hexametaphosphate. *Cem. Concr. Res.* **2014**, *65*, 8–14. [[CrossRef](#)]
66. Bernard, E.; Lothenbach, B.; Cau-Dit-Coumes, C.; Chlique, C.; Dauzères, A.; Pochard, I. Magnesium and calcium silicate hydrates, Part I: Investigation of the possible magnesium incorporation in calcium silicate hydrate (C-S-H) and of the calcium in magnesium silicate hydrate (M-S-H). *Appl. Geochem.* **2018**, *89*, 229–242. [[CrossRef](#)]
67. Roosz, C.; Grangeon, S.; Blanc, P.; Montouillout, V.; Lothenbach, B.; Henocq, P.; Giffaut, E.; Vieillard, P.; Gaboreau, S. Crystal structure of magnesium silicate hydrates (M-S-H): The relation with 2:1 Mg-Si phyllosilicates. *Cem. Concr. Res.* **2015**, *73*, 228–237. [[CrossRef](#)]
68. Walling, S.A.; Kinoshita, H.; Bernal, S.A.; Collier, N.C.; Provis, J.L. Structure and properties of binder gels formed in the system $\text{Mg}(\text{OH})_2\text{-SiO}_2\text{-H}_2\text{O}$ for immobilisation of Magnox sludge. *Dalton Trans.* **2015**, *44*, 8126–8137. [[CrossRef](#)] [[PubMed](#)]
69. Nied, D.; Enemark-Rasmussen, K.; L'Hopital, E.; Skibsted, J.; Lothenbach, B. Properties of magnesium silicate hydrates (M-S-H). *Cem. Concr. Res.* **2016**, *79*, 323–332. [[CrossRef](#)]
70. Bernard, E. *Magnesium Silicate Hydrate (MSH) Characterization: Temperature, Calcium, Aluminium and Alkali*; University of Burgundy Franche-Comté: Besançon, France, 2017.
71. Schaefer, J.; Hilsdorf, H.K. Ancient and new lime mortars—The correlation between their composition structure and properties. In *Conservation of Stone and Other Materials, Prevention and Treatments*; Thiel, M.-J., Ed.; (RILEM proceedings. 21,2.); E & FN Spon: London, UK, 1993; Volume 2, pp. 605–612.
72. Papayianni, I.; Stefanidou, M. The Evolution of Porosity in Lime-Based Mortars. In *Proceedings of the 8th Euroseminar on Microscopy Applied to Building Materials*, Athens, Greece, 4–7 September 2001; pp. 451–458.
73. Thomson, M.; Lindqvist, J.E.; Elsen, J.; Groot, C.J.W.P. 2.5. *Porosity of Mortars*; RILEM Publications SARL: Cachan, France, 2007; pp. 77–106.



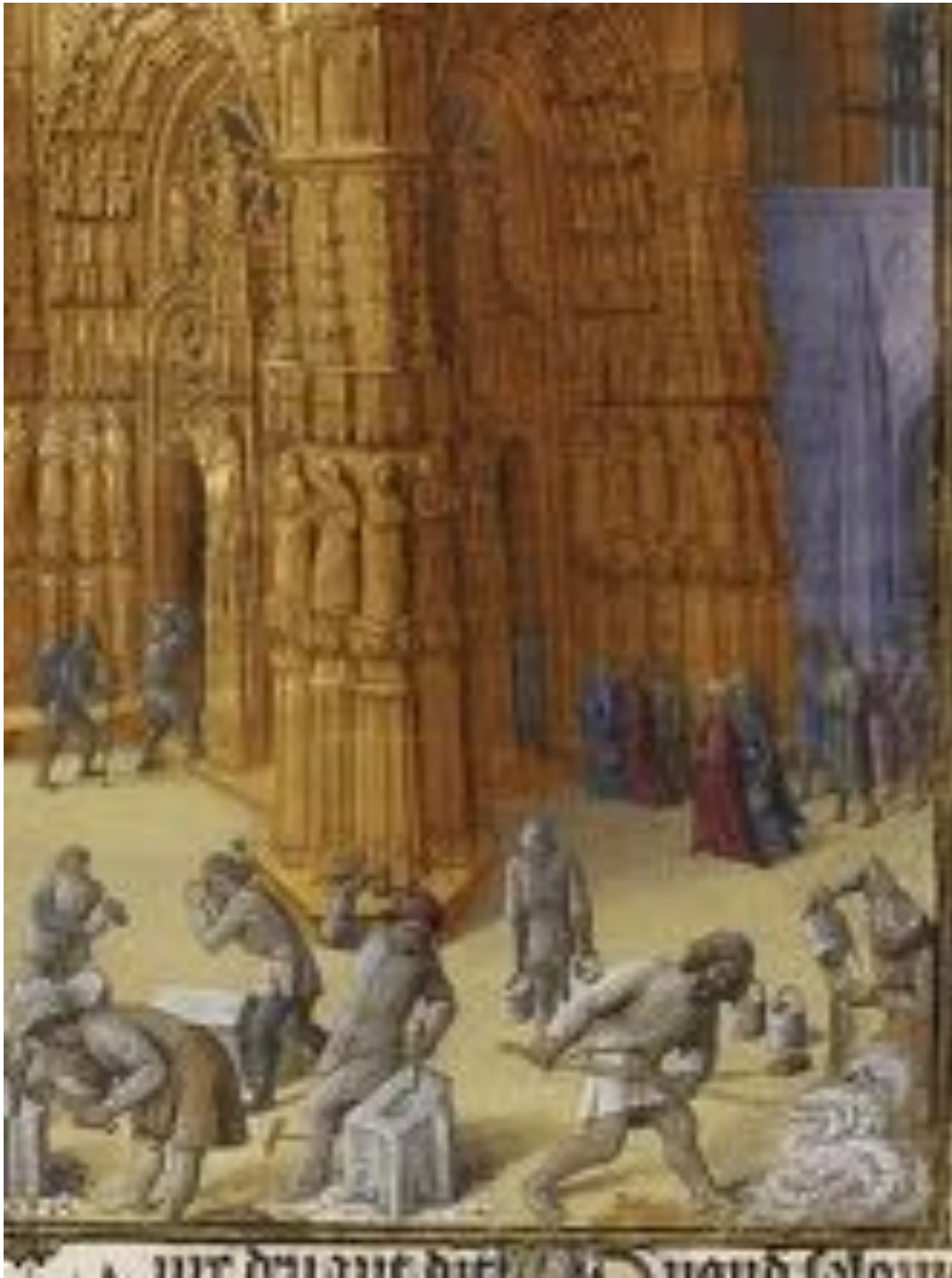
© 2020 by the authors. Licensee MDPI, Basel, Switzerland. This article is an open access article distributed under the terms and conditions of the Creative Commons Attribution (CC BY) license (<http://creativecommons.org/licenses/by/4.0/>).

Allí donde muere
la investigación científica
nace
la imaginación
poética.

Luis Eduardo Aute
Ciencia poética que no poesía científica, EL SEXtO ANIMAL

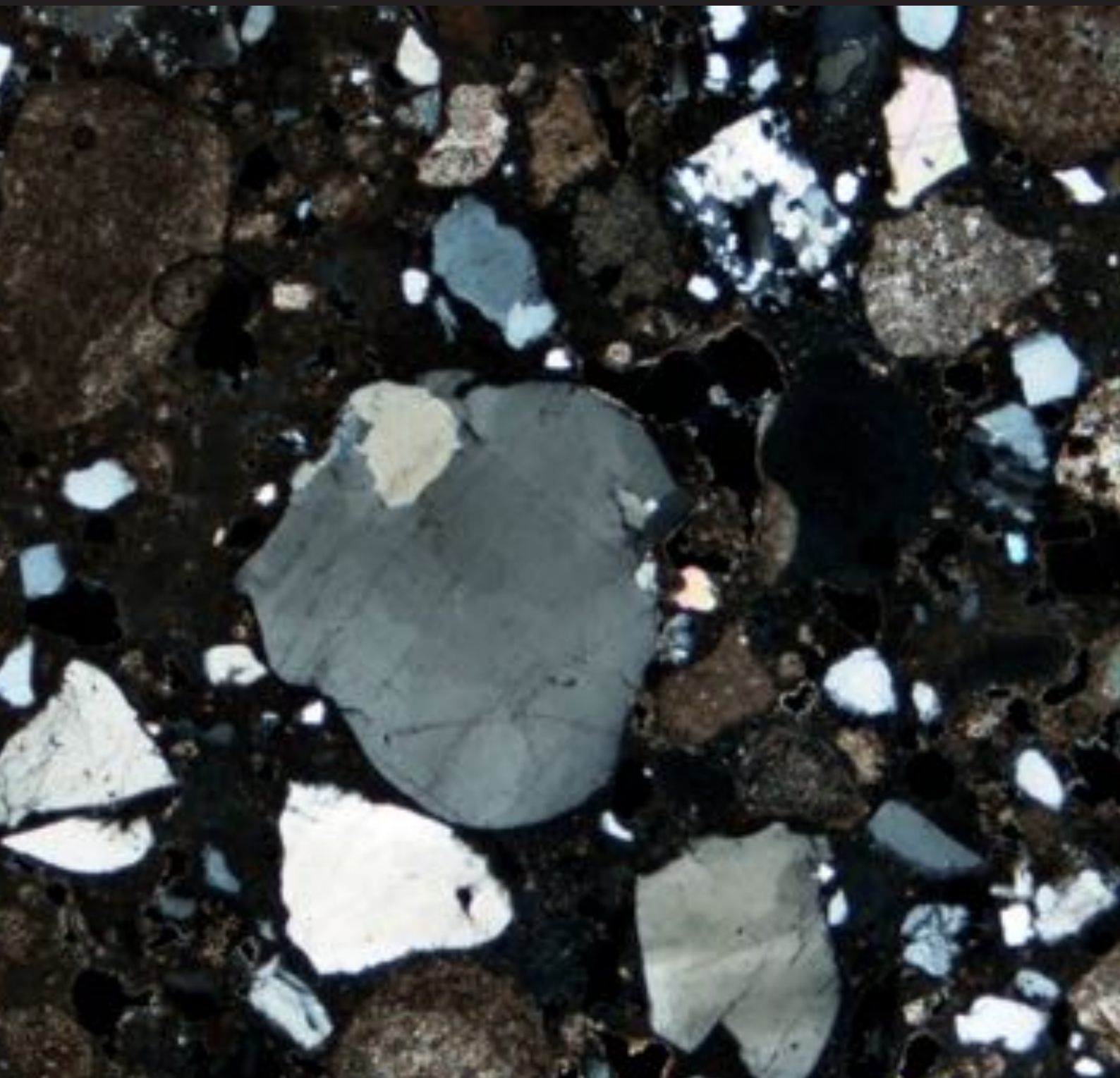


Top left, a mason manufacturing a mortar. A detail from *Building of the Tower of Babel*, In: *Bedford Hours*. British Library, London. Add Ms 18850, fol.17 v. Bedford Master, ca. 1410-1430.



Bottom right, masons manufacturing a mortar. A detail from *Construction du Temple de Jérusalem par ordre de Salomon.*, In: *Antiquités judaïques de Flavius Josèphe.* Bibliothèque Nationale de France, Paris. Ms 247, fol.163 v. Jean Fouquet, 1470-1475.

This PhD thesis has been accomplished with the research grant from the Basque Country Government PRE-2015-1-0235 in the Department of Mineralogy and Petrology of the University of the Basque Country (UPV/EHU) under the supervision of Dr Maria Cruz Zuluaga and Dr Luis Angel Ortega.



The conservation and restoration of monuments must have recourse to all the sciences and techniques which can contribute to the study and safeguarding of the architectural heritage.

Article 2. Venice Charter, 1964